

# POLITECNICO DI MILANO

Corso di Laurea Magistrale in Ingegneria Aeronautica

Scuola di Ingegneria Industriale e dell'Informazione

Dipartimento di Scienze e Tecnologie Aeroespaziali



## **Exact solutions to non-classical, quasi-1D steady nozzle flows of Bethe-Zel'dovich-Thompson fluids**

Relatore: Prof. Alberto Guardone

Tesi di laurea di:  
Davide Vimercati  
Matr. 800911

Anno Accademico 2013 - 2014



## Abstract

The properties of steady internal flows of Bethe-Zel'dovich-Thompson (BZT) fluids—substances exhibiting a finite region of negative fundamental derivative of gasdynamics—are analyzed. Neglecting the effects of viscosity and thermal diffusion, exact solutions to flows of a mono-component and single-phase fluids in a converging-diverging nozzle are derived here for the first time, within a quasi-one-dimensional approximation. The governing differential equations are analytically integrated, holding the uniformity of the mass flow rate, the entropy and the total enthalpy. Given the values of these three quantities, the problem is recast in terms of a single algebraic equation with density as unknown. Shock waves play a significant role in the complete description of nozzle flows. A general solution consists of isentropic portions matched with shock discontinuities, which have to satisfy the Rankine-Hugoniot jump relations together with suitable admissibility criteria. The proposed solution method consist in solving at most systems of non linear algebraic equations, with the desired accuracy. Hence, these solutions are to be considered exact, though no closed-form analytical expression is provided. The van der Waals polytropic model, i.e. with constant specific heat at constant volume, is used here as the most simple model allowing for a BZT fluid behavior. The nozzle is considered as a discharging device between a reservoir and a stationary atmosphere with fixed pressure. For given reservoir conditions, a specific sequence of exact solutions is observed as the exhaust condition is altered. The resulting exact solutions layout identifies the so-called functioning regime. The BZT fluid class is found to exhibit eight distinct functioning regimes, with significant differences compared to the well-known solutions layout for ideal gases. Non-ideal effects include the non-monotonicity of Mach number in isentropic flows, the presence of rarefaction shock waves and shock-splitting configurations. The dependence of the functioning regimes on the reservoir conditions is analyzed, to produced the so-called thermodynamic map of functioning regimes. The effect of varying the molecular complexity is also discussed.

**Keywords:** Nozzle flows, Non-ideal compressible fluid dynamics (NICFD), non-classical gasdynamics, rarefaction shock waves, Bethe-Zel'dovich-Thompson (BZT) fluids, van der Waals model.



## Sommario

Nel presente lavoro vengono analizzate le proprietà di correnti interne di vapori di fluidi Bethe-Zel'dovich-Thompson (BZT), ossia quelle sostanze in grado di esibire una regione termodinamica con derivata fondamentale della gasdinamica negativa. Considerando trascurabili gli effetti della viscosità e della conducibilità termica, lo scopo è produrre delle soluzioni esatte per un flusso monocomponente e monofase in un tipico ugello convergente-divergente, nell'ambito di un'approssimazione quasi mono-dimensionale. Le equazioni differenziali che governano la corrente sotto tali ipotesi possono essere integrate analiticamente ottenendo l'uniformità di tre variabili lungo l'asse dell'ugello: il flusso di massa, l'entropia e l'entalpia totale. Un'opportuna rielaborazione delle equazioni consente di ottenere un'unica equazione algebrica implicita per l'incognita densità, una volta fissati i valori delle tre quantità costanti nell'ugello. Le onde d'urto giocano un ruolo importante per una completa descrizione della corrente. A queste si richiede di soddisfare le relazioni di salto di Rankine-Hugoniot, insieme a determinate condizioni di ammissibilità. Una soluzione generale del problema in esame è costituita da porzioni isoentropiche, nelle quali le equazioni in forma differenziale sono valide, opportunamente interfacciate da onde d'urto normali. Considerando l'ugello come un dispositivo connesso a monte ad un serbatoio e a valle ad una regione con pressione fissata, il metodo qui proposto consente di ottenere la soluzione del problema risolvendo al più sistemi non lineari di equazioni algebriche, le cui radici possono essere determinate numericamente con l'accuratezza desiderata. Di conseguenza le soluzioni vengono considerate esatte, sebbene non ne venga fornita un'espressione analitica. Il modello termodinamico qui impiegato, il gas di van der Waals politropico con elevata complessità molecolare, si rivela molto adatto per uno studio qualitativo del problema. Per condizioni di serbatoio fissate, al variare della condizione a valle, ossia la pressione allo scarico, si osserva una specifica sequenza di soluzioni esatte. La forma e la sequenza stessa delle soluzioni identificano un determinato regime di funzionamento. Otto diversi regimi di funzionamento vengono introdotti per i flussi di fluidi BZT. Le differenze principali con i flussi di gas ideali includono la non-monotonicità del numero di Mach in correnti isoentropiche, la formazione di onde d'urto di rarefazione e di configurazioni shock-splitting. Si studia la dipendenza del regime di funzionamento dalle condizioni di serbatoio, per ottenere la cosiddetta mappa termodinamica dei regimi. Si discute infine l'effetto su questa stessa mappa di una riduzione della complessità molecolare.

**Keywords:** Flussi in ugelli, Fluidodinamica comprimibile non-ideale (NICFD), gasdinamica nonclassica, onde d'urto di rarefazione, fluidi di Bethe-Zel'dovich-Thompson (BZT), modello di van der Waals.



## **Acknowledgements**

I would like to express my sincere gratitude to my supervisor Prof. Alberto Guardone for the continuous support, for his valuable guidance, for his patience and enthusiasm.

A special thank to my parents. Thanks, from the bottom of my heart, for your ever-present support. To my brother: thank you for bearing with me every single day.

Last but not the least, I would like to thank my friends, inside and outside the university, my companions in everyday life and in this five-year adventure.



# Contents

<b>1</b>	<b>Introduction</b>	<b>19</b>
1.1	Fundamentals of non-classical gasdynamics . . . . .	19
1.2	Internal flows of non-ideal compressible fluids . . . . .	20
1.3	Goal and outline of the thesis . . . . .	22
<b>2</b>	<b>Nozzle flows of non-ideal fluids</b>	<b>25</b>
2.1	Governing equations for steady, quasi-1D flows . . . . .	25
2.2	The thermodynamic model employed . . . . .	26
2.2.1	LMC, HMC and BZT fluids . . . . .	28
2.3	Steady isentropic flow . . . . .	30
2.3.1	The standard differential approach . . . . .	30
2.3.2	Mach number variations with density . . . . .	32
2.3.3	The flux function . . . . .	34
2.3.4	The phase plane . . . . .	36
2.3.5	Isentropic patterns . . . . .	39
2.4	Steady flow with shocks . . . . .	44
2.4.1	Jump relations and admissibility conditions . . . . .	44
2.4.2	Flux function and sonic shocks . . . . .	46
2.4.3	Isentropic pattern transitions . . . . .	47
<b>3</b>	<b>Exact solutions to quasi-1D steady nozzle flows</b>	<b>51</b>
3.1	Problem description . . . . .	51
3.2	Limiting and intermediate solutions . . . . .	52
3.3	The computation procedure . . . . .	53
3.3.1	Computation of limiting solutions . . . . .	53
3.3.2	Computation of intermediate solutions . . . . .	56
3.4	Exact solutions for HMC fluids . . . . .	59
3.4.1	Remark on functioning regimes . . . . .	60
3.5	Exact solutions for BZT fluids . . . . .	62
3.5.1	Preliminary remarks . . . . .	62
3.5.2	Functioning regimes for BZT fluids . . . . .	64
3.6	Summary of functioning regimes . . . . .	84
<b>4</b>	<b>Comparison with a quasi 1-D shock capturing method</b>	<b>87</b>
4.1	Governing equations for quasi 1-D unsteady flow . . . . .	87
4.2	Numerical methods for balance laws . . . . .	88

4.3 Numerical results . . . . .	93
4.3.1 Comparison of the different methods . . . . .	93
4.3.2 Comparison with exact solutions . . . . .	94
<b>5 Thermodynamic map of functioning regimes</b>	<b>105</b>
5.1 Transitional regimes . . . . .	105
5.2 The maximum mass flow rate . . . . .	120
5.3 Map's variation with molecular complexity . . . . .	121
<b>6 Conclusions</b>	<b>125</b>
<b>A Nozzle geometry</b>	<b>129</b>
<b>B Shock adiabat concavity at a sonic point</b>	<b>131</b>
<b>C Solution of nonlinear systems of equations</b>	<b>135</b>
<b>Bibliography</b>	<b>137</b>
<b>Estratto in lingua italiana</b>	<b>141</b>

# List of Figures

2.1	Evolution of a triangular pressure disturbance: (a) $\Gamma > 0$ , formation of a compression shock; (b) $\Gamma < 0$ , formation of a rarefaction shock. Taken from [31] . . . . .	29
2.2	$\Gamma = 1$ loci for different values of molecular complexity $N$ . For $N = N^{HMC}$ the $\Gamma = 1$ locus reduces to a point located on the saturation curve. . . . .	30
2.3	$\Gamma = 0$ loci for different values of molecular complexity $N$ . For $N = N^{BZT}$ the $\Gamma = 0$ locus reduces to a point located on the saturation curve. . . . .	31
2.4	Mach number variations with density for a polytropic van der Waals gas with $\delta = 1/10$ , which represents a HMC fluid. The different curves are relative to the same entropy. The stagnation states correspond to different densities along the same isentrope. The reference isentrope enters the $\Gamma < 1$ region. . . . .	33
2.5	Mach number variations with density for a polytropic van der Waals gas with $\delta = 1/50$ , which represents a BZT fluid. The different curves are relative to the same entropy. The stagnation states correspond to different densities along the same isentrope. The reference isentrope enters the $\Gamma < 0$ region. . . . .	34
2.6	Representative flux functions for a polytropic van der Waals gas with $\delta = 1/50$ . The different curves correspond to the stagnation states used to compute the curves of Fig. 2.5. The dots indicate sonic points, which are stationary points of the flux function. . . . .	36
2.7	Phase plane - The stagnation conditions exhibit one sonic point only, in an isentropic expansion. . . . .	37
2.8	Phase plane - The stagnation conditions exhibit three sonic points, in an isentropic expansion. The largest of the sonic densities corresponds to the global maximum of the related flux function. . . . .	38
2.9	Phase plane - The stagnation conditions exhibit three sonic points, in an isentropic expansion. The lowest of the sonic densities corresponds to the global maximum of the related flux function. . . . .	39
2.10	Limiting curves computed for a polytropic van der Waals gas with $\delta = 1/50$ . The reference isentrope enters $\Gamma < 0$ region. . . . .	41
2.11	Transitional phase planes: (a) $\mathcal{S}_{\mathcal{M}-}/\mathcal{S}_{\mathcal{N}-}$ , (b) $\mathcal{S}_{\mathcal{N}-}/\mathcal{S}_{\mathcal{N}+}$ , (c) $\mathcal{S}_{\mathcal{N}+}/\mathcal{S}_{\mathcal{M}+}$ , computed for a polytropic van der Waals gas with $\delta = 1/50$ . . . . .	42

---

2.12	$P$ - $v$ diagram of stagnation states leading to different isentropic patterns. The curves are computed from the polytropic van der Waals model with $\delta = 1/50$ . The three isentropes displayed are those tangent to the VLE line, the $\Gamma = 0$ locus and the $\Gamma = 1$ locus.	43
2.13	$T$ - $s$ diagram of stagnation states leading to different isentropic patterns. The curves are computed from the polytropic van der Waals model with $\delta = 1/50$ .	44
2.14	Mach number variations with density for a polytropic van der Waals gas with $\delta = 1/50$ . The stagnation states correspond to different densities along the same isenthalpic. The different isentropes represent possible expansion or compression with the same total enthalpy.	48
2.15	Mach number variations with density for a polytropic van der Waals gas with $\delta = 1/50$ . Limiting curves for different isentropic patterns. The curves are relative to the same total enthalpy.	49
2.16	Saturation curve $M^{\text{sat}}(\rho, h^t)$ . Effect of varying the reference total enthalpy.	50
3.1	Density, pressure and Mach number limiting solutions for $\mathcal{R}_{\mathcal{I}}$ functioning regime. Solutions computed from the polytropic van der Waals model with $\delta = 1/3$ , corresponding to a LMC fluid. Reservoir conditions: $v_{\text{res}} = 10v_c$ , $P_{\text{res}} = 10P_c$ .	55
3.2	Density, pressure and Mach number intermediate solutions (continuous line) and limiting solutions (dotted line) for $\mathcal{R}_{\mathcal{I}}$ functioning regime. Solutions computed from the polytropic van der Waals model with $\delta = 1/3$ , corresponding to a LMC fluid. Reservoir conditions: $v_{\text{res}} = 10v_c$ , $P_{\text{res}} = 10P_c$ .	57
3.3	Phase plane for the two isentropic portions of intermediate solution $\mathcal{R}_{\mathcal{I}}^{[1-2]}$	59
3.4	Mach number limiting solutions for $\mathcal{R}_{\mathcal{M}^+}$ functioning regime. Solutions computed from the polytropic van der Waals model with $\delta = 1/15$ , corresponding to a HMC fluid. Reservoir conditions: $v_{\text{res}} = 0.50v_c$ , $P_{\text{res}} = 6.61P_c$ .	60
3.5	Mach number intermediate solutions (continuous line) and limiting solutions (dotted line) for $\mathcal{R}_{\mathcal{M}^+}$ functioning regime. Solutions computed from the polytropic van der Waals model with $\delta = 1/15$ , corresponding to a HMC fluid. Reservoir conditions: $v_{\text{res}} = 0.5048v_c$ , $P_{\text{res}} = 6.6134P_c$ .	61
3.6	Example of limiting solution containing multiple shocks (bold line), together with portions of phase planes relative to the different isentropic branches.	62
3.7	Example of limiting solution containing multiple shocks (bold line), together with portions of phase planes relative to the different isentropic branches. The second shock also determines an isentropic pattern transition.	63

- 
- 3.8 Mach number limiting solutions for  $\mathcal{R}_{\mathcal{M}-}$  functioning regime. Solutions computed from the polytropic van der Waals model with  $\delta = 1/50$ , corresponding to a BZT fluid. Reservoir conditions:  $v_{\text{res}} = 0.8087v_c, P_{\text{res}} = 1.2148P_c$ . . . . . 64
- 3.9 Mach number intermediate solutions (continuous line) and limiting solutions (dotted line) for  $\mathcal{R}_{\mathcal{M}-}$  functioning regime. Solutions computed from the polytropic van der Waals model with  $\delta = 1/50$ , corresponding to a BZT fluid. Reservoir conditions:  $v_{\text{res}} = 0.8087v_c, P_{\text{res}} = 1.2148P_c$ . . . . . 65
- 3.10 Density, pressure and Mach number limiting solutions for  $\mathcal{R}_{\mathcal{N}^{2+}}$  functioning regime. Solutions computed from the polytropic van der Waals model with  $\delta = 1/50$ , corresponding to a BZT fluid. Reservoir conditions:  $v_{\text{res}} = 0.7818v_c, P_{\text{res}} = 1.1168P_c$ . . . . . 67
- 3.11 Shock adiabat through a point exhibiting null fundamental derivative, computed from the polytropic van der Waals model with  $\delta = 1/50$ . The Rayleigh line corresponds to a pre-sonic shock. . . . . 69
- 3.12 Density, pressure and Mach number intermediate solutions (continuous line) and limiting solutions (dotted line) for  $\mathcal{R}_{\mathcal{N}^{2+}}$  functioning regime. Solutions computed from the polytropic van der Waals model with  $\delta = 1/50$ , corresponding to a BZT fluid. Reservoir conditions:  $v_{\text{res}} = 0.7818v_c, P_{\text{res}} = 1.1168P_c$ . . . . . 72
- 3.13 Density, pressure and Mach number limiting solutions for  $\mathcal{R}_{\mathcal{N}^{2-}}$  functioning regime. Solutions computed from the polytropic van der Waals model with  $\delta = 1/50$ , corresponding to a BZT fluid. Reservoir conditions:  $v_{\text{res}} = 0.7880v_c, P_{\text{res}} = 1.2931P_c$ . . . . . 74
- 3.14 Compression shock with intermediate sonic step, in which the Rayleigh line is tangent to the shock adiabat, computed from a polytropic van der Waals model with  $\delta = 1/50$ . A slight decrease of the mass flux causes a shock-splitting configuration. . . . . 76
- 3.15 Density, pressure and Mach number limiting solutions for  $\mathcal{R}_{\mathcal{N}^{1+}}$  functioning regime. Solutions computed from the polytropic van der Waals model with  $\delta = 1/50$ , corresponding to a BZT fluid. Reservoir conditions:  $v_{\text{res}} = 0.7600v_c, P_{\text{res}} = 1.1453P_c$ . . . . . 77
- 3.16 Density, pressure and Mach number intermediate solutions (continuous line) and limiting solutions (dotted line) for  $\mathcal{R}_{\mathcal{N}^{2+}}$  functioning regime. Solutions computed from the polytropic van der Waals model with  $\delta = 1/50$ , corresponding to a BZT fluid. Reservoir conditions:  $v_{\text{res}} = 0.7600v_c, P_{\text{res}} = 1.1453P_c$ . . . . . 79
- 3.17 Density, pressure and Mach number limiting solutions for  $\mathcal{R}_{\mathcal{N}^{1-}}$  functioning regime. Solutions computed from the polytropic van der Waals model with  $\delta = 1/50$ , corresponding to a BZT fluid. Reservoir conditions:  $v_{\text{res}} = 0.7760v_c, P_{\text{res}} = 1.2576P_c$ . . . . . 82
- 3.18 Density, pressure and Mach number limiting solutions for  $\mathcal{R}_{\mathcal{N}^3}$  functioning regime. Solutions computed from the polytropic van der Waals model with  $\delta = 1/50$ , corresponding to a BZT fluid. Reservoir conditions:  $v_{\text{res}} = 0.6775v_c, P_{\text{res}} = 1.3566P_c$ . . . . . 85

- 
- 3.19 Density, pressure and Mach number intermediate solutions (continuous line) and limiting solutions (dotted line) for  $\mathcal{R}_{\mathcal{N}^3}$  functioning regime. Solutions computed from the polytropic van der Waals model with  $\delta = 1/50$ , corresponding to a BZT fluid. Reservoir conditions:  $v_{\text{res}} = 0.6775v_c$ ,  $P_{\text{res}} = 1.3566P_c$ . . . . . 86
- 4.1 Formulation (4.3): comparison between different numerical methods, on case  $\mathcal{R}_{\mathcal{N}^{2+}}^{[4-5]}$ , for 200, 300, 600 cells on a uniform grid. . . . . 91
- 4.2 Formulation (4.4): comparison between different numerical methods, on case  $\mathcal{R}_{\mathcal{N}^{2+}}^{[4-5]}$ , for 200, 300, 600 cells on a uniform grid. . . . . 92
- 4.3 Entropy evolution for case  $\mathcal{R}_{\mathcal{N}^{2+}}^{[4-5]}$ , with 200, 300, 600 cells on a uniform grid, obtained from the wave propagation method. . . . . 94
- 4.4 Numerical intermediate solutions (dashed-marked line), exact intermediate solutions (solid line) and exact limiting solutions (dashed line) for functioning regime  $\mathcal{R}_{\mathcal{N}^{2+}}$ , computed from the polytropic van der Waals model with  $\delta = 1/50$ . The numerical solutions are computed on a uniform grid with 600 cells, by means of the first order split method based on formulation (4.4), the Roe solver of [16] and forward Euler time advance. . . . . 97
- 4.5 Numerical intermediate solutions (dashed-marked line), exact intermediate solutions (solid line) and exact limiting solutions (dashed line) for functioning regime  $\mathcal{R}_{\mathcal{N}^{1+}}$ , computed from the polytropic van der Waals model with  $\delta = 1/50$ . The numerical solutions are computed on a uniform grid with 600 cells, by means of the first order split method based on formulation (4.4), the Roe solver of [16] and forward Euler time advance. . . . . 98
- 4.6 Numerical intermediate solutions (dashed-marked line), exact intermediate solutions (solid line) and exact limiting solutions (dashed line) for functioning regime  $\mathcal{R}_{\mathcal{N}^3}$ , computed from the polytropic van der Waals model with  $\delta = 1/50$ . The numerical solutions are computed on a uniform grid with 600 cells, by means of the first order split method based on formulation (4.4), the Roe solver of [16] and forward Euler time advance. . . . . 99
- 4.7 Numerical limiting solutions (dashed-marked line) and exact limiting solutions (solid line) of density for cases  $\mathcal{R}_{\mathcal{N}^{2+}}^{[5]}$  and  $\mathcal{R}_{\mathcal{N}^{2-}}^{[5]}$  above,  $\mathcal{R}_{\mathcal{N}^{1+}}^{[4]}$  and  $\mathcal{R}_{\mathcal{N}^{1-}}^{[4]}$  below. Solutions computed from the polytropic van der Waals model with  $\delta = 1/50$ . The numerical solutions are computed on a uniform grid with 600 cells, by means of the first order split method based on formulation (4.4), the Roe solver of [16] and forward Euler time advance. . . . . 100

---

4.8	Numerical intermediate solutions (dashed-marked line), exact intermediate solutions (solid line) and exact limiting solutions (dashed line) for functioning regime $\mathcal{R}_{\mathcal{N}^{2+}}$ , computed from the polytropic van der Waals model with $\delta = 1/50$ . The numerical solutions are computed on a uniform grid with 600 cells, by means of the second order split method based on formulation (4.4), the Roe solver of [16] with van Leer limiter and the second order TVD Runge-Kutta time advance. . . . .	101
4.9	Numerical intermediate solutions (dashed-marked line), exact intermediate solutions (solid line) and exact limiting solutions (dashed line) for functioning regime $\mathcal{R}_{\mathcal{N}^{1+}}$ , computed from the polytropic van der Waals model with $\delta = 1/50$ . The numerical solutions are computed on a uniform grid with 600 cells, by means of the second order split method based on formulation (4.4), the Roe solver of [16] with van Leer limiter and the second order TVD Runge-Kutta time advance. . . . .	102
4.10	Numerical intermediate solutions (dashed-marked line), exact intermediate solutions (solid line) and exact limiting solutions (dashed line) for functioning regime $\mathcal{R}_{\mathcal{N}^3}$ , computed from the polytropic van der Waals model with $\delta = 1/50$ . The numerical solutions are computed on a uniform grid with 600 cells, by means of the second order split method based on formulation (4.4), the Roe solver of [16] with van Leer limiter and the second order TVD Runge-Kutta time advance. . . . .	103
5.1	$P$ - $v$ plane regions where reservoir couples lead to different functioning regimes. The curves are computed from the polytropic van der Waals model with $\delta = 1/50$ . . . . .	106
5.2	$T$ - $s$ plane regions where reservoir couples lead to different functioning regimes. The curves are computed from the polytropic van der Waals model with $\delta = 1/50$ . . . . .	106
5.3	Limiting solutions for representative transitional regime $\mathcal{R}_{\mathcal{M}^-}/\mathcal{R}_{\mathcal{N}^{2+}}$ , computed from the polytropic van der Waals model with $\delta = 1/50$ .107	
5.4	Limiting solutions for representative transitional regime $\mathcal{R}_{\mathcal{N}^{1+}}/\mathcal{R}_{\mathcal{N}^{2+}}$ , computed from the polytropic van der Waals model with $\delta = 1/50$ .109	
5.5	Limiting solutions for representative transitional regime $\mathcal{R}_{\mathcal{N}^{1-}}/\mathcal{R}_{\mathcal{N}^{2-}}$ , computed from the polytropic van der Waals model with $\delta = 1/50$ .110	
5.6	Rarefaction shock region computed from the polytropic van der Waals model with $\delta = 1/50$ . The DSL line collects all the states which could be connected by a double sonic shock. The PSV line collects post-shock states of rarefaction shocks originating on the saturation curve. . . . .	111
5.7	The stagnation state is located between the $\mathcal{S}_{\mathcal{N}^+}/\mathcal{S}_{\mathcal{N}^-}$ and $\mathcal{R}_{\mathcal{N}^2}/\mathcal{R}_{\mathcal{N}^1}$ line. Sonic conditions $\rho = \rho_{s_1}$ occur before entering the RSR. Diagram computed from the polytropic van der Waals model with $\delta = 1/50$ . . . . .	112

5.8 Post-sonic compression shock exhibiting $\Gamma = 0$ at post-shock state, computed from a polytropic van der Waals model with $\delta = 1/50$ . . . . .	113
5.9 Limiting solutions for representative transitional regime $\mathcal{R}_{\mathcal{N}^{1+}}/\mathcal{R}_{\mathcal{N}^{1-}}$ , computed from the polytropic van der Waals model with $\delta = 1/50$ . . . . .	114
5.10 Limiting solutions for representative transitional regime $\mathcal{R}_{\mathcal{N}^{2+}}/\mathcal{R}_{\mathcal{N}^{2-}}$ , computed from the polytropic van der Waals model with $\delta = 1/50$ . . . . .	115
5.11 Shock adiabat through a point exhibiting null fundamental derivative, computed from the polytropic van der Waals model with $\delta = 1/50$ . The Rayleigh line corresponds to a pre-sonic shock. . . . .	116
5.12 Limiting solutions for representative transitional regime $\mathcal{R}_{\mathcal{N}^{1+}}/\mathcal{R}_{\mathcal{N}^3}$ , computed from the polytropic van der Waals model with $\delta = 1/50$ . . . . .	118
5.13 Limiting solutions for representative transitional regime $\mathcal{R}_{\mathcal{N}^{1-}}/\mathcal{R}_{\mathcal{M}^+}$ , computed from the polytropic van der Waals model with $\delta = 1/50$ . . . . .	119
5.14 $P-v$ map of functioning regimes, computed from the polytropic van der Waals model with $\delta = 1/30$ . . . . .	122
5.15 $P-v$ map of functioning regimes, computed from the polytropic van der Waals model with $\delta = 1/25$ . . . . .	122
5.16 $P-v$ map of functioning regimes, computed from the polytropic van der Waals model with $\delta = 1/20$ . . . . .	123
5.17 $P-v$ map of functioning regimes, computed from the polytropic van der Waals model with $\delta = 1/18$ . . . . .	123
A.1 Nozzle geometry. . . . .	129

# List of Tables

2.1	Classification of fluids or fluid vapors, based on the possibility for a certain fluid to display non-ideal $\Gamma$ -regions, namely those in which the fundamental derivative is positive but lower than unity, and those in which it is negative. Within the polytropic van der Waals model, the fluid class is determined only by the number of active degrees of freedom $N$ . . . . .	29
2.2	Description of isentropic patterns. Recall that, in presence of multiple sonic points, the corresponding densities are ordered as $\rho_{s_3} < \rho_{s_2} < \rho_{s_1}$ . If one sonic point only is present, it is specified as $\rho_s$ . . . . .	40
2.3	Possible isentropic patterns for the different fluid classes. . . . .	41
3.1	Possible functioning regimes for the different fluid classes. . . . .	84
A.1	Nozzle characteristics. . . . .	129



# Chapter 1

## Introduction

### 1.1 Fundamentals of non-classical gasdynamics

Most of our understanding about gasdynamics concerns flows of ideal gases with constant specific heats. For some basic problems, such as one-dimensional (1D) unsteady homoentropic flows, quasi-1D steady nozzle flows or 2D supersonic steady flows, the ideal gas assumption allows us to obtain explicit analytical relations, which often means the possibility to gain a deep insight into certain phenomena, without the need for extensive computational or experimental activity. Despite its simplicity, this model gives rather accurate results in many applications, especially at ordinary pressure and temperature conditions. However, approaching the saturated vapor curve, the model fails in predicting the physically correct behavior, from both a qualitative and a quantitative point of view. The ideal gas model is indeed applicable in dilute gas conditions and more complex thermodynamic models are needed to account for non-ideal effects. Within this context, Non-ideal compressible fluid dynamics (NICFD) is set as the branch of fluid mechanics specialized in the study of fluid flows largely deviating from ideal conditions. The departure from the ideal gas behavior is responsible for some of the most intriguing gasdynamic phenomena, including the occurrence of expansion shocks and compression fans, which are not admissible in dilute gases with constant specific heats. Sonic and double sonic shocks, shock-splitting configurations and composite waves are other noteworthy non-classical examples. The possibility of non-classical gasdynamic phenomena is related to the sign of the quantity

$$\left( \frac{\partial^2 P}{\partial v^2} \right)_s, \quad (1.1)$$

where  $P$  is the pressure,  $v$  the specific volume and  $s$  the specific entropy, expressing the curvature of isentropes in pressure-specific volume plane. Quantity (1.1) is usually recast in non-dimensional form as the *fundamental derivative of gasdynamics*:

$$\Gamma = 1 + \frac{\rho}{c} \left( \frac{\partial c}{\partial \rho} \right)_s = \frac{v^3}{2c^2} \left( \frac{\partial^2 P}{\partial v^2} \right)_s, \quad (1.2)$$

in which  $c$  is the speed of sound. Classical gasdynamics, be it ideal or non-ideal, roots in the assumption that (1.1) or equivalently (1.2) is positive.

Fluids exhibiting negative- $\Gamma$  regions are commonly referred to as Bethe-Zel'dovich-Thompson (BZT) fluids, due to the significant contributions by these authors. In 1942 Bethe first analyzed shock theory with general equations of state [4], obtaining the well-known result that, with third order accuracy, the entropy variation across a shock is

$$\frac{T_1}{c_1^2}[s] = \frac{1}{6}\Gamma_1\Pi^3 + O(\Pi^4), \quad (1.3)$$

where  $T$  is the temperature,  $\Pi = [P]/\rho_1 c_1^2$  is the shock strength and subscript 1 indicates the pre-shock state. Assuming  $\Gamma_1 \neq 0$ , weak shocks of compressive or expansive type are admissible if the fundamental derivative is respectively positive or negative. Both Bethe and later Zel'dovich in 1946 [41] found a negative- $\Gamma$  region, near the vapor-mixture phase boundary, in van der Waals gases with large values of specific heat. A couple of decades later, shock waves with negative pressure jump in the vapor region were analyzed by Zel'dovich and Raizer [42]. The importance of  $\Gamma$  in determining the qualitative features of certain fluid flows was discussed by Thompson in [35], who also introduced the current definition of  $\Gamma$  as the fundamental derivative of gasdynamics. The work provided an overview of the consequences of a negative fundamental derivative, for some typical gasdynamics problems such as steady isentropic flow, steady duct flow with friction, shock formation in 1D unsteady flow and weak shock theory.

In the attempt to describe non-ideal fluid dynamics phenomena, suitable equations of state are to be selected. Due to its simplicity, the van der Waals model has often been used for a qualitative description of non-ideal compressible fluids effects. For accurate predictions, more complex equation of state, such as the Soave-Redlich-Kwong, the Peng-Robinson, the Martin-Hou or the Span-Wagner models are to be employed. To date, despite the extensive theoretical effort [8, 9, 12, 15, 23, 25, 30, 37, 40], no experimental evidence of non-classical phenomena is available.

## 1.2 Internal flows of non-ideal compressible fluids

Results for steady nozzle flows of ideal gases, under the quasi-1D hypothesis, are available in every gasdynamics textbooks. This kind of flows are an essential part in the understanding of compressible fluid flows. The anomalous phenomena related to a non-classical behavior encouraged researchers to study nozzle flows in the neighborhood of the negative- $\Gamma$  region.

Thompson in [35] first showed the role of  $\Gamma$  in accelerating flows through a sonic throat. He pointed out the need for a classical throat if the fundamental derivative is positive, in contrast to a non-classical antithroat, when  $\Gamma$  is negative.

Cramer and Best in [10] observed another significant consequence of the possibility of  $\Gamma$  to change sign along an isentropic expansion. Their focus was on the Mach number variations with density, for fixed entropy and total enthalpy. For certain stagnation conditions, they found that the Mach number, which in

the ideal context is a monotone decreasing function of density, could exhibit non-monotone behavior if  $\Gamma \leq 1$ . Moreover, if the fundamental derivative assumes negative values, up to three sonic points could be simultaneously present.

Chandrasekar and Prasad [6] studied transonic nozzle flows of single phase fluids, assuming that the fundamental derivative changes its sign in the neighborhood of the throat. The behavior of the flow variables is described through a first order approximation to the flow equations, presenting a non-convex flux function. Steady sonic and rarefaction shocks are predicted to occur in this kind of flows.

Schnerr and Leidner [34] studied the diabatic flow of non-ideal compressible fluids. The flow was supposed inviscid, steady and quasi-1D. Their study, based on the van der Waals model, showed that for gases exhibiting low or negative- $\Gamma$  regions the influence of an addition of given rate of heat becomes much stronger, with respect to flows of ideal gases.

In the context of transonic flows, Kluwick [22] derived a viscous small-perturbation equation, focusing on the inviscid limit. For certain reference states the presence of multiple sonic points was confirmed, and consequences were analyzed. The qualitative layout of shocked flows in the neighborhood of the throat pointed out the impossibility of a shock free transition from subsonic to supersonic conditions, in a conventional nozzle operating in the negative- $\Gamma$  region.

Cramer and Fry [11] continued the analysis of steady flows of BZT fluids in conventional converging-diverging nozzles. The focus is on stagnation condition exhibiting three sonic points in the Mach-density relation. With an extensive use of phase planes and through an approximate model (isentropic shocks), they introduced two different type of nozzle flows. In the first one, *Type 1*, in order to attain an expansion from subsonic inlet conditions to arbitrarily large exit Mach numbers, a rarefaction shock is required downstream of the throat. In the second type, *Type 2*, a rarefaction shock is placed upstream of throat. Solutions accounting for the actual entropy jump across shock discontinuities were produced through a shock fitting technique employing a six-order Runge-Kutta algorithm.

Transonic nozzle flows of BZT fluids have been discussed again by Kluwick in [24], in the quasi-1D context and in the inviscid limit. Conventional convergent-divergent geometries were first considered, showing the impossibility of a shock-free subsonic-supersonic transition. Nozzle shapes leading to shock-free transition were then discussed. A laminar boundary layer analysis was also performed. The unusual properties of BZT fluids were shown to cause significant deviations from classical boundary layer theory. For instance, under adiabatic wall conditions, the different scaling of the Eckert number, caused by the large values of specific heat typical of BZT fluids, produces very small temperature variations across the boundary layer.

William in his master's thesis [39] performed a deep investigation of the nozzle flow types identified by Cramer and Fry [11]. His approach, designed to produce 'exact' solutions, have been undertaken also in the present work and will be described in the following. For given reservoir conditions, William computed the whole solutions layout, accounting for the actual exit boundary

condition. The present work benefits from William's thesis also of the concept of limiting and intermediate solutions, which will be essential in dealing the complex layout of nozzle solutions to BZT fluids.

### 1.3 Goal and outline of the thesis

The aim of the present work is to investigate the properties of steady nozzle flows of Bethe-Zel'dovich-Thompson fluids. The quasi-1D approximation, developed by many authors [10, 22, 11] is assumed here and it represents a simple, though insightful context in the study of non-ideal compressible fluid flows. As in [39], the solutions to nozzle flows produced in the present work are referred to as exact solutions. As a matter of fact, the governing differential equations can be analytically integrated, leading to a set of algebraic, possibly implicit, equations defining the evolution of the thermodynamic and kinematic variables. Shock discontinuities are accounted for through the system of algebraic equations containing the well-known jump relations [36]. Therefore the exact computation procedure involves solving at most nonlinear systems of algebraic equations, with the desired accuracy if an explicit solution is not available.

The present work is organized as follows. Chapter 2 presents the fundamental tools used to compute exact solutions. The mathematical problem, i.e. the quasi-1D approximation for the Euler equations, is addressed. The choice of a suitable thermodynamic model, necessary to close the problem, is discussed. A general solution is seen to be composed of isentropic portions, satisfying the differential equations, matched with shock waves. Three essential tools for inspecting isentropic nozzle flows are detailed: the Mach number dependence on density, the flux function and the phase plane. The same approach was exploited by Chandrasekar and Prasad [6], Cramer and Best [10], Kluwick [22], Cramer and Fry [11], in studying nozzle flows of non-ideal fluids. The central concept of isentropic pattern is then introduced. This idea is used here to identify the global features of the isentropic flow, related to a given choice of stagnation conditions. With respect to shocked flow, the jump relations are recalled, together with the admissibility criteria.

Chapter 3 is the core of the present work. The difference between limiting and intermediate solutions is detailed, together with the computational procedure to identify both of them. The well-known results from nozzle flows of ideal gases support the exposition. The difficulties related to nozzle flows of BZT fluid are discussed. The presence of up to three sonic points, along an isentropic expansion, is the main difference with flows of ideal gases. The nozzle is considered as a discharging device between a reservoir and a stationary atmosphere with fixed pressure. A monotonic decrease in the exhaust pressure produces a specific sequence of solutions, identifying the functioning regime. Being a generic solution piecewise isentropic, a given regime exhibits different isentropic patterns. Particular attention is paid to the shock-induced transitions among the fore-mentioned isentropic patterns. In §4, a comparison between exact solutions and numerical solutions produced by a shock capturing method is performed. Some simple numerical techniques are discussed and a suitable combination of them is

implemented in a novel quasi-1D code for non-ideal compressible fluid dynamics. Both first and second order numerical results are presented and discussed.

In §5, the conditions resulting in the transition between the different functioning regimes are investigated. This procedure has the purpose of defining a thermodynamic map of functioning regimes. The map describes the regions, in a thermodynamic plane, such as pressure-specific volume, where different reservoir conditions result in each functioning regime. Conclusions and possible future developments are presented in §6.



## Chapter 2

# Nozzle flows of non-ideal fluids

In this chapter the equations modeling the quasi one-dimensional steady flow of a mono-component fluid are briefly recalled, assuming that viscous effects, thermal conductivity and body forces are negligible. The mathematical statement needs a closure, provided by the constitutive relation describing the fluid material. To this purpose a suitable thermodynamic model allowing for non-ideal phenomena is introduced. A distinction between fluid categories, according to the values of  $\Gamma$  they can possibly assume, is recalled. The essential tools for studying isentropic and shocked flows are detailed.

### 2.1 Governing equations for steady, quasi-1D flows

The quasi-one-dimensional approach is introduced here to study steady nozzle flows of non-ideal compressible fluids. Applicability of the quasi-1D approximation requires the following conditions to be met [36]:

- The effects of viscosity, thermal diffusion and body forces are all negligible.
- At any streamwise location  $x$  the radius of curvature of the nozzle axis is large compared to the nozzle cross-sectional length (the radius or the semi-height for an axisymmetric or 2D nozzle respectively).
- The cross sectional area  $A(x)$  is a smooth function of  $x$  with slight variation:  $\frac{A'(x)}{\sqrt{A(x)}} \ll 1$ .

Thus all properties are assumed to vary only along the streamwise direction and the governing equations for a steady flow can be written as

$$\begin{cases} \frac{d}{dx} (\rho u A(x)) = 0 \\ \frac{d}{dx} (\rho u^2 A(x) + P(h, \rho) A(x)) = P(h, \rho) \frac{dA(x)}{dx} \\ \frac{d}{dx} \left( h + \frac{1}{2} u^2 \right) = 0, \end{cases} \quad (2.1)$$

where  $\rho$ ,  $P$ ,  $u$ ,  $h$  are respectively the fluid density, the pressure, the velocity and the specific enthalpy. The function  $A(x)$  represents the known cross sectional

area distribution. The problem is completed by specifying a suitable equation of state for the pressure,  $P = P(h, \rho)$ . Introducing the mass flow rate  $\dot{m} = \rho u A(x)$ , the specific entropy  $s$  and the specific total enthalpy  $h^t = h + u^2/2$ , Eqs. (2.1) can be conveniently rewritten as

$$\begin{cases} \frac{d\dot{m}}{dx} = 0 \\ \frac{ds}{dx} = 0 \\ \frac{dh^t}{dx} = 0. \end{cases} \quad (2.2)$$

From this set of equations we can infer that the mass flow rate, the specific entropy and the specific total enthalpy are all constant along the nozzle axis.

However, the interest is on solutions possibly containing discontinuities, i.e. weak solutions to Eqs. (2.1), as defined for instance in [29]. Two types of fluid dynamic discontinuities can be distinguished: shock waves, having non-zero mass flux through the discontinuity itself and contact discontinuities, in which the mass flux is zero, since fluid on both sides of the jump moves with the same speed of the discontinuity. However, considering a contact discontinuity in a the steady quasi-1D flow is meaningless, since it implies zero velocity on both sides and, in turn, zero mass flow rate throughout the nozzle. Therefore, in the following, all discontinuities are assumed to be shock waves. Discontinuities between isentropic branches have to satisfy the steady 1D version of the Rankine-Hugoniot jump relations [36]

$$\begin{cases} \rho_1 u_1 = \rho_2 u_2 \\ P_1 + \rho_1 u_1^2 = P_2 + \rho_2 u_2^2 \\ h_1 + \frac{1}{2} u_1^2 = h_2 + \frac{1}{2} u_2^2, \end{cases} \quad (2.3)$$

where subscript 1 and 2 denote the upstream and downstream side of the shock. From the third equation of (2.3) one can easily conclude that, despite the entropy does not remain constant across discontinuities, the total enthalpy does. System (2.3) is to be equipped with the entropy and speed ordering admissibility criteria, as it will be explained in detail in §2.4.1.

## 2.2 The thermodynamic model employed

The problem addressed in §2.1 is complete once the equation of state for the pressure is specified. The polytropic van der Waals model is used here as the most simple thermodynamic model allowing for non-ideal effects, such as a non-constant (especially negative) fundamental derivative of gasdynamics and the liquid-vapor transition. The term polytropic refers to a constant  $c_v = (\partial e / \partial T)_v$ , the specific heat at constant volume. Despite being rather quantitatively inaccurate, this thermodynamic model provides qualitatively correct predictions which, together with its simplicity, make it very suitable for a deep investigation in the qualitative features of non-ideal compressible fluid flows.

The van der Waals equation of state was obtained through improvement of the Ideal Gas equation of state [5]. The corrections concern the molecules, which are no more considered as point particles, and the existence of forces between the molecules. The van der Waals thermal equation of state is

$$P(T, v) = \frac{RT}{v - b} - \frac{a}{v^2},$$

where  $T$  and  $v$  are respectively the temperature and the specific volume. The coefficient  $R = R_u/M$  is the gas constant, in which  $R_u$  is the universal gas constant and  $M$  is the molar mass. The parameters  $a$  and  $b$  are related to the forementioned corrections. The critical point coordinates, denoted with subscript  $c$ , relate to these parameters:

$$P_c = \frac{a}{27b^2}, \quad T_c = \frac{8a}{27bR}, \quad v_c = 3b.$$

The thermal equation of state is not sufficient to characterize the thermodynamic system completely, insofar as a second equation of state, namely the caloric equation  $e(T, v)$  for the specific internal energy  $e$ , has not yet been given. The caloric equation  $e(T, v)$  cannot be given in a completely independent manner from  $P(T, v)$ , for thermodynamic formalism requires the two equations of state to satisfy the consistency condition [5]

$$\left( \frac{\partial e}{\partial v} \right)_T = T \left( \frac{\partial P}{\partial T} \right)_v - P(T, v)$$

Therefore, in the polytropic case the caloric equation of state is

$$e(T, v) = e_0 + c_v T - \frac{a}{v}$$

where  $e_0$  is the value of the specific internal energy in a suitable reference state. It is standard practice to consider reduced quantities as follows

$$\hat{P} = \frac{P}{P_c}, \quad \hat{T} = \frac{T}{T_c Z_c}, \quad \hat{v} = \frac{v}{v_c}, \quad \hat{e} = \frac{e}{P_c v_c}, \quad \hat{s} = \frac{s}{R}, \quad \hat{c}^2 = \frac{c^2}{P_c v_c}.$$

As usual  $s$  and  $c$  stand respectively for the specific entropy and for the speed of sound. Similar reductions are considered for other thermodynamic quantities, such as the specific enthalpy or Gibbs potential. The quantity  $Z_c$  is the critical compressibility factor,  $Z_c = (P_c v_c)/(RT_c) = 3/8$ . Introducing the dimensionless reciprocal specific heat

$$\delta = \frac{R}{c_v},$$

the two equations of state are recast in reduced form as

$$\begin{aligned} \hat{P}(\hat{T}, \hat{v}) &= \frac{\hat{T}}{\hat{v} - \hat{b}} - \frac{\hat{a}}{\hat{v}^2}, \\ \hat{e}(\hat{T}, \hat{v}) &= \hat{e}_0 + \frac{\hat{T}}{\delta} - \frac{\hat{a}}{\hat{v}}, \end{aligned}$$

where  $\hat{a} = 3$  and  $\hat{b} = 1/3$ . Therefore, the complete polytropic van der Waals model in reduced form depends only on the value of the dimensionless reciprocal specific heat  $\delta$ . Other relevant equations of state, such as those for the specific entropy and the speed of sound are respectively

$$\begin{aligned}\hat{s}(\hat{T}, \hat{v}) &= \hat{s}_0 + \frac{1}{\delta} \ln \hat{T} + \ln(\hat{v} - \hat{b}), \\ \hat{c}^2(\hat{T}, \hat{v}) &= \frac{(\delta + 1)\hat{T}\hat{v}^2}{(\hat{v} - \hat{b})^2} - \frac{2\hat{a}}{\hat{v}},\end{aligned}$$

where  $s_0$  is the specific entropy value in the reference state. The fundamental derivative of gasdynamics is computed by its definition

$$\begin{aligned}\Gamma(\hat{s}, \hat{v}) &= \frac{v^3}{2c^2} \left( \frac{\partial^2 P}{\partial v^2} \right)_s = \frac{\hat{v}^3}{2\hat{c}^2} \left( \frac{\partial^2 \hat{P}}{\partial \hat{v}^2} \right)_{\hat{s}} \\ &= \frac{\hat{v}}{2} \frac{(\delta + 1)(\delta + 2)(\hat{v} - \hat{b})^{-(\delta+3)} e^{\delta(\hat{s}-\hat{s}_0)} - 6\hat{a}\hat{v}^{-4}}{(\delta + 1)(\hat{v} - \hat{b})^{(-\delta+2)} e^{\delta(\hat{s}-\hat{s}_0)} - 2\hat{a}\hat{v}^{-3}}.\end{aligned}$$

### 2.2.1 LMC, HMC and BZT fluids

Given its primary importance in non-classical gasdynamics, a fluid classification is introduced, according to the minimum value of the fundamental derivative a certain fluid can assume. Among the others, one simple way to describe the role of  $\Gamma$  is the analysis of shocks formation in homoentropic 1D unsteady flows [35]. Considering a simple wave, the speed of a weak pressure disturbance is  $w = u + c$ , being  $u$  the local velocity and  $c$  the local speed of sound. These quantities vary according to

$$\frac{du}{dP} = \frac{v}{c}, \quad \frac{dc}{dP} = \frac{v}{c}(\Gamma - 1), \quad \frac{dw}{dP} = \frac{v}{c}\Gamma$$

The local velocity increases on isentropic compression and decreases on isentropic expansion. The two limiting values of the fundamental derivative, namely  $\Gamma = 1$  and  $\Gamma = 0$ , rule the variation in the speed of sound and in the wave speed. Three types of behavior can be distinguished:

- $\Gamma > 1$ : the speed of sound increases on isentropic compression and decreases on isentropic expansion. Compression waves steepen to form a compression shock, while expansion waves spread out, see Fig. 2.1a.
- $0 < \Gamma < 1$ : the speed of sound decreases on isentropic compression and increases on isentropic expansion. However, the decrease in speed of sound is overcompensated by the increase in local velocity. Therefore, compression and expansion waves respectively steepen and spread out, Fig. 2.1a.
- $\Gamma < 0$ : the speed of sound decreases on isentropic compression and increases on isentropic expansion. The decrease in speed of sound exceeds the increase in local velocity. Expansion waves steepen and eventually produce expansion shocks, while compression waves spread out in compression fans, Fig. 2.1b.

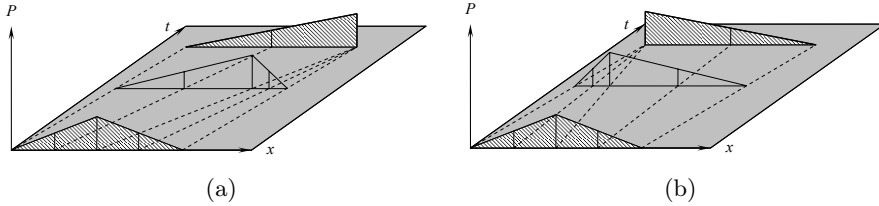


Figure 2.1: Evolution of a triangular pressure disturbance: (a)  $\Gamma > 0$ , formation of a compression shock; (b)  $\Gamma < 0$ , formation of a rarefaction shock. Taken from [31]

Following Colonna and Guardone [7], a classification of fluids or fluid vapors can be based on the possibility for a certain fluid to exhibit some or all the behaviors previously described. Considering the polytropic van der Waals model, the reduced form depends only on the dimensionless reciprocal specific heat  $\delta = R/c_v$ . According to the energy equipartition principle [5], the relation between  $\delta$  and the number  $N$  of active degrees of freedom is

$$\delta = \frac{2}{N}.$$

The value  $N$  is also referred to as the *molecular complexity*. Fig. 2.2 shows the  $\Gamma = 1$  loci for different values of the molecular complexity. The value  $N^{HMC} \simeq 7.57$  is the minimum one for which a  $\Gamma < 1$  region exists in the vapor phase, see Kluwick [24]. For this reason, vapors allowing for  $\Gamma < 1$  regions are referred to as *high molecular complexity* (HMC) fluids. In contrast, for *low molecular complexity* (LMC) fluids, the fundamental derivative always exceeds unity. Non-classical gasdynamic phenomena are related to the existence of a  $\Gamma < 0$  region in the vapor phase. Fig. 2.3 shows the  $\Gamma = 0$  loci for different values of molecular complexity. The minimum value of  $N$ , allowing the presence of a  $\Gamma < 0$  region, is  $N^{BZT} \simeq 33.33$  and it is computed in [37]. Fluids allowing for  $\Gamma < 0$  regions are referred to as *Bethe - Zel'dovich - Thompson* (BZT) fluids.

The classification proposed by the authors of [7] is summarized in Table 2.1. Here  $\Gamma_{\min}$  is the minimum value of the fundamental derivative in the vapor phase. The value  $N = 3$  is the one corresponding to a simple monoatomic gas.

Fluid	Minimum $\Gamma$ value	Interval of $N$
LMC	$\Gamma_{\min} > 1$	$3 < N \lesssim 7.57$
HMC	$0 < \Gamma_{\min} < 1$	$7.57 \lesssim N \lesssim 33.33$
BZT	$\Gamma_{\min} < 0$	$N \gtrsim 33.33$

Table 2.1: Classification of fluids or fluid vapors, based on the possibility for a certain fluid to display non-ideal  $\Gamma$ -regions, namely those in which the fundamental derivative is positive but lower than unity, and those in which it is negative. Within the polytropic van der Waals model, the fluid class is determined only by the number of active degrees of freedom  $N$ .

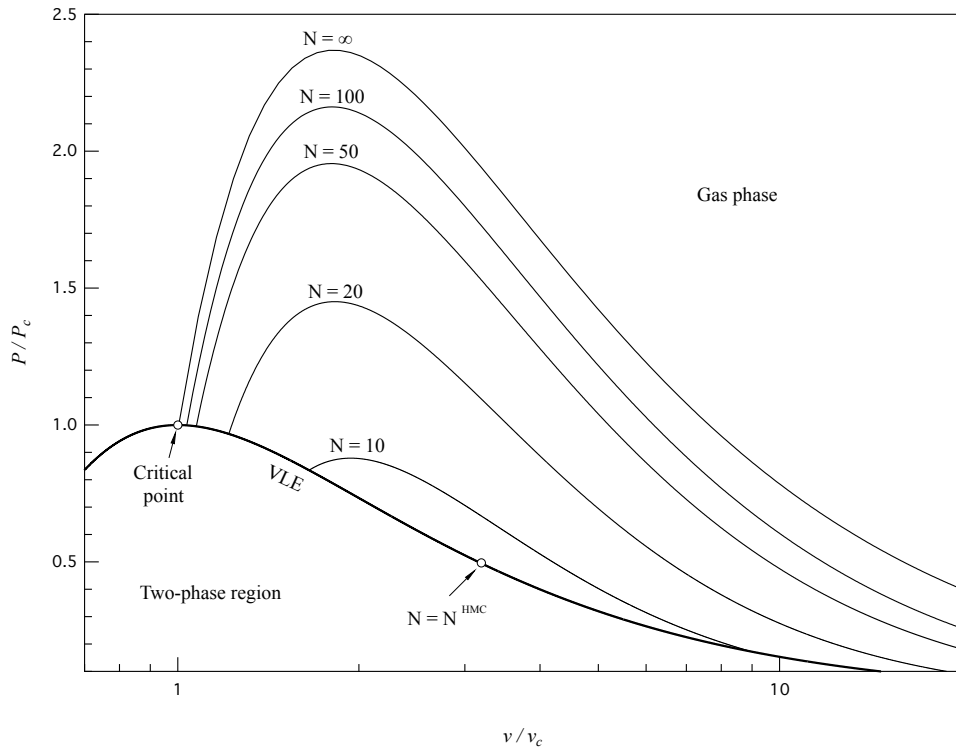


Figure 2.2:  $\Gamma = 1$  loci for different values of molecular complexity  $N$ . For  $N = N^{HMC}$  the  $\Gamma = 1$  locus reduces to a point located on the saturation curve.

## 2.3 Steady isentropic flow

Solutions to the nozzle problem are generally composed of isentropic branches matched through shocks satisfying the jump relations. This section deals with the properties of isentropic nozzle flows. Note that the present discussion extends not only to complete isentropic flows, from inlet to outlet, but also to any isentropic branches upstream or downstream of a shock discontinuity. The essential tools for inspection of isentropic flow and the concept of isentropic pattern will be introduced.

### 2.3.1 The standard differential approach

A convenient way to introduce isentropic nozzle flows is through the differential approach, which highlights the roles of the Mach number and of the fundamental derivative in the evolution of the thermodynamic and kinematic variables, along a nozzle of given geometry. System (2.1) is equivalent to

$$\begin{cases} \frac{d}{dx} (\rho u A(x)) = 0 \\ u \frac{du}{dx} + \frac{1}{\rho} \frac{dP}{dx} = 0 \\ \frac{ds}{dx} = 0, \end{cases}$$

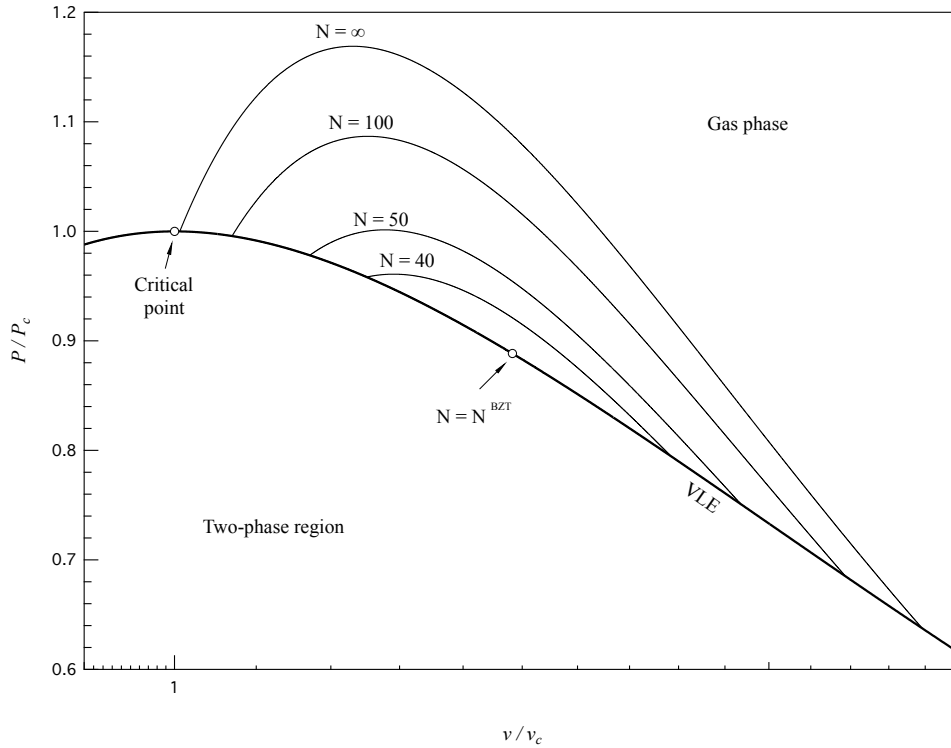


Figure 2.3:  $\Gamma = 0$  loci for different values of molecular complexity  $N$ . For  $N = N^{BZT}$  the  $\Gamma = 0$  locus reduces to a point located on the saturation curve.

By straightforward manipulation of the previous equations, the following standard relations are readily obtained [10, 11, 34]

$$\begin{aligned} \frac{1}{u} \frac{du}{dx} &= \frac{1}{M^2 - 1} \frac{1}{A} \frac{dA}{dx}, \\ \frac{1}{\rho} \frac{d\rho}{dx} &= \frac{M^2}{1 - M^2} \frac{1}{A} \frac{dA}{dx}, \\ \frac{1}{P} \frac{dP}{dx} &= \frac{1}{1 - M^2} \frac{\rho u^2}{P} \frac{1}{A} \frac{dA}{dx}, \\ \frac{1}{c} \frac{dc}{dx} &= \frac{(\Gamma - 1)M^2}{1 - M^2} \frac{1}{A} \frac{dA}{dx}, \\ \frac{1}{M} \frac{dM}{dx} &= \frac{1 + (\Gamma - 1)M^2}{M^2 - 1} \frac{1}{A} \frac{dA}{dx}. \end{aligned}$$

These relations lead to the basic features of subsonic and supersonic nozzle flow. In subsonic flows a decreasing area,  $A'(x) < 0$ , results in an expansion combined with an acceleration, whereas an increasing area produces a compression combined with a deceleration. In a supersonic flow the opposite is true.

Another classical result concerns the Mach number variation at a throat ( $A'(x) = 0$ ,  $A''(x) > 0$ ) or at an antithroat ( $A'(x) = 0$ ,  $A''(x) < 0$ ), with sonic conditions. Applying l'Hosplital's rule gives

$$\left(\frac{dM}{dx}\right)^2 \rightarrow \frac{\Gamma}{2A} \frac{d^2A}{dx^2} \quad \text{as } M \rightarrow 1 \text{ and } \frac{dA}{dx} \rightarrow 0,$$

which states that, for a subsonic-supersonic transition or vice versa, a conventional throat (antithroat) is required if the fundamental derivative is positive (negative).

### 2.3.2 Mach number variations with density

The Mach number dependence on density provides relevant information about nozzle flow properties [10, 11, 22]. The uniformity of the total enthalpy  $h^t$  gives, for the Mach number

$$M(\rho; s, h^t) = \frac{\sqrt{2[h^t - h(s, \rho)]}}{c(s, \rho)}, \quad (2.4)$$

where  $s$  and  $h^t$  have to be considered as parameters identifying stagnation conditions. Differentiation yields

$$\frac{dM}{d\rho}(\rho; s, h^t) = \frac{M(\rho; s, h^t)}{\rho} \underbrace{\left(1 - \Gamma(s, \rho) - \frac{1}{M^2(\rho; s, h^t)}\right)}_{J(\rho; s, h^t)}. \quad (2.5)$$

Therefore the sign of  $J(\rho; s, h^t)$  determines the Mach number variations with density. If the minimum value of the fundamental derivative along a given isentrope,  $\Gamma_{\min}^s(s)$ , is lower than unity, the  $J = 0$  locus is readily obtained as

$$M^{J=0}(\rho; s) = \frac{1}{\sqrt{1 - \Gamma(s, \rho)}}. \quad (2.6)$$

Different behaviors can occur depending on the values that  $\Gamma$  assumes on a given isentrope. Consider first the case of a LMC fluid. The  $M$ - $\rho$  relation is always monotone decreasing. This is the classical behavior encountered in the study of nozzle flows of a polytropic ideal gas.

Figure 2.4 shows the  $M$ - $\rho$  dependence for a HMC fluid. The different curves are all relative to the same entropy, i.e. the stagnation state corresponds to different densities along the same isentrope. The reference isentrope also enters the  $\Gamma < 1$  region, i.e.  $0 < \Gamma_{\min}^s(s) < 1$ . Therefore in the  $M$ - $\rho$  diagram the region  $J > 0$  exists. On the contrary, if the minimum value of the fundamental derivative, along the current isentrope, exceeds unity, then the diagram is qualitatively coincident with that of a LMC fluid. Note that the  $J = 0$  curve will not cross the sonic line, since  $\Gamma_{\min}^s(s) > 0$ . Curve labeled  $b$  does not enter the  $J > 0$  region and exhibits the same qualitative behavior of LMC fluids. Curves such as  $a$  show non-monotone  $M$ - $\rho$  dependence in a supersonic region. A remark has to be made on the possibility of entering the two-phase region, in an isentropic expansion. The HMC fluid considered here exhibits retrograde behavior.

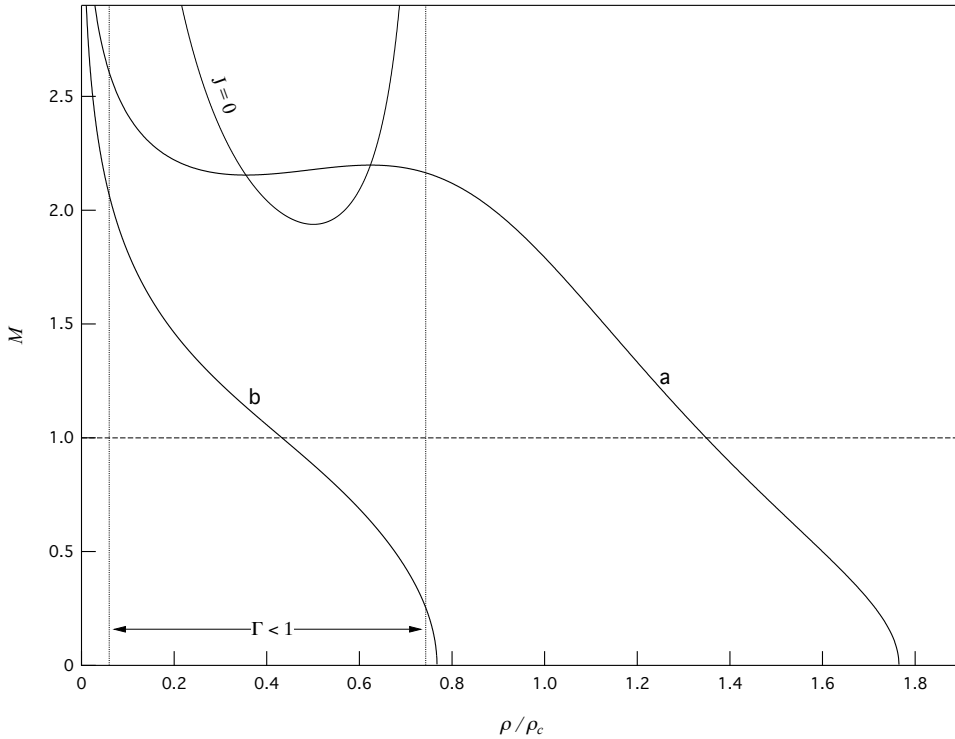


Figure 2.4: Mach number variations with density for a polytropic van der Waals gas with  $\delta = 1/10$ , which represents a HMC fluid. The different curves are relative to the same entropy. The stagnation states correspond to different densities along the same isentrope. The reference isentrope enters the  $\Gamma < 1$  region.

Denoting with  $s_{\text{vle}}$  the entropy value of the isentrope tangent to the saturation curve, if  $s > s_{\text{vle}}$  condensation along the reference isentrope typically occurs for very low density values, with respect to those related to the non-classical region, which is located near the critical point. Therefore we may regard the flow as single-phase as long as  $s > s_{\text{vle}}$ , being implied that the non-ideal phenomena we are interested in entirely occur in gas phase. Such an assumption would fail for isentropes  $s < s_{\text{vle}}$ , which cross the VLE line for density values comparable to the critical point value. Extension to such isentropes requires considering two-phase effects. Moreover, isentropes passing very close the critical point are interested by critical point phenomena. A treatment of these effects, as well as two-phase effects, is beyond the purpose of this work. However, rather than just excluding isentropes crossing the VLE line, we may consider those as well, limiting the discussion to the single-phase portions, i.e. neglecting the two-phase region in the  $M$ - $\rho$  diagram.

The more complex case of BZT fluids is illustrated in Fig. 2.5, for the exemplary case of  $\delta = 1/50$ . Again, for a comprehensive description, the reference entropy is chosen so that  $\Gamma_{\min}^s(s) < 0$ . In this case the  $J = 0$  locus crosses the sonic line, allowing for a subsonic non-monotone region. Curves  $a$  and  $d$  are similar to those encountered in the HMC case. Curves such as  $b$  enters the  $J > 0$  region for slightly supersonic Mach numbers. In the  $J > 0$  region

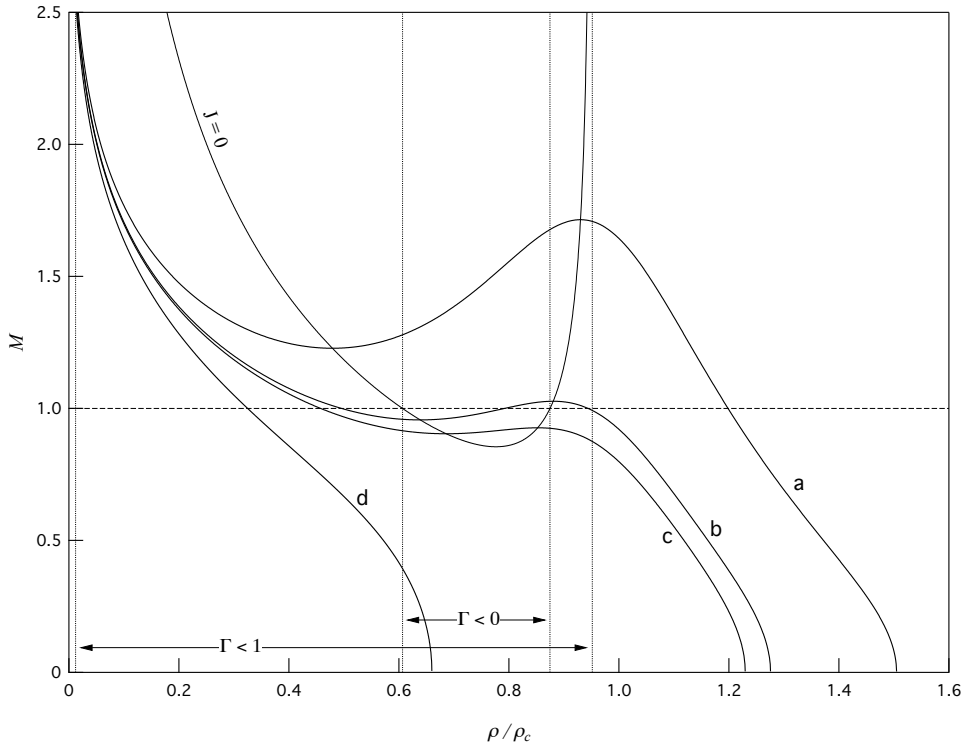


Figure 2.5: Mach number variations with density for a polytropic van der Waals gas with  $\delta = 1/50$ , which represents a BZT fluid. The different curves are relative to the same entropy. The stagnation states correspond to different densities along the same isentrope. The reference isentrope enters the  $\Gamma < 0$  region.

the decrease in Mach number with decreasing density is sufficient to cause an additional crossing of the sonic line. Then, as soon as the curve exits the  $J > 0$  region, the necessary Mach number increase with decreasing density leads to a further sonic point. Therefore curves such as  $b$  exhibit three sonic points. Curve labeled  $c$  shows a non-monotone behavior confined at subsonic values, therefore displaying only one sonic point.

Subsequent discussion will be relative to BZT fluids, given that they represent the most general case. As Fig. 2.5 clearly shows, variation of the reference entropy allows one to observe the typical behavior of a LMC or HMC fluid.

### 2.3.3 The flux function

In quasi-1D steady nozzle flows the flux function is defined as

$$f(\rho; s, h^t) = \rho u(\rho; s, h^t) = \rho \sqrt{2[h^t - h(s, \rho)]}. \quad (2.7)$$

Again, the entropy and total enthalpy have to be considered as parameters identifying stagnation conditions. Analysis by means of the flux function or mass flux has been used by Kluwick in [22], under the assumption of small perturbation with respect to sonic conditions. Indicating the flux function as

simply  $f(\rho)$ , the first and second derivatives are respectively

$$f'(\rho) = \frac{M^2 - 1}{M} c, \quad (2.8)$$

$$f''(\rho) = \left(1 - 2\Gamma - \frac{1}{M^2}\right) \frac{c}{\rho M}. \quad (2.9)$$

Therefore sonic points are stationary points of the flux function,  $f'(\rho)|_{M=1} = 0$ . Their type depends upon  $\Gamma$ , in view of  $f''(\rho)|_{M=1} = -2\Gamma c/\rho$ . A sonic point is a local maximum, minimum or stationary inflection point of  $f(\rho)$  if  $\Gamma$  is respectively positive, negative or null at that point.

Figure 2.6 shows the flux functions relative to the same stagnation conditions used to compute the curves of Fig. 2.5. The curves exhibiting one sonic point share the same qualitative behavior: a subsonic branch from stagnation, where  $f(\rho) = 0$ , to the sonic point and a supersonic branch from there to vacuum, where  $\lim_{\rho \rightarrow 0} f(\rho) = 0$ . The curve marked  $b$  shows instead three stationary points, two local maxima and a local minimum in between.

The problem of finding the density evolution along the nozzle, for given values of the entropy, the total enthalpy and the mass flow rate, can be recast in terms of a single algebraic equation involving the flux function. For given  $s$ ,  $h^t$  and mass flow rate  $\dot{m}$ , the mass balance equation is rewritten as

$$\Phi(\rho, x) = f(\rho) - \frac{\dot{m}}{A(x)} = 0, \quad (2.10)$$

where the cross sectional area is assumed to be a smooth function. If the requirements of the Implicit Function Theorem [32] are satisfied, then Eq. (2.10) is an implicit definition of  $\rho(x)$ . Given  $\Phi(\rho, x) : \mathbb{R}^2 \supset \mathcal{B} \rightarrow \mathbb{R}$ , both  $\Phi$  and  $(\partial\Phi/\partial\rho)_x$  are required to be continuous. Here we can take  $\mathcal{B} = (0, \rho_0) \times (x_{\min}, x_{\max})$ , where  $\rho_0 = \rho(s, h = h^t)$  is the stagnation density and  $x_{\min} < x < x_{\max}$ . It is easy to check that the two conditions are both satisfied, thanks to the differentiability of the flux function. For a given point  $(\rho, x)$ ,  $\Phi(\rho, x) = 0$  implicitly defines (locally) a function  $\rho(x)$  if the condition

$$\left(\frac{\partial\Phi}{\partial\rho}\right)_x \neq 0$$

is satisfied. Therefore, given that  $(\partial\Phi/\partial\rho)_x = f'(\rho)$ , Eq. (2.10) is an implicit definition of  $\rho(x)$  if the density is included between any two stationary points (which are also sonic points), or between a stationary point and an endpoint of the density interval  $(0, \rho_0]$ .

To conclude this section, a standard result for nozzle flows, the cross sectional area dependence on density, is recalled,

$$A(\rho) = \frac{\dot{m}}{f(\rho)}.$$

The two functions  $A(\rho)$  and  $f(\rho)$  are the reciprocal of each other (through  $\dot{m}$ ).

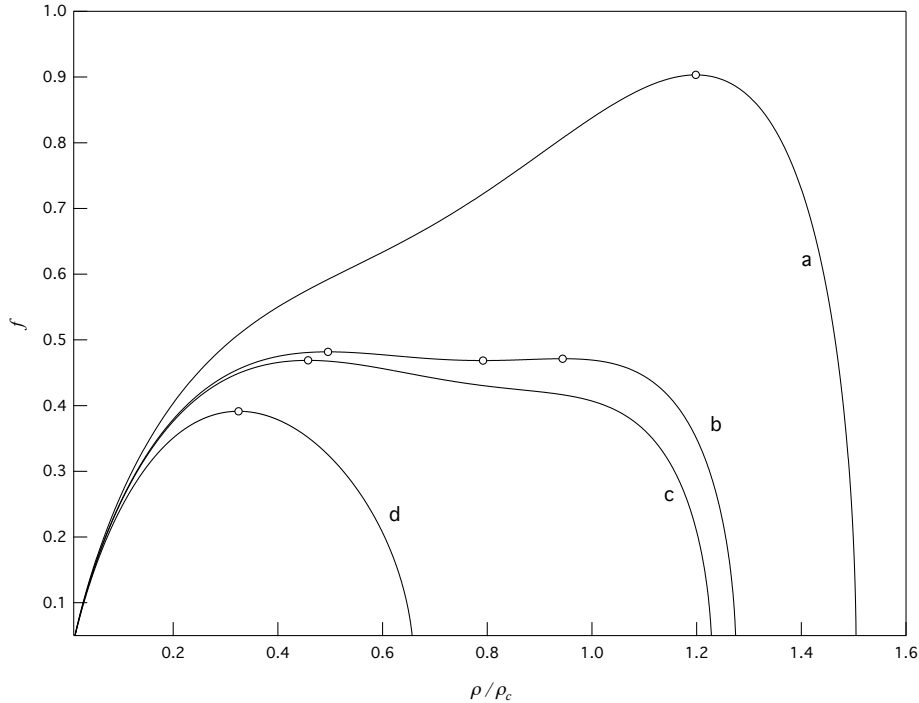


Figure 2.6: Representative flux functions for a polytropic van der Waals gas with  $\delta = 1/50$ . The different curves correspond to the stagnation states used to compute the curves of Fig. 2.5. The dots indicate sonic points, which are stationary points of the flux function.

The first and second derivatives are simply given by:

$$A'(\rho) = -\frac{f'(\rho)}{f^2(\rho)} \dot{m}$$

$$A''(\rho) = \frac{2(f'(\rho))^2 - f(\rho)f''(\rho)}{f^3(\rho)} \dot{m}.$$

A stationary point for  $f(\rho)$  is stationary for  $A(\rho)$  too, but their type is different since at a stationary point the curvature of  $A(\rho)$  and  $f(\rho)$  is opposite.

### 2.3.4 The phase plane

Strictly related to the flux function is the phase plane. The phase plane analysis provides a deep insight in the study of isentropic nozzle flows, especially when non-classical phenomena are expected [10, 11, 22, 6]. It is also a very useful tool to predict the possible isentropic and non-isentropic flows occurring in a nozzle of given geometry. The phase plane is simply a contour plot of the mass flow rate function,  $\dot{m}(\rho, x; s, h^t)$ , for given reservoir conditions in an isentropic flow. Figures 2.7, 2.8, 2.9 show the phase plane for different stagnation conditions chosen along the same isentrope. The represented function is the normalized mass flow rate:

$$\frac{\dot{m}(\rho, x; s, h^t)}{\dot{m}_c(s, h^t)}, \quad (2.11)$$

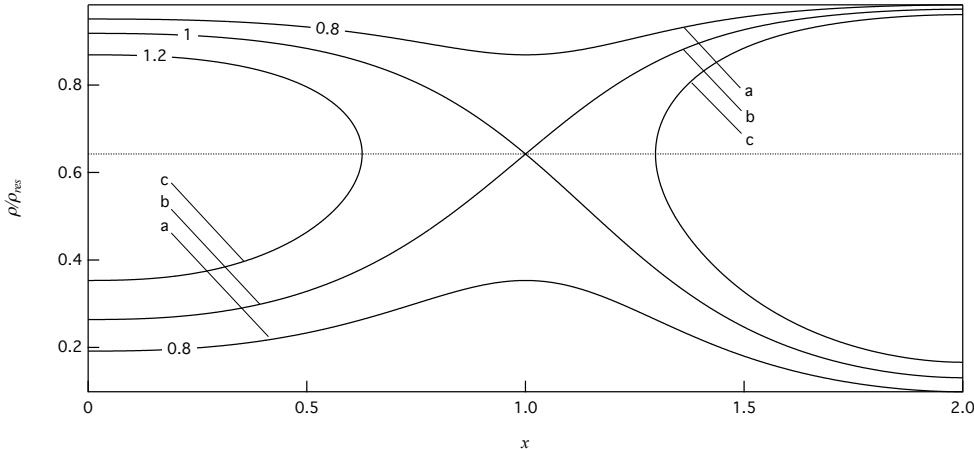


Figure 2.7: Phase plane - The stagnation conditions exhibit one sonic point only, in an isentropic expansion.

where we introduced  $\dot{m}_c$  as the critical mass flow rate,

$$\dot{m}_c = \max_{\rho} f(\rho; s, h^t) \min_x A(x). \quad (2.12)$$

Given the convergent-divergent geometry, the minimum cross sectional area is simply the area of the unique throat,  $A_t$ . The critical mass flow rate is related to the maximum mass flow rate value in an isentropic flow, see below.

The exemplary nozzle geometry used here and throughout the work is detailed in Appendix A for completeness. Figure 2.7 illustrates the phase plane for stagnation condition resulting in one sonic point only. The possible non-monotone Mach number behavior does not play a role in the qualitative shape of the contour plot. Three representative level sets are detailed:

- (a) The mass flow rate is lower than the critical value. The upper branch represents a completely subsonic flow whereas the lower one represents a completely supersonic flow.
- (b) The mass flow rate is identical to the critical value,  $\dot{m}_c$ . The throat is sonic. Subsonic-supersonic and supersonic-subsonic transition are possible together with completely subsonic and supersonic flows with sonic throat.
- (c) The mass flow rate is greater than the critical value. Following the pre-throat branch, sonic conditions occur upstream of the throat. The flow cannot be continued beyond this point.

The curves relative to a mass flow rate lower or equal to the critical value represent a possible isentropic flow from inlet to exhaust section.

Phase planes relative to stagnation conditions leading to three sonic points display the most peculiar behavior. Given the following ordering for the sonic densities:

$$\rho_{s3} < \rho_{s2} < \rho_{s1} \quad (2.13)$$

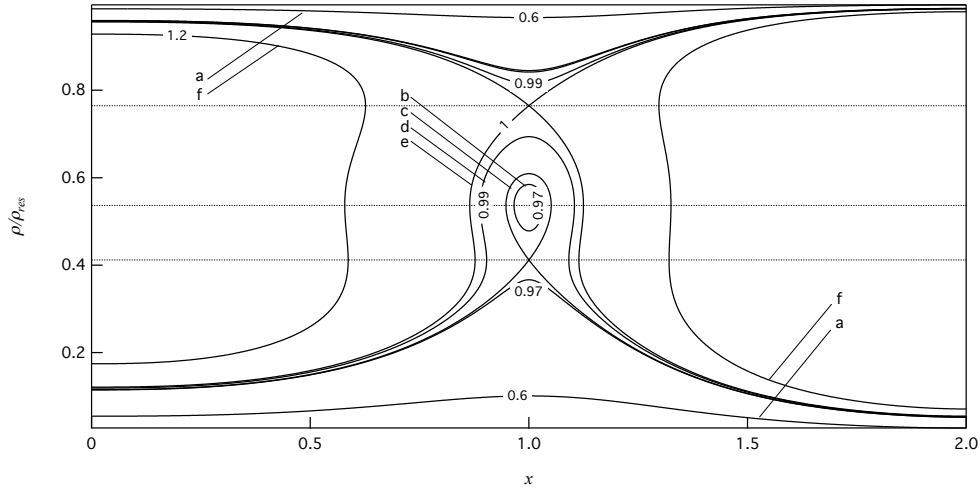


Figure 2.8: Phase plane - The stagnation conditions exhibit three sonic points, in an isentropic expansion. The largest of the sonic densities corresponds to the global maximum of the related flux function.

two different layouts can be observed depending on which of the local maxima is the global one. Figure 2.8 shows the case  $\dot{m}_c = f(\rho_{s_1})A_t$ . Here is the analysis of the representatives level sets, taken in ascending order of mass flow rate:

- (a) As in the previous case the upper branch represents a completely subsonic flow and the lower one a completely supersonic flow.
- (b) Besides the two forementioned curves, a closed isoline appears around  $\rho_{s_2}$ . This line has no physical relevance.
- (c) The mass flow rate reaches the value  $\dot{m} = f(\rho_{s_3})A_t < \dot{m}_c$ . The upper branch describes a completely subsonic flow. The supersonic branch reaches sonic throat density  $\rho_t = \rho_{s_3}$ , intersecting the closed isoline at this point. The portion of this closed line downstream of the throat could be followed up to sonic point  $\rho_{s_2}$ , in which the slope becomes infinite, the contour line turns back and the flow cannot be continued isentropically. Recalling the relation between the density and the cross-sectional area variation, see §2.3.1, a sonic point in a streamwise location different from the throat section,  $A'(x) \neq 0$ , results in an infinite density variation. Moreover, recalling the implicit definition of  $\rho(x)$ , this simply reflects that  $\Phi(\rho, x) = 0$  is no more locally satisfied as the cross sectional area is slightly increased.
- (d) The upper branch represents a completely subsonic flow. The lower branch describes a supersonic inlet. Sonic condition  $\rho_{s_3}$  is reached upstream of the throat. Also in this case the flow cannot be continued beyond this point in an isentropic flow.
- (e) The mass flow rate is equal to the critical value. Subsonic-supersonic transition is possible, passing through the sonic throat, but as in the previous

cases the flow cannot be continued as density reaches the sonic value  $\rho_{s_2}$ .

- (f) The mass flow rate is greater than the critical value. These lines have no physical relevance in isentropic flows.

A curve which is continuous from inlet to exit and does not present points with vertical slope, represents a possible isentropic flow from the inlet to the exhaust section.

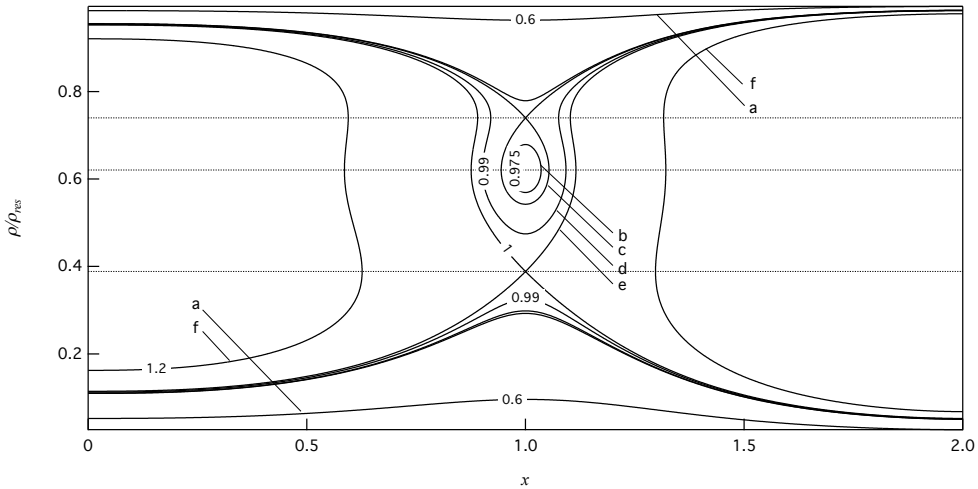


Figure 2.9: Phase plane - The stagnation conditions exhibit three sonic points, in an isentropic expansion. The lowest of the sonic densities corresponds to the global maximum of the related flux function.

Figure 2.9 describes the case  $\dot{m}_c = f(\rho_{s_3})A_t$ . The phase plane pattern appears overturned. That is, what previously happens for supersonic inlet now is for subsonic inlet and vice versa. Cramer and Fry in [11] refer to phase planes of Figs. 2.8 and 2.9 respectively as *Type-1* and *Type-2* phase planes.

### 2.3.5 Isentropic patterns

The analysis performed in the previous sections has pointed out different types of behavior, with respect to the size of the non-monotone Mach number region, the number of sonic points, the layout of the phase plane. Moreover, the choice of stagnation conditions is crucial in defining the features of an isentropic flow. The concept of *isentropic pattern* is introduced here to epitomize all the isentropic features analyzed by means of the  $M$ - $\rho$  diagram, the flux function and the phase plane. According to the previous analysis, the following patterns have been identified:

- $\mathcal{I}$ ) One sonic point and monotone decreasing  $M$ - $\rho$  relation. See curves labeled  $d$  in Figs. 2.5 and 2.6 for the  $M$ - $\rho$  diagram and the flux function; see Fig. 2.7 for the related phase plane. The name refers to the features displayed by isentropic flows of polytropic ideal gases.

- $\mathcal{M}^-$ ) One sonic point and non-monotone Mach region confined at subsonic values. See curves labeled  $c$  in Figs. 2.5 and 2.6 for the  $M$ - $\rho$  diagram and the flux function; see Fig. 2.7 for the related phase plane
- $\mathcal{M}^+$ ) One sonic points and non-monotone Mach number region confined at supersonic values. See curves labeled  $a$  in Figs. 2.5 and 2.6 for the  $M$ - $\rho$  diagram and the flux function; see Fig. 2.7 for the related phase plane.
- $\mathcal{N}^-$ ) Three sonic points are present, as in curves labeled  $b$  in Figs. 2.5 and 2.6. The global maximum of the flux function is identified by the lowest of the sonic densities, leading to a phase plane qualitatively similar to that of Fig. 2.9.
- $\mathcal{N}^+$ ) Three sonic points are present, as in the previous case. However, the global maximum of the flux function is identified by the largest of the sonic densities, leading to a phase plane qualitatively similar to that of Fig. 2.8.

The following Table 2.2 summarizes the characteristics of the different patterns.

Isentropic pattern	Number of sonic points	$J _{M<1}$	$J _{M>1}$	$\max_\rho f(\rho)$
$\mathcal{M}^+$	1	$J < 0$	$J \leq 0$	$\rho_s$
$\mathcal{N}^+$	3	$J \leq 0$	$J \leq 0$	$\rho_{s_1}$
$\mathcal{N}^-$	3	$J \leq 0$	$J \leq 0$	$\rho_{s_3}$
$\mathcal{M}^-$	1	$J \leq 0$	$J < 0$	$\rho_s$
$\mathcal{I}$	1	$J < 0$	$J < 0$	$\rho_s$

Table 2.2: Description of isentropic patterns. Recall that, in presence of multiple sonic points, the corresponding densities are ordered as  $\rho_{s_3} < \rho_{s_2} < \rho_{s_1}$ . If one sonic point only is present, it is specified as  $\rho_s$ .

In the following, the symbol ' $\mathcal{S}$ ' will be used to indicate isentropic patterns. Isentropic patterns  $\mathcal{S}_{\mathcal{I}}$ ,  $\mathcal{S}_{\mathcal{M}^+}$ ,  $\mathcal{S}_{\mathcal{M}^-}$  exhibit only one sonic point, so that, regardless of the different  $M$ - $\rho$  relation, their flux functions and phase planes are qualitatively similar. On the other hand, while patterns  $\mathcal{S}_{\mathcal{N}^+}$  and  $\mathcal{S}_{\mathcal{N}^-}$  share the qualitative  $M$ - $\rho$  dependence, their phase planes considerably differ.

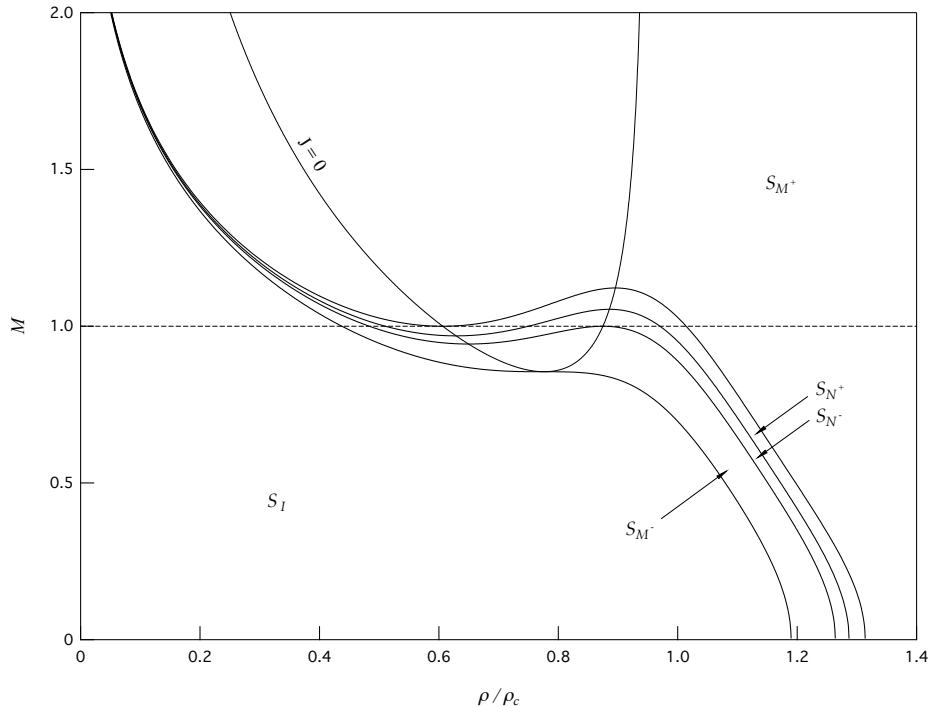
The possibility to observe, on a given isentropic flow, all the previously introduced isentropic patterns, or a given subset of them, is clearly related to the possible values assumed by the fundamental derivative along the reference isentrope. According to the fluid categories introduced in §2.2.1, Table 2.3 describes the possible isentropic patterns for the different type of fluid considered.

Boundary isentropes in  $M$ - $\rho$  diagram, computed with  $c_v/R = 50$ , are shown in Fig. 2.10. The limiting curve for  $\mathcal{S}_{\mathcal{M}^-}/\mathcal{S}_{\mathcal{I}}$  patterns is the one which intersects the  $J = 0$  locus at its minimum. Curve separating the  $\mathcal{S}_{\mathcal{M}^-}$  and  $\mathcal{S}_{\mathcal{N}^-}$  regions exhibits two sonic points. The one for higher density satisfies the condition

LMC	$\mathcal{S}_{\mathcal{I}}$
HMC	$\mathcal{S}_{\mathcal{I}}, \mathcal{S}_{\mathcal{M}^+}$
BZT	$\mathcal{S}_{\mathcal{I}}, \mathcal{S}_{\mathcal{M}^+}, \mathcal{S}_{\mathcal{N}^+}, \mathcal{S}_{\mathcal{N}^-}, \mathcal{S}_{\mathcal{M}^-}$

Table 2.3: Possible isentropic patterns for the different fluid classes.

$dM/d\rho = 0$ , i.e. it lies on  $J = 0$  locus. The present point can also be regarded as a non-simple sonic point, meaning that it is a non-simple root of equation  $M(\rho) - 1 = 0$ , since  $(dM/d\rho)|_{\rho_{s_1}} = 0$ . A slight decrease of the stagnation density causes the present sonic point to disappear, leading to isentropic pattern  $\mathcal{S}_{\mathcal{M}^-}$ . On the contrary, a slight increase of the stagnation density causes the mentioned point to separate into two distinct sonic points, resulting in pattern  $\mathcal{S}_{\mathcal{N}^-}$ . The phase plane corresponding to the current transition is shown in Fig. 2.11a. For some subsonic portions, infinite slope points are visible, for density values corresponding to the non-simple sonic point. However, they are somewhat different from what observed for  $\mathcal{S}_{\mathcal{N}^-}$  or  $\mathcal{S}_{\mathcal{N}^+}$  in Figs. 2.8 and 2.9. Indeed, in the present case the contour line doesn't turn back. This can be explained by recalling that  $J|_{M=1} = -\Gamma$ , so that this sonic density is one of the two values for which the reference isentrope crosses the  $\Gamma = 0$  line. Therefore this sonic point represents a stationary inflection point of the related flux function.

Figure 2.10: Limiting curves computed for a polytropic van der Waals gas with  $\delta = 1/50$ . The reference isentrope enters  $\Gamma < 0$  region.

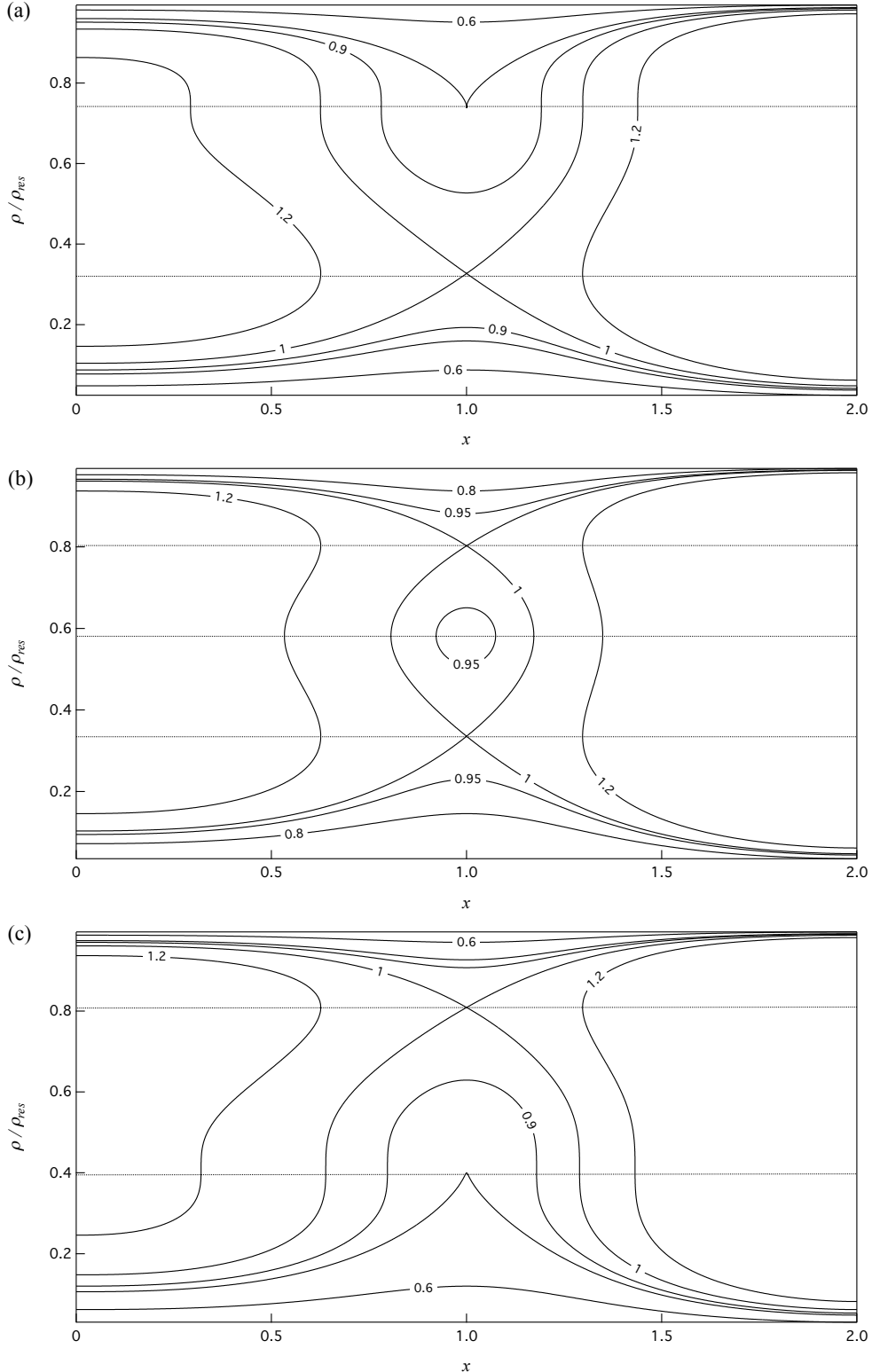


Figure 2.11: Transitional phase planes: (a)  $S_{M-}/S_{N-}$ , (b)  $S_{N-}/S_{N+}$ , (c)  $S_{N+}/S_{M+}$ , computed for a polytropic van der Waals gas with  $\delta = 1/50$ .

Transition  $\mathcal{S}_{\mathcal{N}^+}/\mathcal{S}_{\mathcal{N}^-}$  occurs when the related flux function has two local maxima with the same value, which requires  $\rho_{s_1}c(s, \rho_{s_1}) = \rho_{s_3}c(s, \rho_{s_3})$ . Phase planes for this transition exhibits two saddle points on the contour line related to the critical mass flow rate, see Fig. 2.11b. Transition  $\mathcal{S}_{\mathcal{M}^+}/\mathcal{S}_{\mathcal{M}^-}$  exhibits two sonic points, as  $\mathcal{S}_{\mathcal{M}^-}/\mathcal{S}_{\mathcal{N}^-}$ , one of which is non-simple, in the sense previously specified. In this case the non-simple sonic point is the one for lower density, i.e.  $(dM/d\rho)|_{\rho_{s_2}} = 0$ . The resulting infinite slope points in the phase plane, Fig. 2.11c, are therefore located in supersonic portions.

By collecting stagnation conditions leading to each isentropic pattern, a map of isentropic patterns can be computed in some typical thermodynamic plane, such as  $P$ - $v$  in Fig. 2.12, or  $T$ - $s$  in Fig. 2.13. The figures are relative to a BZT fluid (polytropic van der Waals model with  $c_v/R = 50$ ), so that all the isentropic patterns are simultaneously present. It is remarkable that the only geometric feature of the nozzle entering the computation of these maps, is the convergent-divergent shape. The present maps are indeed independent of the actual cross-sectional area distribution. This also relates to the assumption of considering isentropic expansion up to arbitrarily large Mach numbers. Stagnation states located above the isentrope tangent to the  $\Gamma = 1$  locus will certainly exhibit  $\mathcal{S}_{\mathcal{T}}$  isentropic pattern. When the reference isentrope enters the  $0 < \Gamma < 1$  region, high stagnation densities lead to  $\mathcal{S}_{\mathcal{M}^+}$  pattern, whereas low stagnation densities lead to  $\mathcal{S}_{\mathcal{T}}$  pattern.

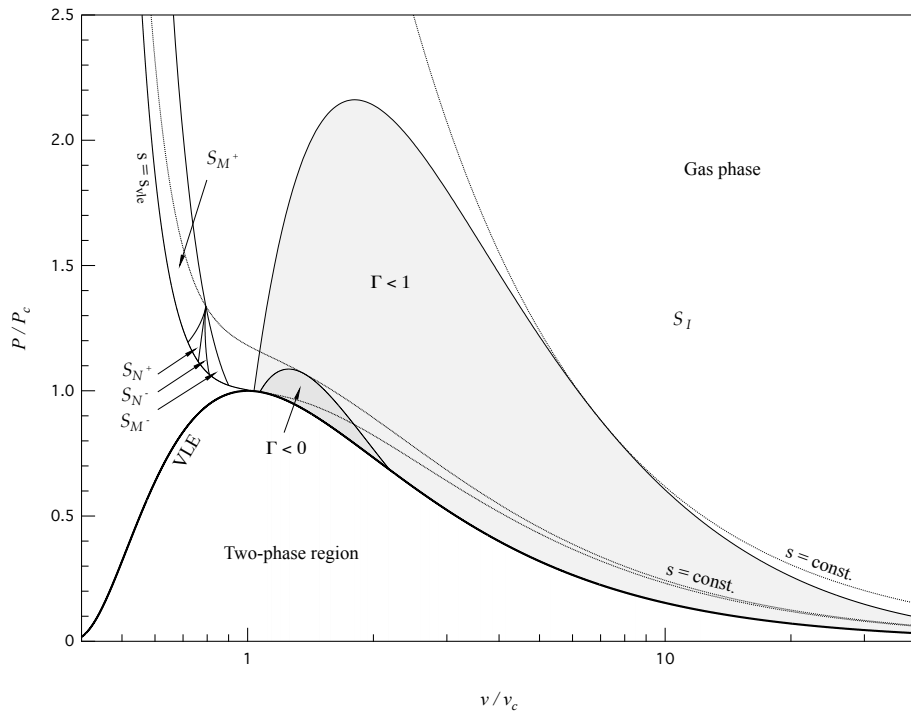


Figure 2.12:  $P$ - $v$  diagram of stagnation states leading to different isentropic patterns. The curves are computed from the polytropic van der Waals model with  $\delta = 1/50$ . The three isentropes displayed are those tangent to the VLE line, the  $\Gamma = 0$  locus and the  $\Gamma = 1$  locus.

If the reference isentrope crosses the negative- $\Gamma$  region, all the isentropic patterns are observable. Stagnation states located along the saturated vapor line are all associated to  $\mathcal{S}_{\mathcal{I}}$  behavior, despite the reference isentrope crosses the negative- $\Gamma$  region. Indeed, recalling the  $M-\rho$  diagram for BZT fluids, if the stagnation density is very close to the  $\Gamma = 0$  line, not only the negative- $\Gamma$  region will be entered with subsonic conditions, but also the  $M-\rho$  function will be monotone decreasing.

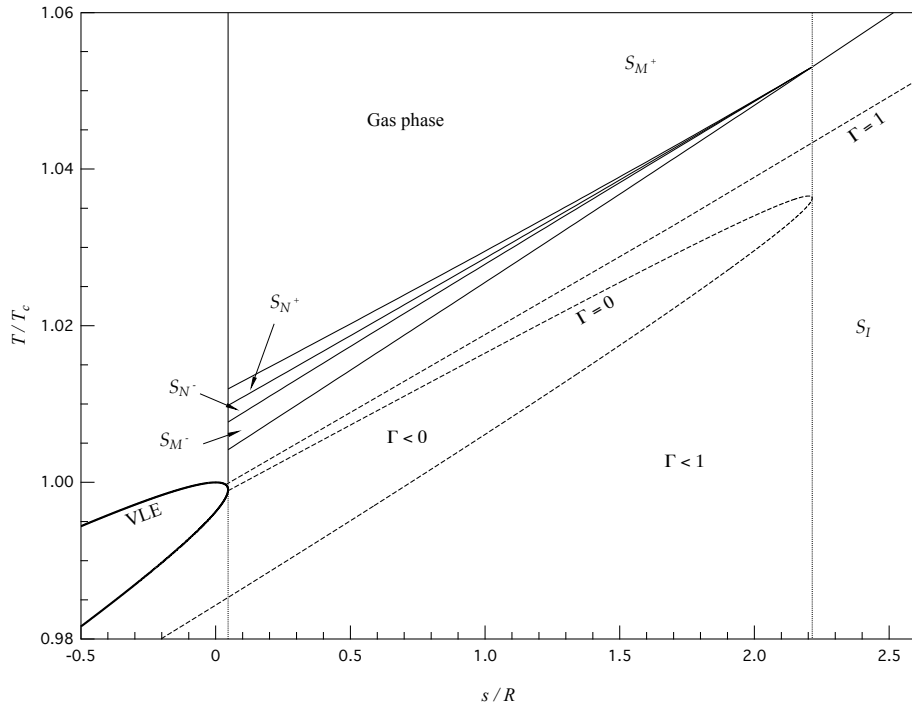


Figure 2.13:  $T$ - $s$  diagram of stagnation states leading to different isentropic patterns. The curves are computed from the polytropic van der Waals model with  $\delta = 1/50$ .

## 2.4 Steady flow with shocks

This section is devoted to the general features of shock waves in steady 1D flows. A peculiar feature of the shock adiabat, its concavity at a sonic point, proves useful in defining admissible sonic shocks. The last part of the section deals with the possible shock-induced transition of isentropic patterns.

### 2.4.1 Jump relations and admissibility conditions

The system of steady, 1-D Rankine-Hugoniot jump relations reads [36]

$$\begin{cases} \rho_1 u_1 = \rho_2 u_2 \\ P_1 + \rho_1 u_1^2 = P_2 + \rho_2 u_2^2 \\ h_1 + \frac{u_1^2}{2} = h_2 + \frac{u_2^2}{2}. \end{cases} \quad (2.14)$$

Given a pre-shock state  $(p_1, v_1, u_1)$  and dropping the subscript "2" for the post-shock state the system can be written as

$$\begin{cases} j = \frac{u_1}{v_1} \\ P = P_1 - j^2(v - v_1) \\ h(P, v) - h(P_1, v_1) - \frac{1}{2}(P - P_1)(v + v_1) = 0. \end{cases} \quad (2.15)$$

The first equation is the definition of the mass flux  $j$ ; the second one is the definition of the *Rayleigh line*  $P^R(v; P_1, v_1) = P^{R,1}(v)$ , from state 1; the third one is the implicit definition of the shock adiabat from state 1,  $P^{RH}(v; P_1, v_1) = P^{RH,1}(v)$ . Therefore it is easy to see that the post-shock state is defined by the intersection of the shock adiabat with the Rayleigh line, both from a given state 1 and for a given mass flux. From the implicit definition of the shock adiabat we can compute the first derivative of the shock adiabat [23, 9] as

$$\frac{dP^{RH,1}(v)}{dv} + j^2 = \frac{\frac{c^2}{v^2} (M^2 - 1)}{1 + \frac{[v]}{2v} G}, \quad (2.16)$$

where the symbol  $[.]$  indicates the difference between the post-shock and the pre-shock state, and

$$G = v \left( \frac{\partial P}{\partial e} \right)_v = \frac{\alpha v}{k_T c_v} = \frac{\alpha c^2}{c_P} \quad (2.17)$$

is the Grüneisen parameter. In the above expression  $\alpha$  is the coefficient of thermal expansion,  $k_T$  is the isothermal compressibility and  $c_P$  is the specific heat at constant pressure. For the computation of this derivative see Appendix B. The condition

$$1 + \frac{[v]}{2v} G = 0 \quad (2.18)$$

is the singularity that limits the maximum possible density increase across a compression shock, for a positive coefficient of thermal expansion, see Kluwick [22]. Subsequent discussion will be restricted to the portion of the shock adiabat to the right of the singularity.

System (2.15) must be complemented with three admissibility criteria. The first one stems from the second law of thermodynamics and requires that the jump of specific entropy across a shock must not be negative:

$$[s] \geq 0. \quad (2.19)$$

Application of the  $T$ - $ds$  relation,

$$Tds = de + Pdv,$$

across the shock gives

$$\begin{aligned} \int_{(1)}^{(2)} T^{RH,1} ds &= [e] + \int_{(1)}^{(2)} P^{RH,1} dv \\ &= -\frac{P_1 + P_2}{2}[v] + \int_{(1)}^{(2)} P^{RH,1} dv. \end{aligned}$$

That is:

$$A_{RH,1} - A_{R,1} \geq 0, \quad (2.20)$$

where  $A_{RH,1}$  and  $A_{R,1}$  are the areas under the shock adiabat and the Rayleigh line. The second admissibility condition concerns the shock stability and is known as the speed ordering condition [27, 26],

$$M_1 \geq 1 \geq M_2. \quad (2.21)$$

Moreover, in view of Eq. (2.16) and  $\frac{dP^{R,1}}{dv} = -j^2$ , fulfillment of the speed ordering condition requires

$$\left. \frac{dP^{RH,1}}{dv} \right|_{v_1} \geq \left. \frac{dP^{R,1}}{dv} \right|_{v_1} \quad \text{and} \quad \left. \frac{dP^{RH,1}}{dv} \right|_{v_2} \leq \left. \frac{dP^{R,1}}{dv} \right|_{v_2}, \quad (2.22)$$

where equalities hold for sonic pre- or post-shock states.

Finally, analysis of the internal dissipative shock structure provides the additional requirement that the Rayleigh line of an admissible shock must not cut the shock adiabat in interior points [23]. The issue of admissibility can be summarized as follows:

- An admissible compression shock requires the Rayleigh line to lie completely above the shock adiabat.
- An admissible rarefaction shock requires the Rayleigh line to lie completely below the shock adiabat.

#### 2.4.2 Flux function and sonic shocks

As we have seen in the related section, phase planes for BZT fluids can exhibit branches including points beyond which the flow cannot be continued isentropically. These are all sonic points located upstream or downstream of the throat. In terms of flux function, they are local minima or maxima, in which  $\Gamma \neq 0$ . The situation is different for stationary inflection points, in which  $\Gamma = 0$ . Indeed we have seen, for instance in Fig. 2.11a, that the contour doesn't turn back and, in principle, the flow can be continued isentropically. Let us focus then on local minima or maxima of a generic flux function. Appendix B provides the following result for the shock adiabat concavity at a sonic point:

$$\frac{v^3}{c^2} \left. \frac{d^2 P^{RH,1}(v)}{dv^2} \right|_{M=1} = \frac{2\Gamma}{1 + \frac{[v]}{2v} G}. \quad (2.23)$$

Here, for ease of notation, variables with no subscript stand for post-shock quantities, that is  $c = c^{RH,1}(v)$ ,  $\Gamma = \Gamma^{RH,1}(v)$  and so on. The denominator of the right hand side of the previous equation is positive, see §2.4.1. We recall also that, at the pre-shock state, the shock adiabat shares a second order contact with the pre-shock isentrope. Consider a generic compression (rarefaction) shock: admissibility requires the Rayleigh line from pre-shock to post-shock state to lie above (below) the shock adiabat. Consider now a sonic shock: the Rayleigh line is tangent to the adiabat. If the shock adiabat at this point is concave upward (downward) the tangent lies locally below (above). Then, in a compression shock, a sonic point (pre or post-shock) is admissible if the shock adiabat at that point is concave downward, which requires  $\Gamma$  to be negative at that point. Conversely, in a rarefaction shock, a sonic point (pre or post-shock) is admissible if the shock adiabat at that point is concave upward, which requires  $\Gamma$  to be positive at that point. A double sonic shock, which can be of rarefaction type only, will then connect two states of positive  $\Gamma$ . If the post-shock fundamental derivative is null, higher order derivatives should be computed to rule out the possible non-admissible sonic shocks.

Consider a shock with pre-shock (post-shock) state corresponding to a local minimum or maximum of pre-shock (post-shock) flux function. The shock exhibit therefore an upstream or downstream sonic state. An example of such a situation has been previously mentioned. Indeed, moving along a contour line of certain phase planes for BZT fluids, a sonic point is present upstream or downstream of the throat section. The flow cannot be continued isentropically and a shock with upstream sonic state is required [11, 22]. From the analysis of the flux function, see §2.3.3, we concluded that a sonic point is a local maximum or minimum of  $f(\rho)$  if  $\Gamma$  is respectively positive or negative, at that point. This leads to the following result: any admissible shock with pre-shock (post-shock) state corresponding to a local *maximum* of the pre-shock (post-shock) flux function is of *rarefaction* type only; any admissible shock with pre-shock (post-shock) state corresponding to a local *minimum* of the pre-shock (post-shock) flux function is of *compression* type only.

### 2.4.3 Isentropic pattern transitions

Solutions to steady nozzle flows are composed by branches in which entropy and total enthalpy do not vary along the nozzle axis, and this portions are matched by the Rankine-Hugoniot jump relations. Moreover, across any stationary shocks the total enthalpy jump is null, so that this quantity is indeed uniform over the entire nozzle. In this respect, the  $M-\rho$  diagram for fixed total enthalpy represents a useful tool to describe the isentropic portions and the possible variations in isentropic patterns across discontinuities. An example is given by Fig. 2.14, which shows isentropes relative to stagnation states chosen along a given isenthalpic (the stagnation isenthalpic). The advantage of a similar representation, over that of the §2.3.2, is that the isentropic portions are now observable on the same diagram, since the presence of a discontinuity will cause to change the reference isentrope at constant total enthalpy.

Considering a given stagnation isenthalpic curve, every intersecting isentrope

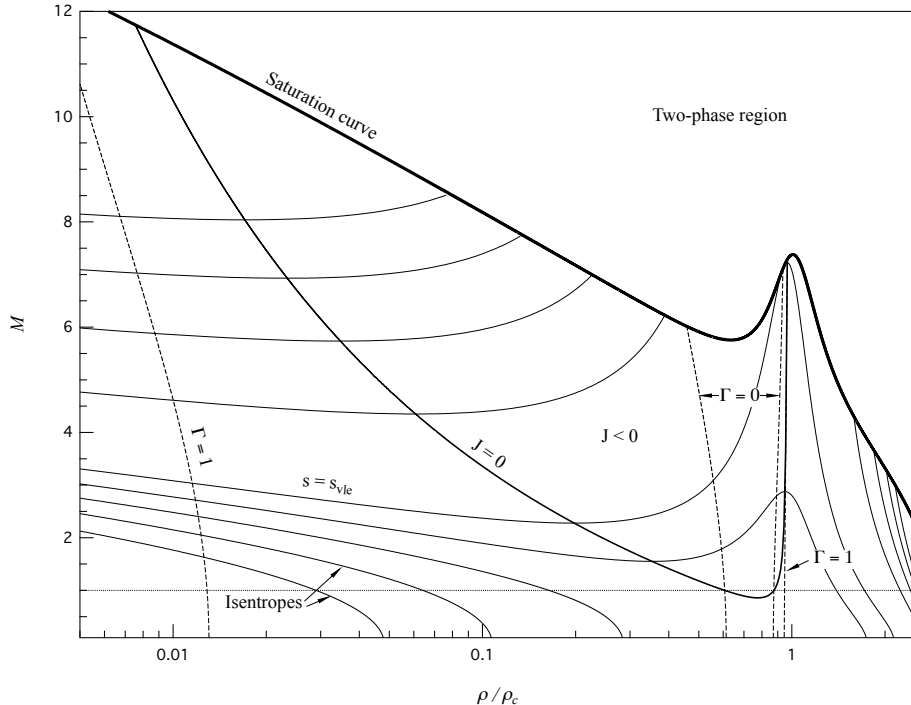


Figure 2.14: Mach number variations with density for a polytropic van der Waals gas with  $\delta = 1/50$ . The stagnation states correspond to different densities along the same isenthalpic. The different isentropes represent possible expansion or compression with the same total enthalpy.

represents a possible isentropic compression or expansion. As previously noted, we may regard the process as single-phase if  $s > s_{vle}$ . Indicating with  $s^{\text{sat}}(\rho)$  the entropy value on the saturation curve, for every density value we can compute the Mach number at a phase boundary, along an isentropic expansion with fixed specific total enthalpy  $h^t$ , as

$$M^{\text{sat}}(\rho; h^t) = \frac{\sqrt{2[h^t - h(s^{\text{sat}}(\rho), \rho)]}}{c(s^{\text{sat}}(\rho), \rho)}. \quad (2.24)$$

The saturation curve in Fig. 2.14 collects all such points. The figure is computed with a  $c_v/R = 50$  and the stagnation isenthalpic is such that the full non-ideal behavior of BZT fluids is involved, i.e. the  $J > 0$  locus extends to subsonic Mach number values. Then, varying the reference entropy, we expect all the isentropic patterns to be observed.

Boundary curves are shown in Fig. 2.15. These curves have the same significance of the boundary curves previously computed under the assumption of fixed entropy, Fig. 2.10. In the present case, boundary curves are relative to different entropy values, but share the same stagnation isenthalpic. The picture now described points out the possible transitions which isentropic patterns can undergo across a shock discontinuity. An admissible shock requires entropy to increase, so that a change in the reference isentrope has to be accompanied by

a decrease in the stagnation density. This can be seen from

$$\left( \frac{\partial \rho}{\partial s} \right)_h = -\frac{1}{v^2} \left( \frac{\partial v}{\partial s} \right)_h = -\frac{\rho T(1+G)}{c^2} < 0, \quad (2.25)$$

Therefore, with reference to Fig. 2.15, given the layout of the regions where different isentropic patterns take place, the following result holds for the possible transitions of isentropic patterns, due to the occurrence of a shock:

$$\mathcal{S}_{M^+} \Rightarrow \mathcal{S}_{N^+} \Rightarrow \mathcal{S}_{N^-} \Rightarrow \mathcal{S}_{M^-} \Rightarrow \mathcal{S}_I. \quad (2.26)$$

It is implied that the transition is not required to occur between two consecutive isentropic patterns. This result, obtained here from the polytropic van der Waals gas with  $c_v/R = 50$ , is closely related to the shape of the two relevant thermodynamic regions for non-ideal fluid flows, namely the  $\Gamma < 1$  and the  $\Gamma < 0$  regions. With decreasing or increasing value of molecular complexity the two regions respectively reduce and enlarge. Nevertheless, their qualitative features remain unchanged. Even though no proof is provided here, this strongly suggest that the same layout of Fig. 2.15 and the same ordering relation (2.26) hold for different values of molecular complexity.

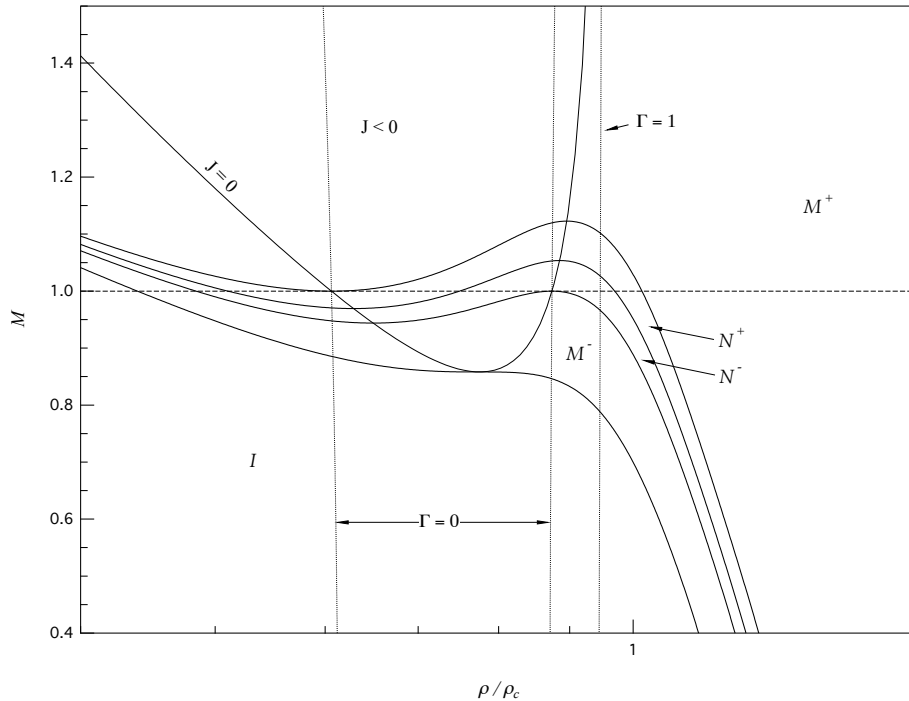


Figure 2.15: Mach number variations with density for a polytropic van der Waals gas with  $\delta = 1/50$ . Limiting curves for different isentropic patterns. The curves are relative to the same total enthalpy.

To complete the description of this type of diagram, the saturation curve variation with total enthalpy is shown in Fig. 2.16. The limiting curve is the one for which the reference isenthalpic is tangent to the vapor dome.

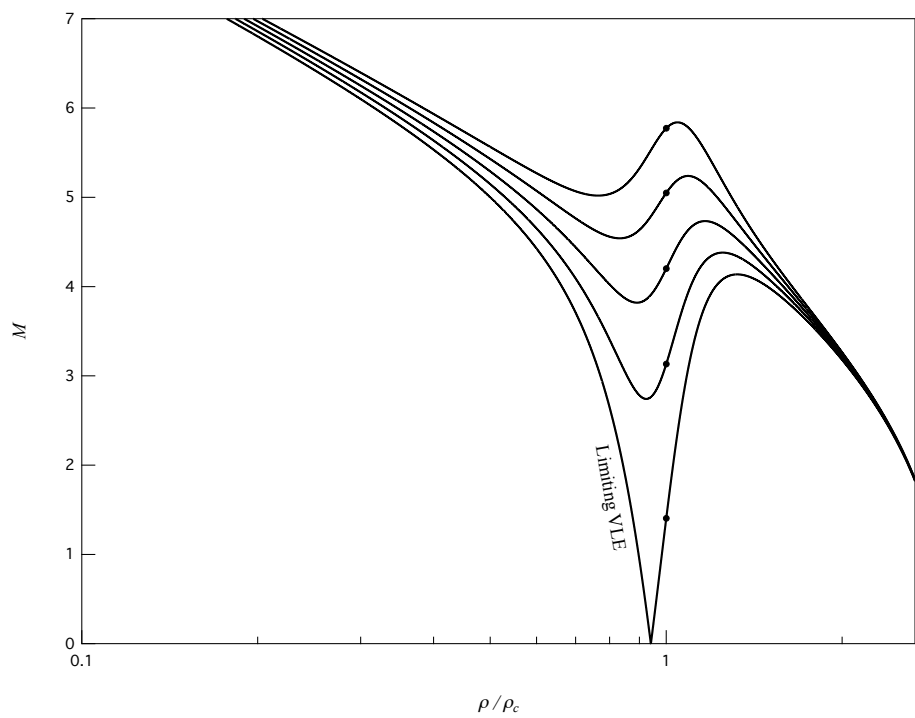


Figure 2.16: Saturation curve  $M^{\text{sat}}(\rho, h^t)$ . Effect of varying the reference total enthalpy.

# Chapter 3

## Exact solutions to quasi-1D steady nozzle flows

This section presents the exact solutions and possible functioning regimes for a convergent-divergent nozzle operating with LMC, HMC and BZT fluids. The computation method is claimed to be exact. A simple analytical integration of Eq. (2.2) allows one to compute the isentropic portions of the solutions. The problem is then recast as a single algebraic equation for the density, namely Eq. (2.10). The isentropic portions are matched by shock discontinuities, which have to satisfy the algebraic set of equations representing the jump relations, subject to admissibility criteria, see §2.4.1. Therefore the procedure involves solving, with the desired accuracy, at most nonlinear systems of equations. The boundary conditions needed by the original differential problem (2.1) translate, for the present procedure, into the correct values of entropy and mass flow rate.

We are interested in expansion from a reservoir, so that the focus is on subsonic inlet conditions. The nozzle geometry is the same used to compute the phase planes of §2.3.4, detailed in Appendix A.

### 3.1 Problem description

Equations (2.1) allow the computation of all the flow variables when  $A(x)$  is known and suitable inlet/outlet conditions are given. However, the standard nozzle problem is set up in a slightly different way. This amounts to considering the nozzle as a discharging device between a reservoir with known conditions and a stationary atmosphere with known pressure  $P_a$ . For given reservoir conditions, the aim is to study the behavior of the flow variables inside of the nozzle and their dependence on the discharge or ambient pressure. The boundary condition we take into account is the ambient to reservoir pressure ratio,

$$\beta = \frac{P_a}{P_{\text{res}}}. \quad (3.1)$$

The inlet/outlet conditions are somehow related to the reservoir and ambient conditions. The inlet will certainly be subsonic, while the outlet could be either subsonic or supersonic. The latter means that the exit conditions could be

different from the ambient values. That is, the ambient pressure  $P_a$  is not to be confused with the actual exit pressure,  $P_e$ , whose value depends on the outflow condition (subsonic/supersonic). In this respect, when  $P_a \neq P_e$  an over-expanded or under-expanded jet develops outside of the nozzle.

We conclude this section with a brief discussion on *choking* conditions. When the mass flow rate equals its maximum value the flow is said to be choked. In such a condition, decreasing the ambient to reservoir pressure ratio has no influence on the mass flow rate value. For a choked flow the throat is required to be sonic,  $M_t = 1$ . However, we will see that the opposite is not always true, i.e. a sonic throat does not necessarily imply the mass flow rate is the maximum dischargeable.

### 3.2 Limiting and intermediate solutions

The term 'solution' refers to a set of variables which describes the complete thermodynamic and kinematic state along the nozzle. For instance, such a set includes the density, the pressure and the Mach number. Consider the reservoir conditions fixed. A monotonic decrease in the exhaust pressure produces a specific sequence of solutions. Solutions exhibiting a different qualitative structure are expected. For instance, recalling standard nozzle flows of polytropic ideal gases, two possible solution types are: those completely subsonic, with no shocks inside of the nozzle and those supersonic in the divergent portion up to the occurrence of a shock wave.

To describe the complex picture of nozzle flows of non-ideal compressible fluids, it is useful to introduce the concept of *limiting* and *intermediate* solutions. Two solutions are said to be equivalent if they are qualitatively similar, i.e. they share branches of the same type (sub/supersonic), the same type of sonic points (minimum/maximum of the related flux functions), the same number and the same type of shocks (compression/rarefaction, sonic/non-sonic). That is, the equivalence is to be understood in a topological sense. According to the boundary conditions, sets of equivalent solutions can be defined as those including solutions sharing the same qualitative structure. A solution is *intermediate* if it is part of a set of equivalent solutions. The *limiting* solutions represent the boundary between two different sets of equivalent solutions, i.e. they separate two distinct types of intermediate solutions. The pattern of the limiting solutions defines the possible isentropic and non-isentropic flow occurring in the nozzle and the qualitative behavior of the variables through the nozzle, i.e the operating or *functioning regime*. In the following we refer to a functioning regime with the symbol ' $\mathcal{R}$ '.

Given the type of boundary condition we consider, in relation to the limiting solutions a set of limiting values of the ambient to reservoir pressure ratio  $\beta_{\text{limit}}$  is defined. Then, for given reservoir conditions, an intermediate solution is observed whenever the ambient to reservoir pressure ratio lies between two consecutive limiting values.

### 3.3 The computation procedure

This section shows how the tools introduced in the previous chapter can be used to compute limiting and intermediate solutions. For simplicity we perform the computation for a LMC fluid first, producing the same qualitative solutions of polytropic ideal gases.

Under certain conditions detailed in §2.3.3, the mass flow rate equation provides an implicit definition of the density evolution along the nozzle, in an isentropic flow. The equation is recalled here, highlighting also the dependence on the total enthalpy, the entropy and the mass flow rate, that leads to

$$f(\rho; s, h^t)A(x) - \dot{m} = 0. \quad (3.2)$$

The total enthalpy is constant along isentropic branches and across any shock discontinuity; it is therefore equal to the reservoir value. Information about the entropy and the mass flow rate, as well as about the presence of shocks, is obtained from the boundary condition. Once the density and entropy evolution along the nozzle is known, all the other variables can be computed.

#### 3.3.1 Computation of limiting solutions

We defined a limiting solution according to the effect resulting from a small perturbation of the boundary condition: this causes the perturbed solution to be qualitatively different from the reference one. Unfortunately such a definition does not provide a practical method to compute this kind of solutions. Nevertheless the analysis of §2 provides very useful information for the task, especially the phase plane analysis. The phase plane offers an overview of the possible solution, so that it is possible to detect some particular solution with the sought features. We recall that the phase plane represents isentropic flows only. Then, in a general flow with shocks, we should associate a phase plane portion to each of the isentropic branches. Relation (2.26) imposes the direction in which the isentropic pattern could change from an isentropic portion to the following one.

The case of a LMC fluid is used as an example, since it is qualitatively similar to the well-known case of a polytropic ideal gas. As stated in §2.3.5, LMC fluids can only exhibit the  $\mathcal{S}_{\mathcal{I}}$  isentropic pattern. This is characterized by a monotone decreasing  $M-\rho$  relation, which leads necessarily to the presence of one sonic point only. Therefore the occurrence of any shocks inevitably produces no change in the isentropic pattern. The resulting, 'ideal', operating regime is referred to as  $\mathcal{R}_{\mathcal{I}}$ . Let us consider the phase plane for isentropic pattern  $\mathcal{S}_{\mathcal{I}}$ , see Fig. 2.7. Focusing on subsonic inlet conditions, we see that an isentropic flow, from inlet to outlet, can be attained only if the exit pressure is higher than the exit value of the subsonic branch of curve  $b$ , or if it is exactly equal to the exit value of the supersonic branch of curve  $b$ . When the ambient pressure falls between these two values we expect to see something that the phase plane alone cannot represent. One situation is the presence of a shock in the divergent portion of the nozzle. The other occurrence is the presence of an over- or under-expanded jet outside of the nozzle. Since LMC fluids exhibit  $\mathcal{S}_{\mathcal{I}}$  pattern only,

the isentropic pattern downstream of the discontinuity would be  $\mathcal{S}_{\mathcal{I}}$  as well, so that we could expect nothing but an isentropic compression down to the exhaust section. The transition between a completely isentropic flow to a shocked one is an example of limiting conditions. With reference to nozzle flows of ideal gases, it is known that decreasing the ambient pressure the shock moves downstream, until it reaches the exhaust section. A further decrease will cause the presence of an over-expanded jet outside of the nozzle. This occurrence is another example of limiting conditions.

With this reasoning it is possible to detect all the limiting solutions. Figure 3.1 shows the density, pressure and Mach number limiting solutions computed from the van der Waals model with  $c_v/R = 3$ . They are detailed as follows:

$$\mathcal{R}_{\mathcal{I}}^{[0]} : \beta = 1$$

Not displayed, there is no flow through the nozzle. The variables equal their reservoir values.

$$\mathcal{R}_{\mathcal{I}}^{[1]} : \beta = \beta_1$$

The flow is subsonic over the entire nozzle except the throat, which is sonic. The solution coincides with the portion of level set  $b$  in Fig. 2.7, representing subsonic flow with sonic throat. A slight increase in the ambient pressure results in a subsonic throat, whereas a decrease causes a shocked flow. The nozzle is choked,  $\dot{m} = \dot{m}_{\max} = \dot{m}_c(s_{\text{res}}, h^t)$ , with  $\dot{m}_c$  as defined in §2.3.4. The density evolution along the nozzle is computed through Eq. (3.2), given that the entropy, total enthalpy and mass flow rate values are all available. The exit density  $\rho_1$  is the subsonic root of equation

$$f(\rho; s_{\text{res}}, h^t) = \dot{m}_{\max}/A_e, \quad (3.3)$$

and consequently

$$\beta_1 = P(s_{\text{res}}, \rho_1)/P_{\text{res}}.$$

Every pressure ratio lower than  $\beta_1$  results in a choked flow.

$$\mathcal{R}_{\mathcal{I}}^{[2]} : \beta = \beta_2$$

The flow is subsonic in the convergent part of the nozzle, sonic at throat and supersonic all over the divergent portion. A shock occurs at the exit section of the nozzle. Except at the exit section, the solution coincides with the portion of level set  $b$  in Fig. 2.7, which represents subsonic-sonic-supersonic flow. A slight increase of the ambient pressure causes a shock to occur in the divergent portion, whereas a decrease results in an isentropic flow inside of the nozzle and an over-expanded jet outside of it. The entropy value upstream of the shock is simply  $s_{\text{res}}$ , the upstream density is given by the supersonic root of (3.3) and the upstream Mach number is computed from Eq. (2.4). The entire upstream state is known so that

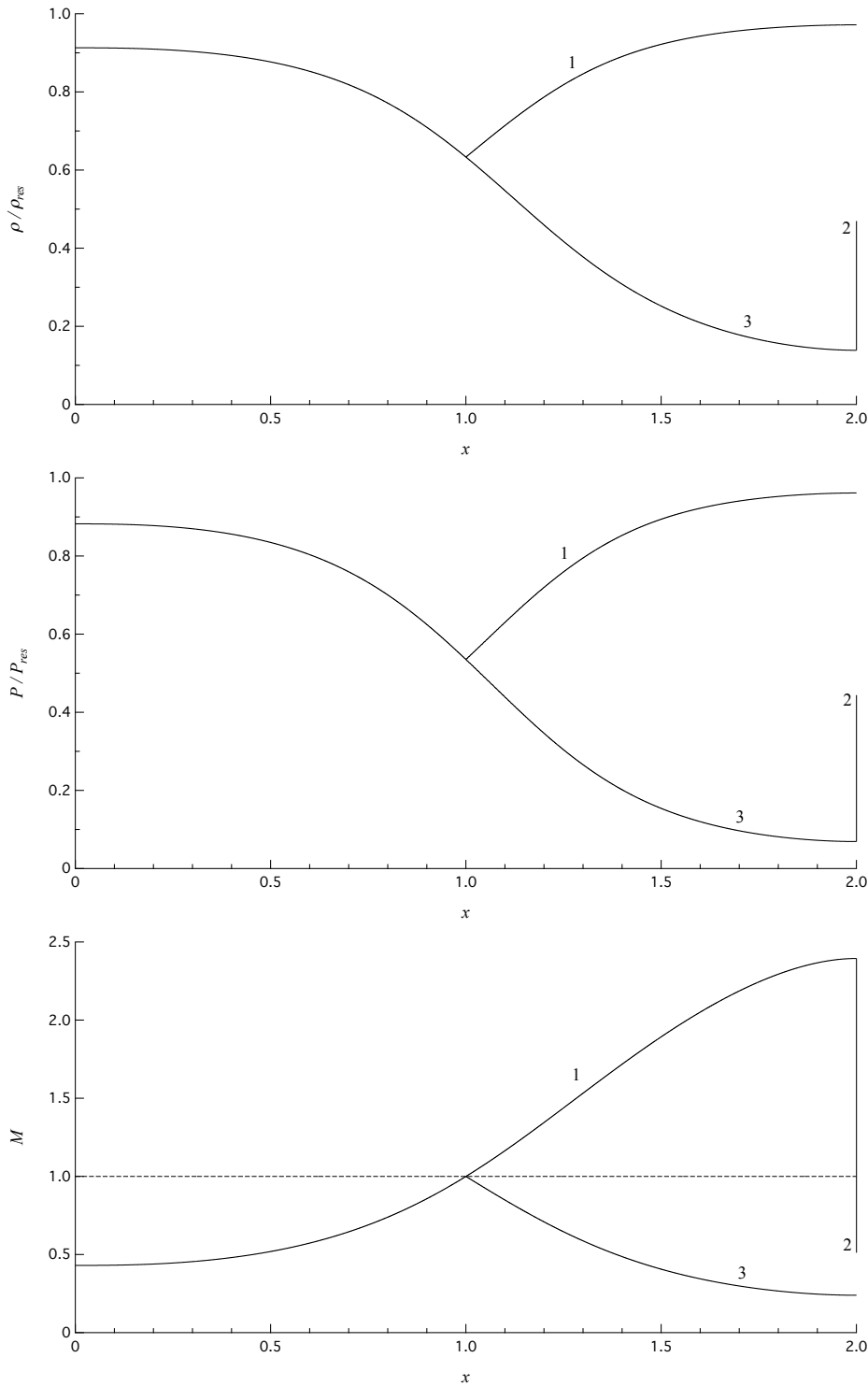


Figure 3.1: Density, pressure and Mach number limiting solutions for  $\mathcal{R}_I$  functioning regime. Solutions computed from the polytropic van der Waals model with  $\delta = 1/3$ , corresponding to a LMC fluid. Reservoir conditions:  $v_{\text{res}} = 10v_c$ ,  $P_{\text{res}} = 10P_c$ .

the downstream state is obtained from system (2.14) and quantity  $\beta_2$  is easily computed.

$$\mathcal{R}_{\mathcal{T}}^{[3]} : \beta = \beta_3$$

A completely isentropic expansion is attained and the nozzle is said to be adapted. The solution equals the previous one except for the shock occurring at the exhaust section. A slight change of the ambient pressure doesn't modify the solution inside of the nozzle, however it causes the presence of an over-expanded or under-expanded jet outside of the nozzle.

The procedure allows as to define a set of limiting ambient to reservoir pressure ratios

$$(1, \beta_1, \beta_2, \beta_3, 0),$$

such that, for any two ambient to reservoir pressure ratios included between two consecutive limiting values, two equivalent solutions are observed. Moreover the limiting solution layout provides very important information to be used in the computation of intermediate solutions.

### 3.3.2 Computation of intermediate solutions

In the computation of intermediate solutions the actual value of the boundary condition is to be taken into account. The process is simplified thanks to the information available from the computation of limiting solutions. Figure 3.2 shows examples of intermediate solutions, described as follows:

$$\mathcal{R}_{\mathcal{T}}^{[0-1]} : \beta_1 < \beta < 1$$

The flow is completely subsonic and the nozzle is not choked. Given that no shock occurs in a subsonic flow, the solution is also isentropic. The exit pressure is equal to the imposed ambient value,  $P_e = P_a > P_1$ , and the exit density is computed from

$$\rho_e = \rho(s_{\text{res}}, P_e).$$

Then the mass flow rate is simply

$$\dot{m} = f(\rho_e, s_{\text{res}}, h^t)A_e.$$

The usual procedure, through Eq. (3.2), applies for the computation of the density evolution.

$$\mathcal{R}_{\mathcal{T}}^{[1-2]} : \beta_2 < \beta < \beta_1$$

The nozzle is choked, exhibiting a supersonic divergent up to the occurrence of a shock. That is, the solution equals  $\mathcal{R}_{\mathcal{T}}^{[3]}$  up to the discontinuity. Downstream of the latter an isentropic compression takes place up to exhaust section. Being the outflow subsonic the exit pressure equals the

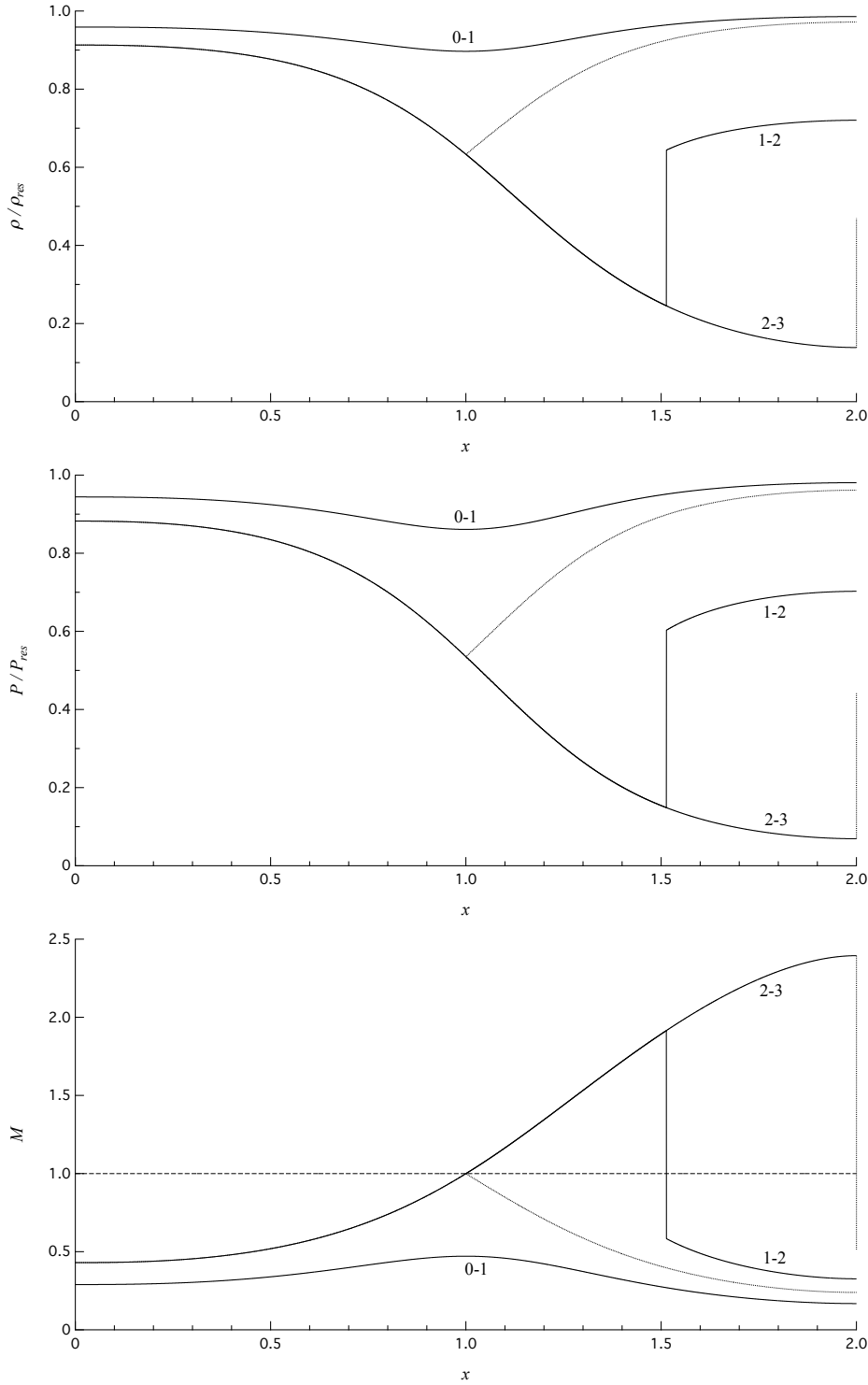


Figure 3.2: Density, pressure and Mach number intermediate solutions (continuous line) and limiting solutions (dotted line) for  $\mathcal{R}_I$  functioning regime. Solutions computed from the polytropic van der Waals model with  $\delta = 1/3$ , corresponding to a LMC fluid. Reservoir conditions:  $v_{\text{res}} = 10v_c$ ,  $P_{\text{res}} = 10P_c$ .

ambient value also in this case. The mass flow rate is known,  $\dot{m} = \dot{m}_{\max}$ , so that the exit density  $\rho_e$  is the root of the following equation:

$$f(\rho; s(P_e, \rho), h^t) - \dot{m}/A_e = 0, \quad (3.4)$$

where  $P_e$  is the imposed exit pressure. This equation has a unique solution, given the following relation for the monotonicity of the flux function, with respect to density, for fixed pressure and total enthalpy:

$$\left( \frac{\partial f}{\partial \rho} \right)_{P, h^t} = u - \frac{\rho}{u} \left( \frac{\partial h}{\partial \rho} \right)_P = u + \frac{c^2}{Gu} > 0.$$

The exit entropy, which is also the constant entropy value downstream of the shock is simply

$$s_e = s(P_e, \rho_e).$$

Therefore, given the known quantities,  $s_l = s_{\text{res}}$ ,  $s_r = s_e$  and  $h^t$ , with subscripts  $l$  and  $r$  denoting quantities upstream and downstream of the shock, the following system,

$$\begin{cases} \rho_r M_r c(s_r, \rho_r) = \rho_l M_l c(s_l, \rho_l) \\ P(s_r, \rho_r) + \rho_r M_r^2 c^2(s_r, \rho_r) = P(s_l, \rho_l) + \rho_l M_l^2 c^2(s_l, \rho_l) \\ h(s_r, \rho_r) + \frac{1}{2} M_r^2 c^2(s_r, \rho_r) = h^t \\ h(s_l, \rho_l) + \frac{1}{2} M_l^2 c^2(s_l, \rho_l) = h^t, \end{cases} \quad (3.5)$$

is to be solved for the unknown vector

$$(\rho_l, \rho_r, M_l, M_r).$$

The numerical method used to approximate the relevant root of nonlinear systems for shock waves is detailed in Appendix C. Once the system is solved the shock position  $x_s$  is given by:

$$f(\rho_l; s_l, h^t) A(x_s) - \dot{m} = 0, \quad (3.6)$$

in which we obviously search for the root in the divergent part of the nozzle. Now the portions upstream and downstream of the shock can be treated separately. It is interesting to observe the phase plane variation across the shock, Fig. 3.3. Due to the entropy rise, across a shock discontinuity the stagnation conditions, as well as the phase plane, change. Recalling Eq. (2.25), stagnation density decreases from  $\rho_{0,l} = \rho(s_l, h^t)$  to  $\rho_{0,r} = \rho(s_r, h^t)$ . Moreover the post-shock flux function is all confined below the pre-shock one,

$$f(\rho, s_r, h^t) < f(\rho, s_l, h^t), \quad 0 \leq \rho \leq \rho_{0,r} \quad (3.7)$$

given that  $h(s_r, \rho) \geq h(s_l, \rho)$ , thanks to  $(\partial h / \partial s)_v = T(1 + G) > 0$ . It follows therefore that  $\dot{m}_c(s_r, h^t) < \dot{m}_c(s_l, h^t)$ . Since the nozzle is choked with  $\dot{m} = \dot{m}_c(s_l, h^t)$ , the contour branch of the density solution after the shock occurrence is similar to case labeled  $c$  in Fig. 2.7.

$$\mathcal{R}_{\mathcal{I}}^{[2-3]} : \beta_3 < \beta < \beta_2$$

For any  $\beta_3 < \beta < \beta_2$  the solution is equal to limiting case  $\mathcal{R}_{\mathcal{I}}^{[3]}$  all over the nozzle. The outflow is supersonic and the exit pressure is lower than the ambient value, causing an over-expanded jet outside of the nozzle.

Finally, when  $\beta < \beta_3$ , the solution is again equal to  $\mathcal{R}_{\mathcal{I}}^{[3]}$  over the entire nozzle and an under-expanded jet lies outside of the nozzle.

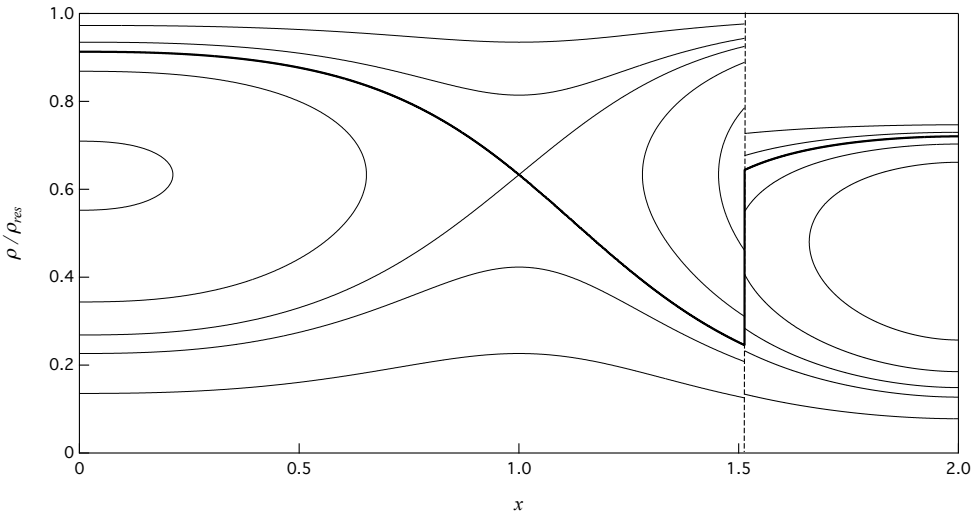


Figure 3.3: Phase plane for the two isentropic portions of intermediate solution  $\mathcal{R}_{\mathcal{I}}^{[1-2]}$ .

### 3.4 Exact solutions for HMC fluids

This section deals with the features of nozzle flows of HMC fluids. This class of fluids can exhibit isentropic patterns  $\mathcal{S}_{\mathcal{I}}$  and  $\mathcal{S}_{\mathcal{M}^+}$ . In §2.4.3 we have claimed that ordering relation (2.26) could be extended to fluids exhibiting different values of dimensionless specific heat. We report indeed that a similar relation holds for the HMC fluid (polytropic van der Waals model with  $c_v/R = 15$ ) selected here for the computation. In the present case the relation clearly involves only  $\mathcal{S}_{\mathcal{I}}$  and  $\mathcal{S}_{\mathcal{M}^+}$  patterns and, as in (2.26), it reveals that an entropy rise may cause  $\mathcal{S}_{\mathcal{M}^+} \rightarrow \mathcal{S}_{\mathcal{I}}$  transition. Conversely, the opposite is not allowed.

If the reservoir conditions exhibit the  $\mathcal{S}_{\mathcal{I}}$  pattern we expect the situation to resemble that of LMC fluids. Thanks to the ordering relation just discussed, no transition is possible from  $\mathcal{S}_{\mathcal{I}}$  to  $\mathcal{S}_{\mathcal{M}^+}$ .

We concentrate now on stagnation conditions exhibiting  $\mathcal{S}_{\mathcal{M}^+}$  pattern. The phase planes and flux functions are qualitatively the same as for  $\mathcal{S}_{\mathcal{I}}$ , leading to density and pressure solutions which are qualitatively the same. The only difference is represented by the Mach number, which exhibits a supersonic non-monotone region. Therefore only the Mach number solutions along the nozzle are presented here. The resulting functioning regime will be referred to as  $\mathcal{R}_{\mathcal{M}^+}$ .

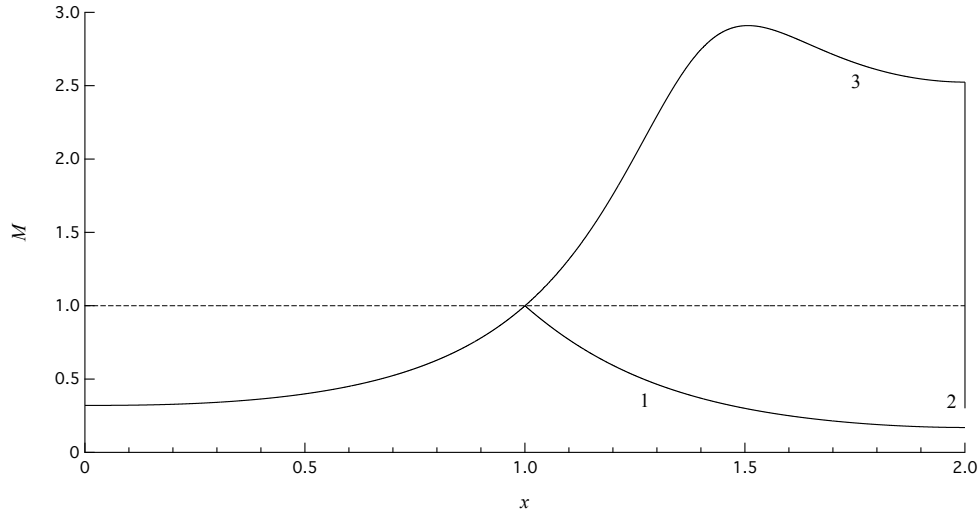


Figure 3.4: Mach number limiting solutions for  $\mathcal{R}_{\mathcal{M}^+}$  functioning regime. Solutions computed from the polytropic van der Waals model with  $\delta = 1/15$ , corresponding to a HMC fluid. Reservoir conditions:  $v_{\text{res}} = 0.50v_c$ ,  $P_{\text{res}} = 6.61P_c$ .

Figures 3.4 and 3.5 show the limiting and intermediate solutions for the Mach number. Among the limiting solutions only those which exhibit a supersonic portion will be affected by non-monotonicity, i.e.  $\mathcal{R}_{\mathcal{M}^+}^{[2]}$  and  $\mathcal{R}_{\mathcal{M}^+}^{[3]}$ , being the subsonic behavior the same of LMC fluids. Intermediate solution  $\mathcal{R}_{\mathcal{M}^+}^{[1-2]}$  presents a shock which could be located anywhere in divergent, depending on the ambient to reservoir pressure ratio. Hence the present solution shows a non-monotone portion depending on the shock position. After the shock occurs the flow is necessarily subsonic, implying strictly monotone decreasing Mach number evolution. The entropy rise across a shock could determine a change in the isentropic profile, which is  $\mathcal{S}_{\mathcal{M}^+}$  upstream and may be  $\mathcal{S}_{\mathcal{M}^+}$  or  $\mathcal{S}_{\mathcal{I}}$  downstream. Since the two exhibit no qualitative differences in the subsonic behavior, the exact solution in both cases is qualitatively the same.

### 3.4.1 Remark on functioning regimes

It has to be noted that, with reference to Figs. 3.4 and 3.5, if the nozzle is not long enough or the stagnation condition conveniently modified, the non-monotone Mach number behavior would not be observed. Recalling §2.3.2, the non-monotone region is confined within a limited density interval, which is related to stagnation conditions. Whether the actual expansion extends to this region is dependent both on stagnation conditions and on the nozzle geometry. If expansion to arbitrarily large Mach number values is assumed, for instance through a continuous increase in the cross-sectional area, then stagnation conditions exhibiting  $\mathcal{S}_{\mathcal{M}^+}$  pattern would certainly result in  $\mathcal{R}_{\mathcal{M}^+}$  functioning regime.

We are indeed interested in describing nozzle flows including non-ideal phenomena. In this respect, an unfavorable geometry of the divergent portion of the nozzle could prevent us from reaching the density values where these phenomena

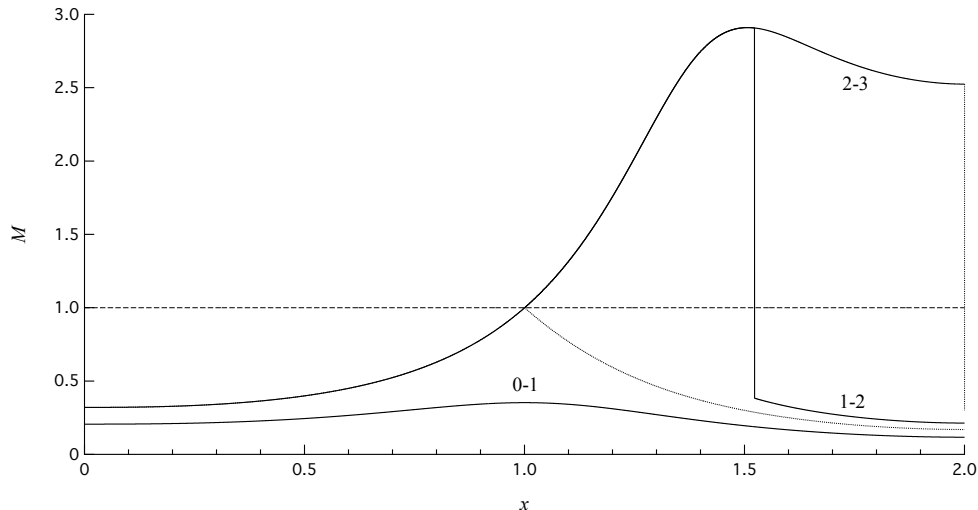


Figure 3.5: Mach number intermediate solutions (continuous line) and limiting solutions (dotted line) for  $\mathcal{R}_{\mathcal{M}^+}$  functioning regime. Solutions computed from the polytropic van der Waals model with  $\delta = 1/15$ , corresponding to a HMC fluid. Reservoir conditions:  $v_{\text{res}} = 0.5048v_c$ ,  $P_{\text{res}} = 6.6134P_c$ .

take place.

Recalling §2.3.2, the idea was to consider the Mach number dependence on density in relation to an expansion to arbitrarily large Mach numbers. In this way the whole non-classical features could be analyzed. Given that the exact solutions layout always include a solution representing a complete expansion, for instance  $\mathcal{R}_{\mathcal{I}}^{[3]}$  or  $\mathcal{R}_{\mathcal{M}^+}^{[3]}$ , we could consider functioning regimes in relation to expansions to arbitrarily large Mach numbers. With such a definition, the exact solutions layout is forced to include all the possible non-ideal phenomena. Moreover, the functioning regime would not depend on the nozzle geometry, except for the assumed convergent-divergent shape. As a matter of fact, the functioning regime are defined by the reservoir conditions.

However, it is not possible to select, a priori, a suitable nozzle geometry allowing for such a complete expansion, i.e. involving the whole non-ideal features, for any couple of reservoir conditions. Nevertheless, we have verified that the current nozzle geometry is appropriate for the task and for future explanation reservoir conditions will be chosen so that all of the non-ideal effects can occur within the current nozzle.

To summarize, two functioning regimes are observable for HMC fluids:  $\mathcal{R}_{\mathcal{I}}$ , which is the same regime performed by LMC fluids;  $\mathcal{R}_{\mathcal{M}^+}$ , which differs from the former in the supersonic portions of the limiting solutions. With the previous assumption on the expansion,  $\mathcal{S}_{\mathcal{I}}$  reservoir conditions lead to  $\mathcal{R}_{\mathcal{I}}$  functioning regime, whereas  $\mathcal{S}_{\mathcal{M}^+}$  reservoir states lead to  $\mathcal{R}_{\mathcal{M}^+}$ .

### 3.5 Exact solutions for BZT fluids

Nozzle flows of BZT fluids exhibit the most interesting behavior due to the presence of multiple sonic points along isentropic expansions. The related phase planes, under certain conditions, show the impossibility of a complete isentropic expansion from rest to arbitrarily large Mach numbers. These and other difficulties related to the non-classical features of BZT fluid flows are first discussed in §3.5.1. The functioning regimes for nozzle flows of BZT fluids are then introduced and detailed.

#### 3.5.1 Preliminary remarks

The computation of limiting solutions for LMC fluids is a straightforward task, being their behavior very similar to polytropic ideal gases. For HMC fluids some limiting solutions are slightly different, due to the non-monotone Mach number evolution, but this can be regarded as a minor modification to the nozzle solutions for LMC fluids. The reason why these regimes are simple to treat is that the related isentropic patterns exhibit one sonic point only. The limiting solutions are also isentropic (except  $\mathcal{R}_{\mathcal{I}}^{[2]}$  and  $\mathcal{R}_{\mathcal{M}^+}^{[2]}$ , at the exhaust section) and they can be detected from the phase plane related to the reservoir conditions.

The situation is different if the isentropic pattern of reservoir conditions shows three sonic points, as it is possibly the case for BZT fluids. As we discussed in §2.3.4, some contours, going from inlet to outlet, show a sonic point upstream or downstream of the throat. The contour line in this case becomes vertical and reverts, so that the flow cannot be continued isentropically. A sonic shock is indeed required to continue the expansion. Therefore we have to deal with limiting solutions containing more than one isentropic branch. To explain such a situation, Fig. 3.6 anticipates a limiting solution having these features.

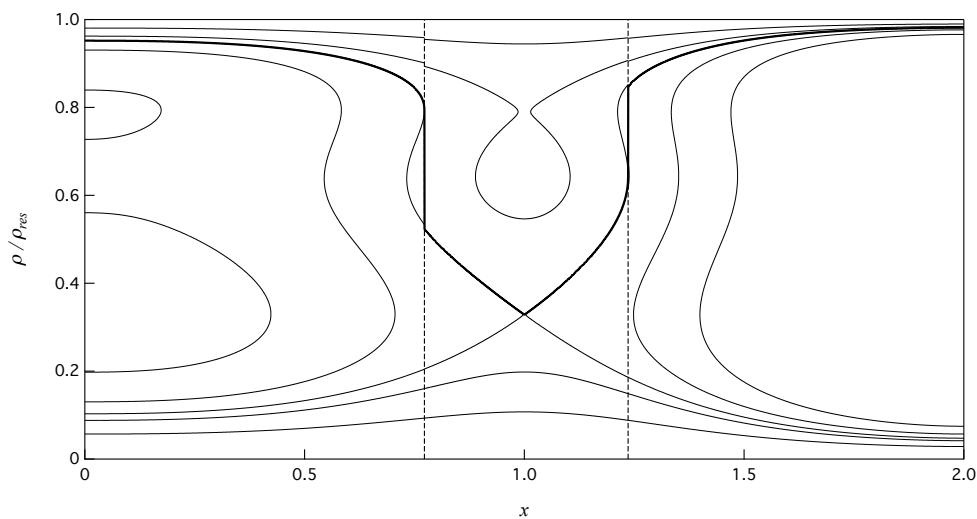


Figure 3.6: Example of limiting solution containing multiple shocks (bold line), together with portions of phase planes relative to the different isentropic branches.

The solution contains two sonic shocks, a pre-sonic rarefaction and a pre-sonic compression shock. Due to the entropy rise, across a shock discontinuity the stagnation conditions, as well as the phase plane, change. The figure represents the portions of the phase planes involved. Reservoir condition exhibit  $S_{N^-}$ -isentropic pattern. It is also easy to see that the three isentropic portions show three sonic points each, due to the fact that no shock-induced transition of isentropic pattern occurs. The occurrence of such a transition is another difficulty we have to deal with in the following.

Significant changes are expected if the isentropic pattern switches from one with three sonic points to another with a different number of sonic points. The situation is depicted in Fig. 3.7. The reservoir conditions show again  $S_{N^-}$ -pattern. Here the second shock determines a transition from  $S_{N^-}$  to  $S_{N^-}/S_{M^-}$ . The latter exhibit two sonic points, one of which is a stationary inflection point of the related flux function. As we can see in the solution, this results in the presence of a point with infinite slope, without causing any shocks. Indeed, in this case the underlying contour line doesn't revert and the flow can be continued isentropically. A slight increase of the exhaust pressure results in no isentropic pattern transition, across the second shock. A decrease of the exhaust pressure causes instead a shock-induced transition from  $S_{N^-}$  to  $S_{M^-}$ . This explains why this solution is a limiting one.

The two examples have shown that detecting limiting solutions is a more difficult task for BZT fluids, compared to LMCs or HMCs. Two observations could be useful in this respect. First, the transition between different isentropic patterns could determine a limiting situation. Moreover, the presence of a sonic shock could be another limiting condition. A sonic shock is indeed the limiting case of a generic shock. Even this is not always the case, we will see that limiting solutions often contain this kind of discontinuities.

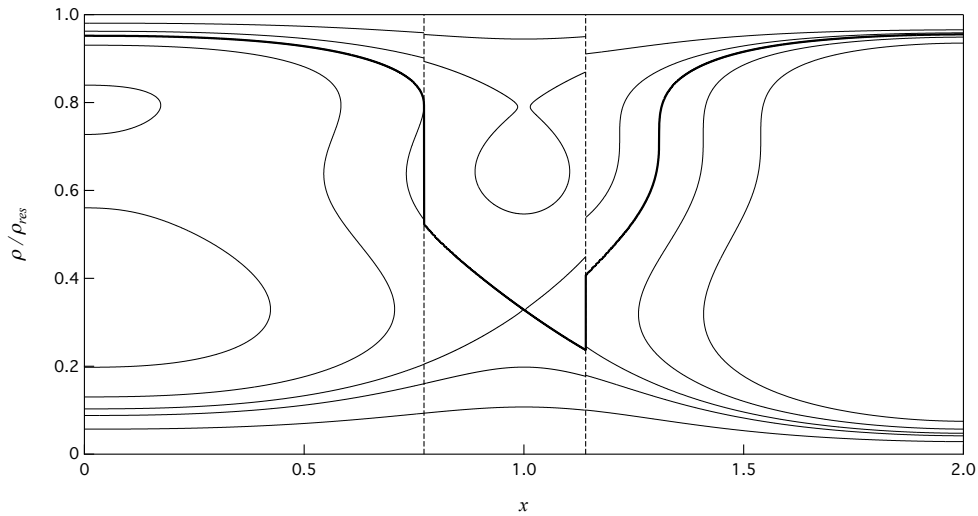


Figure 3.7: Example of limiting solution containing multiple shocks (bold line), together with portions of phase planes relative to the different isentropic branches. The second shock also determines an isentropic pattern transition.

The discussion reported in §2.4.2 can be of help in defining the possible sonic shocks that could take place in any specific circumstances. In §2.3.4 the multiple sonic points exhibited by certain isentropic pattern have been ordered as (2.13). In view of the presence of different isentropic branches in certain solutions, it is convenient to make the dependence of the sonic density values on entropy and total enthalpy explicit. However, the total enthalpy is uniform over the entire nozzle and therefore it is sufficient to specify only the entropy value. For instance, considering an isentropic pattern, with entropy value  $\bar{s}$  and exhibiting three sonic points,  $\rho_{s_1}(\bar{s})$  indicates the largest of the sonic densities.

### 3.5.2 Functioning regimes for BZT fluids

We consider a fluid described by the polytropic van der Waals model with  $c_v/R = 50$  and a set of reservoir conditions which starts from  $S_I$  isentropic pattern up to  $S_{M+}$ . That is, with reference to ordering relation (2.26), the description begins with the isentropic pattern exhibiting no possible transitions, up to that which allows all possible transitions. Transitions between different isentropic pattern indeed play a central role for BZT fluids. We immediately point out that this way of presenting has the purpose of gradually increasing the complexity of the flow description. It is not related to an equivalence between the isentropic pattern of reservoir conditions and the functioning regimes. Actually, for certain functioning regimes the latter claim it true, but it is not always the case. We leave for a subsequent section a precise definition of reservoir conditions leading to each functioning regime.

In addition to  $R_I$  and  $R_{M+}$ , six new functioning regimes are introduced:  $R_{M-}$ ,  $R_{N^{1+}}$ ,  $R_{N^{1-}}$ ,  $R_{N^{2+}}$ ,  $R_{N^{2-}}$ ,  $R_{N^3}$ . The description of  $R_I$  is omitted since it shows the same features previously described for LMC fluids.

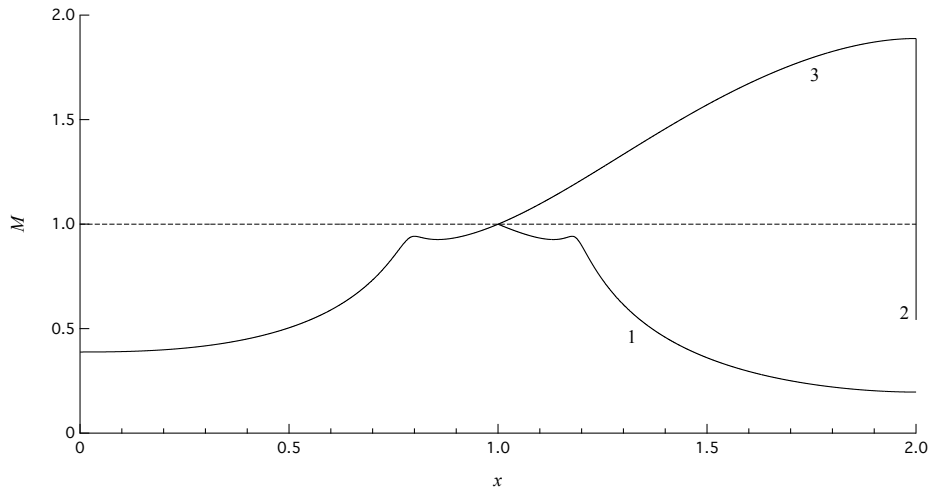


Figure 3.8: Mach number limiting solutions for  $R_{M-}$  functioning regime. Solutions computed from the polytropic van der Waals model with  $\delta = 1/50$ , corresponding to a BZT fluid. Reservoir conditions:  $v_{\text{res}} = 0.8087v_c$ ,  $P_{\text{res}} = 1.2148P_c$ .

### Functioning regime $\mathcal{R}_{\mathcal{M}-}$

Functioning regime  $\mathcal{R}_{\mathcal{M}-}$  results from reservoir conditions exhibiting  $\mathcal{S}_{\mathcal{M}-}$  isentropic pattern. The latter is characterized by the presence of one sonic point and of a non-monotone Mach number region confined at subsonic values. The phase planes and flux functions are qualitatively the same as for  $\mathcal{S}_{\mathcal{I}}$  and this leads to density and pressure solutions which are qualitatively the same. The only difference is represented by the Mach number behavior, which exhibit a subsonic non-monotone region. Therefore only the Mach number solutions along the nozzle are presented. These are shown in Figs. 3.8 and 3.9. The subsonic portions of the limiting solution, or even entire  $\mathcal{R}_{\mathcal{M}-}^{[1]}$  solution, show the non-monotone region, near the sonic point. In Fig. 3.9 two intermediate solutions  $\mathcal{R}_{\mathcal{M}-}^{[1-2]}$  are plotted, namely  $\mathcal{R}_{\mathcal{M}-}^{[1-2']}$  and  $\mathcal{R}_{\mathcal{M}-}^{[1-2'']}$ . The former exhibits a  $\mathcal{S}_{\mathcal{M}-}$  post-shock isentropic pattern. A non-monotone region develops after the shock, where the Mach number is close to unity. Conversely, in  $\mathcal{R}_{\mathcal{M}-}^{[1-2'']}$  an isentropic pattern transition, from  $\mathcal{S}_{\mathcal{M}-}$  to  $\mathcal{S}_{\mathcal{I}}$ , takes place across the shock. However, we remark that this is not always the case. It is possible as well that the shock causes an isentropic pattern transition but, being density far from the non-monotone  $M-\rho$  region, the exact solution nevertheless shows a monotone behavior.

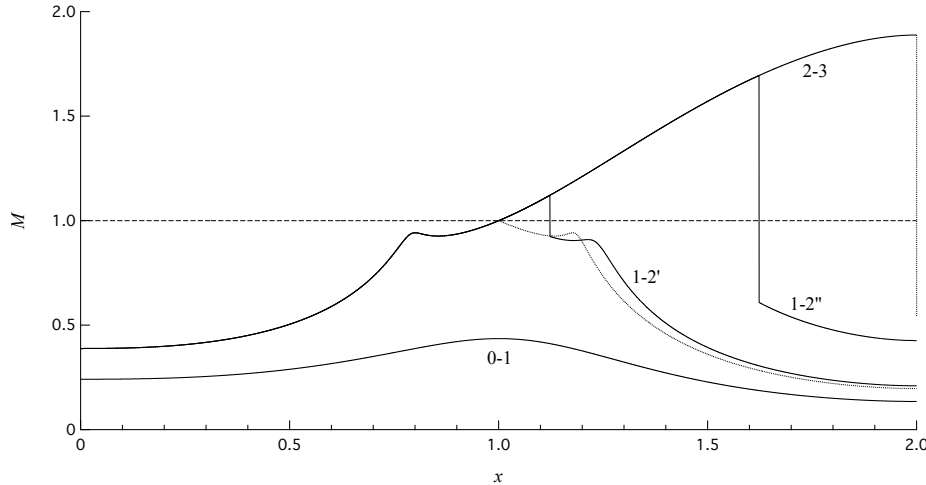


Figure 3.9: Mach number intermediate solutions (continuous line) and limiting solutions (dotted line) for  $\mathcal{R}_{\mathcal{M}-}$  functioning regime. Solutions computed from the polytropic van der Waals model with  $\delta = 1/50$ , corresponding to a BZT fluid. Reservoir conditions:  $v_{\text{res}} = 0.8087v_c$ ,  $P_{\text{res}} = 1.2148P_c$ .

### Functioning regime $\mathcal{R}_{\mathcal{N}^{2+}}$

For the description of this functioning regime we select a stagnation state exhibiting  $\mathcal{S}_{\mathcal{N}-}$  isentropic pattern. This represent a major change with respect to the previously described functioning regimes, due to the presence of three sonic points. Moreover, this leads to significant consequences regarding the chocking condition. Figure 3.10 shows the limiting solutions pattern, described as follows:

$$\mathcal{R}_{\mathcal{N}^{2+}}^{[0]} : \beta = 1$$

The exit pressure equals the reservoir value, no flow occurs.

$$\mathcal{R}_{\mathcal{N}^{2+}}^{[1]} : \beta = \beta_1$$

The flow is subsonic in the convergent portion, sonic at throat and subsonic again in the divergent. The throat density is  $\rho_t = \rho_{s_1}(s_{\text{res}})$ , which does not correspond to the global maximum of the related flux function. The mass flow rate is  $\dot{m} = f(\rho_{s_1}; s_{\text{res}}, h^t)$ .

$$\mathcal{R}_{\mathcal{N}^{2+}}^{[2]} : \beta = \beta_2$$

The mass flow rate equals that of the previous solution, given that these two solutions share the same convergent branch. The present solution includes the first example of non-classical phenomenon: the sonic compression shock. The divergent part of the nozzle is supersonic up to reaching sonic density  $\rho_{s_2}(s_{\text{res}})$ , where the flow cannot be continued isentropically. Since this sonic point coincides with a local minimum of the flux function, a slight cross section increase results in no local roots of Eq. (3.2). The occurrence of a shock is required to continue the flow towards the nozzle exit. Moreover, previous discussion identified compression shocks as those admissible from sonic point  $\rho_{s_2}(s_{\text{res}})$ , see §2.4.2. The upstream state is known and system (2.14) can be used to obtain the downstream state. Downstream of the sonic shock the flow is subsonic up to the exit section.

$$\mathcal{R}_{\mathcal{N}^{2+}}^{[3]} : \beta = \beta_3$$

The present solution shares the convergent branch with the two previous solutions, so that the mass flow rate is the same. Another non-classical phenomenon is observed: the rarefaction shock. This is a pre-sonic rarefaction shock located exactly at throat and it is computed through system (2.14). The downstream isentropic pattern is still  $\mathcal{S}_{\mathcal{N}^-}$ , so that a subsonic branch is followed up to the occurrence of a limiting pre-sonic compression shock, as that of the previous solution.

$$\mathcal{R}_{\mathcal{N}^{2+}}^{[4]} : \beta = \beta_4$$

When the ambient pressure ratio is further reduced, the mass flow rate increases. Sonic density  $\rho_{s_1}(s_{\text{res}})$  is reached upstream of the throat section and a shock is required to continue the expansion. It is remarkable that the pre-shock state is the same of the limiting rarefaction shock of the previous solution. That is, the same pre-sonic rarefaction shock of the previous solution is now observed in a different location, upstream of the throat. Therefore the entropy value at throat is different from the reservoir value,  $s_t \neq s_{\text{res}}$ .

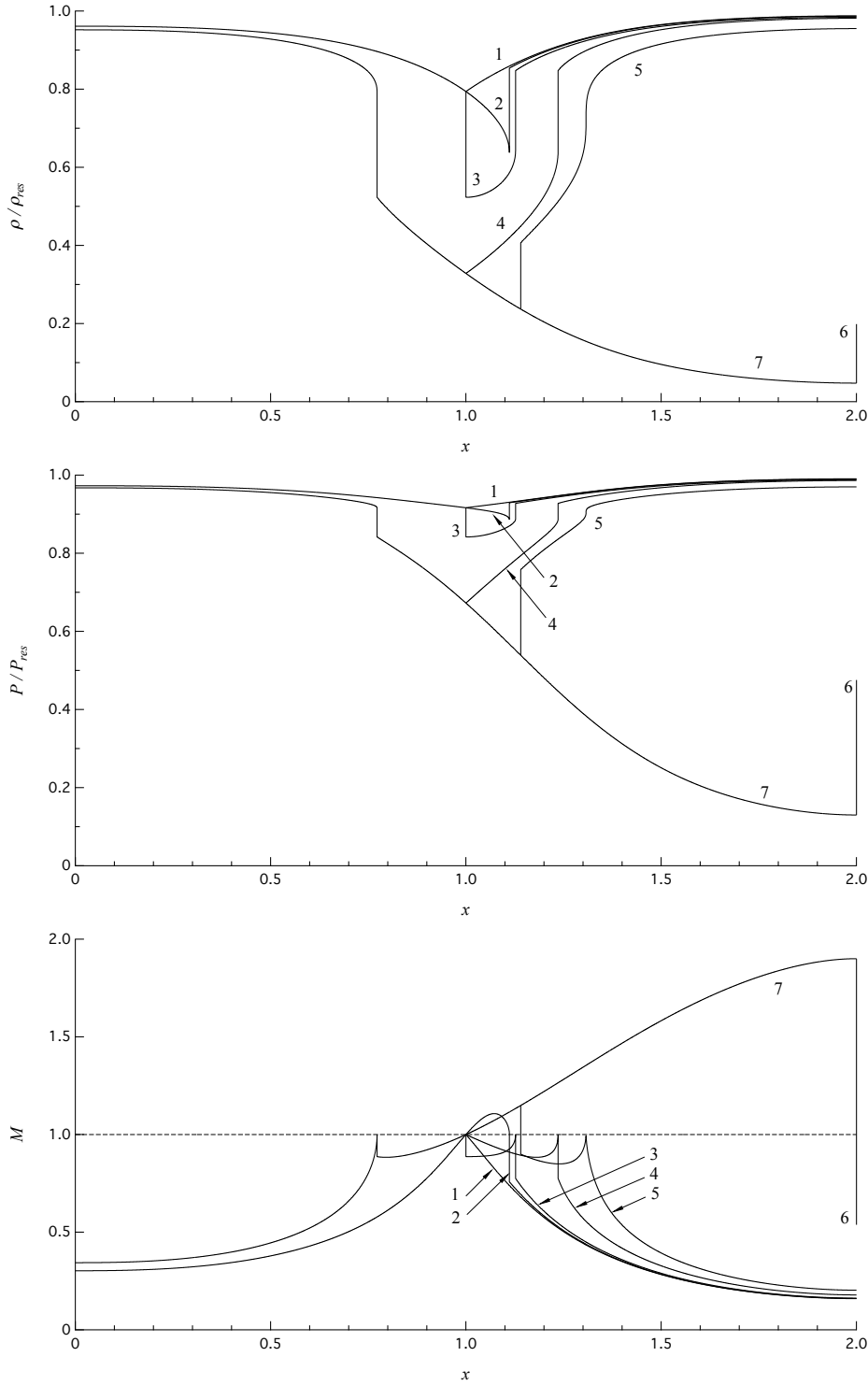


Figure 3.10: Density, pressure and Mach number limiting solutions for  $\mathcal{R}_{N^{2+}}$  functioning regime. Solutions computed from the polytropic van der Waals model with  $\delta = 1/50$ , corresponding to a BZT fluid. Reservoir conditions:  $v_{\text{res}} = 0.7818v_c$ ,  $P_{\text{res}} = 1.1168P_c$ .

The present solution exhibits the maximum mass flow rate dischargeable,

$$\dot{m} = \dot{m}_{\max} = \dot{m}_c(s_t, h^t),$$

so that the nozzle is choked. A major difference with standard nozzle flow theory is that sonic conditions at throat do not necessarily imply the mass flow rate is the maximum dischargeable. In the previous solutions  $\mathcal{R}_{\mathcal{N}^{2+}}^{[1]}$  to  $\mathcal{R}_{\mathcal{N}^{2+}}^{[3]}$ , the throat density is  $\rho_{s_1}(s_{\text{res}})$ , which however does not correspond to the global maximum of the related flux function. We have seen that, for solutions  $\mathcal{R}_{\mathcal{N}^{2+}}^{[1]}$ ,  $\mathcal{R}_{\mathcal{N}^{2+}}^{[2]}$  and  $\mathcal{R}_{\mathcal{N}^{2+}}^{[3]}$ , the mass flow rate is identical. Therefore we could talk of a 'local choking', in the sense that reducing the exhaust pressure ratio from  $\beta_1$  to  $\beta_3$  the mass flow rate does not change, even this is not the maximum dischargeable. Moreover, the presence of a shock upstream of the throat implies the throat entropy is higher than the reservoir value,  $s_t > s_{\text{res}}$ . Recalling 3.7, it follows that, for  $\mathcal{R}_{\mathcal{N}^{2+}}$  the maximum mass flow rate is

$$\dot{m}_{\max} = \dot{m}_c(s_t, h^t) < \dot{m}_c(s_{\text{res}}, h^t).$$

Downstream of the forementioned shock, the isentropic pattern is still  $\mathcal{S}_{\mathcal{N}-}$ , so that in the divergent portion of the nozzle a compressive branch is followed up to reaching sonic density  $\rho_{s_2}(s_t)$ . A pre-sonic compression shock is required to continue the flow. The current shock has the same features of the pre-sonic compression shock of solution  $\mathcal{R}_{\mathcal{N}^{2+}}^{[3]}$ , i.e. they share both the pre-shock and post-shock states. To summarize: the present limiting solution defines the choking condition and exhibits the same shocks of limiting solution  $\mathcal{R}_{\mathcal{N}^{2+}}^{[3]}$ , placed in different locations.

$$\mathcal{R}_{\mathcal{N}^{2+}}^{[5]} : \beta = \beta_5$$

For  $\beta < \beta_4$  the solution equals the previous one up to the throat section. In this case, in the divergent, the flow continues the expansion. The present limiting solution shows, in the divergent section, a peculiar shock for which the post-shock isentropic pattern precisely coincides with transition  $\mathcal{S}_{\mathcal{N}-}/\mathcal{S}_{\mathcal{M}-}$ . Pressure ratios slightly higher than  $\beta_4$  cause a  $\mathcal{S}_{\mathcal{N}-}$  pattern downstream of the shock. Conversely, pressure ratios slightly lower than  $\beta_4$  cause a transition to  $\mathcal{S}_{\mathcal{M}-}$  pattern. We will see later, in the computation of intermediate solutions, that these two conditions respectively result in a shock-splitting or simple shock configuration. Focusing on the current limiting shock, exhibiting isentropic pattern  $\mathcal{S}_{\mathcal{N}-}/\mathcal{S}_{\mathcal{M}-}$  downstream of it, the post-shock entropy is given by the following system:

$$\begin{cases} J(\rho, s; h^t) &= 0 \\ M(\rho, s; h^t) &= 1. \end{cases} \quad (3.8)$$

As usual the total enthalpy is fixed and equal to the reservoir value. This system has two roots, one which identifies transition  $\mathcal{S}_{\mathcal{M}+}/\mathcal{S}_{\mathcal{N}+}$  and one

for transition  $S_{N-}/S_{M-}$ . The former occurs for entropy values lower than  $s_{\text{res}}$ , whereas the latter for larger values. Then, imposition of the entropy condition simply provides the root we are interested in. The complete upstream and downstream states are computed from system (3.5), and consequently the shock location is obtained.

The present solution is one of the examples mentioned in the preliminary remarks §3.4.1, in which the presence of the infinite slope point in the final isentropic has also been discussed. The infinite slope point corresponds to a sonic point with null fundamental derivative. This claim that a similar point can exist in an isentropic flow can be verified also by a complementary argument. Consider the shock adiabat through that point, Fig. 3.11. The Rayleigh line corresponding to a pre-sonic shock intersects the shock adiabat in the pre-shock state and in a point located at lower density. The latter intersection represents a non-admissible shock, recall §2.4.1. Therefore the only admissible shock is the zero-intensity one, i.e. the flow can be continued isentropically through the forementioned infinite slope point.

$$\mathcal{R}_{N^2+}^{[6]} : \beta = \beta_6$$

The solution represents a complete expansion up to a compression shock which occurs at the exhaust section of the nozzle. This is treated exactly as the exit shock of case  $\mathcal{R}_{\mathcal{I}}^{[2]}$ .

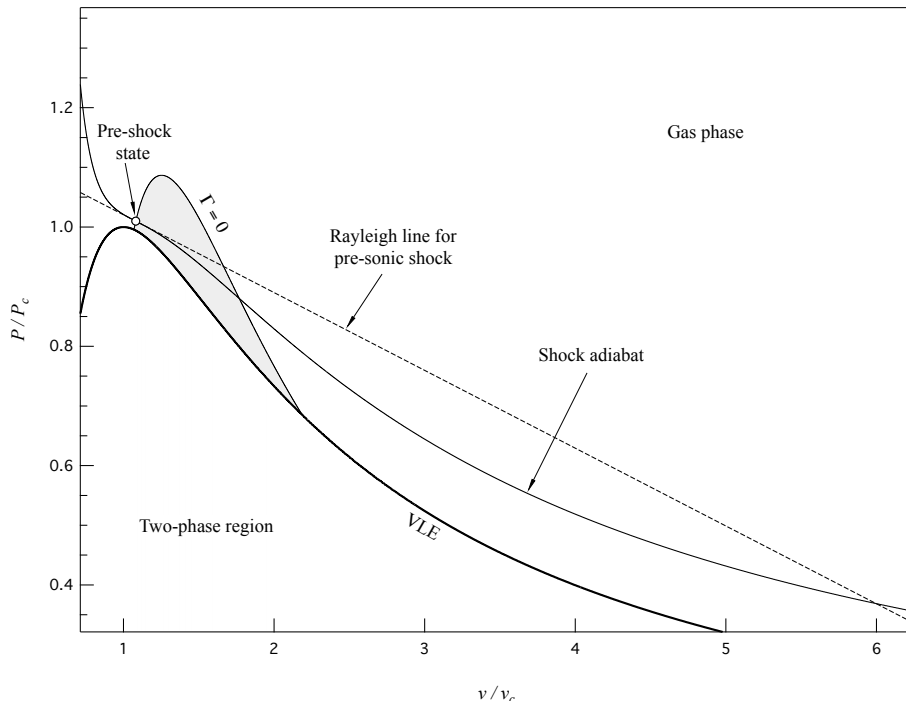


Figure 3.11: Shock adiabat through a point exhibiting null fundamental derivative, computed from the polytropic van der Waals model with  $\delta = 1/50$ . The Rayleigh line corresponds to a pre-sonic shock.

$$\mathcal{R}_{\mathcal{N}^{2+}}^{[7]} : \beta = \beta_7$$

The nozzle is adapted, the solution equals the previous one except for the exit shock. A major difference with respect to nozzle flows of polytropic ideal gases is that a complete expansion from rest to arbitrarily large Mach numbers cannot be attained isentropically. A pre-sonic rarefaction shock upstream of the throat is required.

The intermediate solutions layout, Fig. 3.12, is detailed as follows:

$$\mathcal{R}_{\mathcal{N}^{2+}}^{[0-1]} : \beta_1 < \beta < 1$$

The flow is subsonic all over the nozzle, which is not choked. The computation of this solution is identical to the same case for  $\mathcal{R}_{\mathcal{I}}$  functioning regime.

$$\mathcal{R}_{\mathcal{N}^{2+}}^{[1-2]} : \beta_2 < \beta < \beta_1$$

The flow is not choked, despite the throat being sonic with density  $\rho_{s_1}(s_{\text{res}})$ . The convergent portion is identical to case  $\mathcal{R}_{\mathcal{N}^{2+}}^{[1]}$ , as well as the mass flow rate. Downstream of the throat the flow is supersonic up to a generic compression shock, whose position is bounded above by the limiting pre-sonic compression shock of solution  $\mathcal{R}_{\mathcal{N}^{2+}}^{[2]}$ . The outflow is subsonic and the mass flow rate is known, so that the exit density is computed from Eq. (3.4). The entropy downstream of the shock is simply  $s_r = s(P_e, \rho_e)$ . Hence the upstream and downstream entropy values are known and system (3.5) can be used to compute the pre- and post-shock states. The unknown shock location is given by (3.6).

$$\mathcal{R}_{\mathcal{N}^{2+}}^{[2-3]} : \beta_3 < \beta < \beta_2$$

The solution consists of three isentropic branches matched by two shocks: a generic rarefaction shock and a pre-sonic compression shock. The convergent portion of the nozzle is equal to solution  $\mathcal{R}_{\mathcal{N}^{2+}}^{[2]}$ , so that the mass flow rate is the same. The first shock is bounded below by the throat shock of solution  $\mathcal{R}_{\mathcal{N}^{2+}}^{[3]}$  and bounded above by the pre-sonic compression shock of solution  $\mathcal{R}_{\mathcal{N}^{2+}}^{[2]}$ . This limiting shock is also the lower bound for the second shock, which is bounded above by the pre-sonic compression shock of solution  $\mathcal{R}_{\mathcal{N}^{2+}}^{[3]}$ . The occurrence of this second shock is due to the presence of three sonic points downstream of the first shock. As density assumes the sonic value  $\rho_{s_2}$ , relative to the entropy value in the central isentropic branch, the flow cannot be continued isentropically. The computation of the two discontinuities is now described. Similarly to other solutions with a known mass flow rate, Eq. (3.4) provides the exit density, from which the exit entropy is obtained. The latter represents the entropy value downstream of the second shock. Given that the shock is pre-sonic, the remaining pre- and post-shock quantities,

$$(\rho_l, \rho_r, s_l, M_r)$$

are computed by means of the following system,

$$\begin{cases} \rho_r M_r c(s_r, \rho_r) = \rho_l c(s_l, \rho_l) \\ P(s_r, \rho_r) + \rho_r M_r^2 c^2(s_r, \rho_r) = P(s_l, \rho_l) + \rho_l c^2(s_l, \rho_l) \\ h(s_r, \rho_r) + \frac{1}{2} M_r^2 c^2(s_r, \rho_r) = h^t \\ h(s_l, \rho_l) + \frac{1}{2} c^2(s_l, \rho_l) = h^t. \end{cases} \quad (3.9)$$

The quantity  $s_l$  is clearly the entropy value downstream of the preceding rarefaction shock. The upstream entropy is simply the reservoir value so that system (3.5) provides the remaining pre- and post-shock quantities. The two shocks locations are computed from Eq. (3.6).

$$\mathcal{R}_{\mathcal{N}^{2+}}^{[3-4]} : \beta_4 < \beta < \beta_3$$

As the ambient to reservoir pressure ratio decreases below  $\beta_3$ , the mass flow rate increases. The convergent portion is subsonic and sonic condition  $\rho_{s_1}(s_{\text{res}})$  occurs upstream of the throat. The upstream state is the same of the pre-sonic rarefaction shock of solution  $\mathcal{R}_{\mathcal{N}^{2+}}^{[3]}$  or  $\mathcal{R}_{\mathcal{N}^{2+}}^{[4]}$ . Therefore this solution presents the same shock but in a different location. The shock position is bounded above by the throat shock of limiting solution  $\mathcal{R}_{\mathcal{N}^{2+}}^{[3]}$  and bounded below by the rarefaction shock of solution  $\mathcal{R}_{\mathcal{N}^{2+}}^{[4]}$ . The throat is not sonic, so that the divergent portion initially consists of a compressive branch. Downstream of the previous shock isentropic pattern  $\mathcal{S}_{\mathcal{N}-}$  persists. Therefore, as density assumes the sonic value  $\rho_{s_2}(s_t)$ , a pre-sonic compression shock is required to continue the flow. The upstream state is equal to that of the pre-sonic compression shock of limiting solution  $\mathcal{R}_{\mathcal{N}^{2+}}^{[3]}$ . This shock is also the lower bound for the present shock, whereas the upper bound is represented by the pre-sonic compression shock of solution  $\mathcal{R}_{\mathcal{N}^{2+}}^{[4]}$ . Therefore any pressure ratios  $\beta_4 < \beta < \beta_3$  results in an intermediate solution including the same shocks of solution  $\mathcal{R}_{\mathcal{N}^{2+}}^{[3]}$ , located however in different positions.

For the computation of this solutions the mass flow rate is to be determined. The exit entropy  $s_e$  is known, being the same of  $\mathcal{R}_{\mathcal{N}^{2+}}^{[3]}$  or  $\mathcal{R}_{\mathcal{N}^{2+}}^{[4]}$ . Given that the outflow subsonic, the exit pressure equals the ambient value. Then the mass flow rate is given by

$$\dot{m} = f(\rho(P_e, s_e); s_e, h^t) A_e.$$

The three isentropic branches are computed through Eq. (3.2). Any pressure ratio  $\beta < \beta_4$  results in a choked flow.

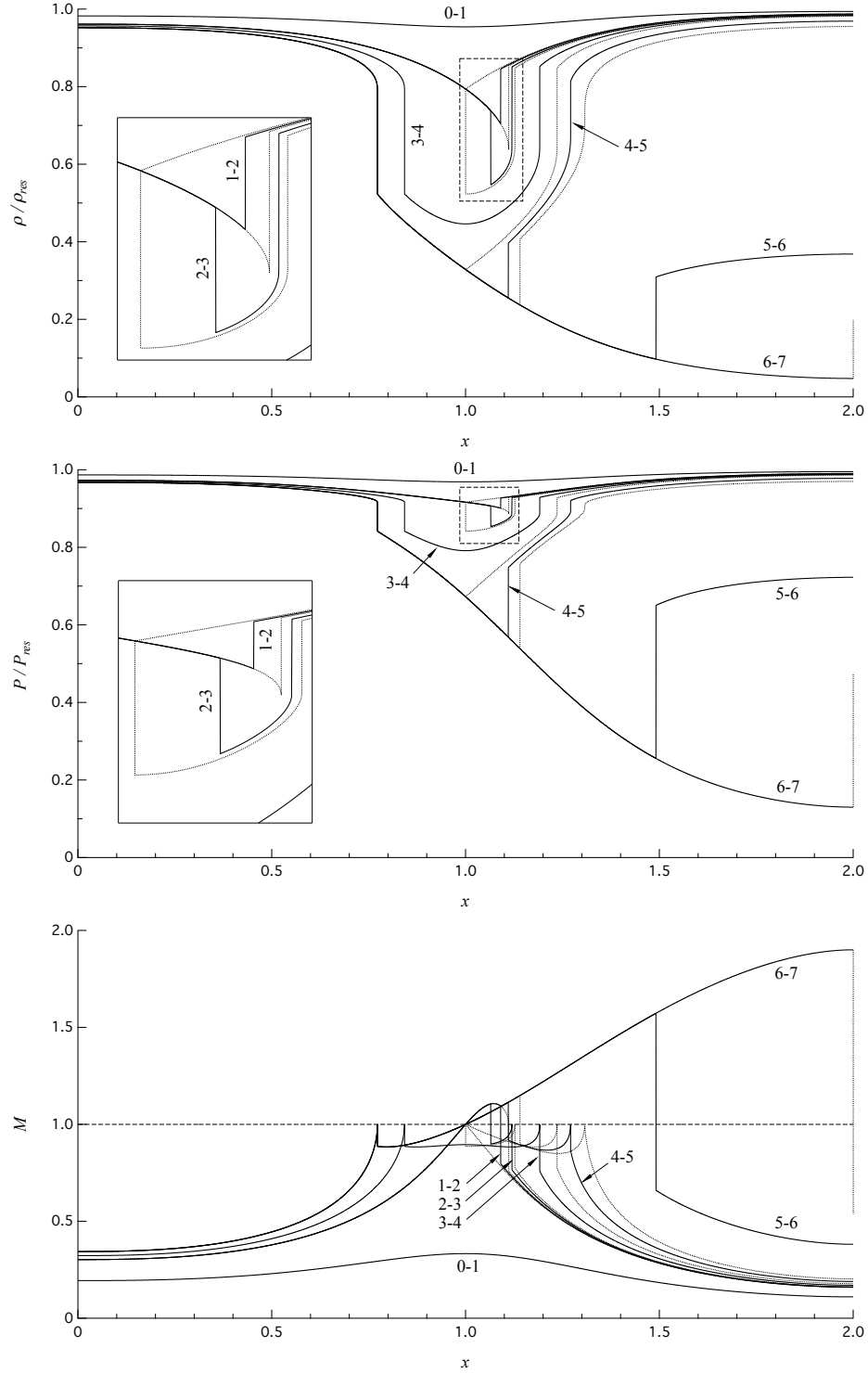


Figure 3.12: Density, pressure and Mach number intermediate solutions (continuous line) and limiting solutions (dotted line) for  $\mathcal{R}_{N^2+}$  functioning regime. Solutions computed from the polytropic van der Waals model with  $\delta = 1/50$ , corresponding to a BZT fluid. Reservoir conditions:  $v_{\text{res}} = 0.7818v_c$ ,  $P_{\text{res}} = 1.1168P_c$ .

$$\mathcal{R}_{\mathcal{N}^{2+}}^{[4-5]} : \beta_5 < \beta < \beta_4$$

This solution shows four isentropic branches separated by three discontinuities. The nozzle is choked and the convergent portion is identical to case  $\mathcal{R}_{\mathcal{N}^{2+}}^{[4]}$ . The divergent exhibits an initial supersonic branch up to the occurrence of a shock-splitting configuration. The latter is composed of two compression shocks. The isentropic pattern downstream of the first shock of the shock-splitting configuration is  $S_{\mathcal{N}^-}$ , i.e. no transition occurs. Therefore, denoting by  $s_r$  the entropy value downstream of it, as sonic density  $\rho_{s_2}(s_r)$  is reached, another shock is required. The computation follows that of intermediate solution  $\mathcal{R}_{\mathcal{N}^{2+}}^{[2-3]}$ . Equation (3.4) provides the exit density, from which the exit entropy is obtained. System (3.9) provides the pre- and post-shock states for the pre-sonic compression shock. Once determined the entropy value downstream of the first discontinuity of the shock-splitting configuration, system (3.5) allows the computation of pre- and post-shock quantities. Equation (3.6) is used to compute the two shocks locations.

$$\mathcal{R}_{\mathcal{N}^{2+}}^{[5-6]} : \beta_6 < \beta < \beta_5$$

The present solution equals limiting solution  $\mathcal{R}_{\mathcal{N}^{2+}}^{[7]}$  up to a generic compression shock in the divergent portion, whose position is bounded below by the compression shock of limiting solution  $\mathcal{R}_{\mathcal{N}^{2+}}^{[5]}$ . With respect to the previous intermediate solution, the shock-splitting configuration is now replaced by a single shock. Consider a point located on the isentropic branch downstream of the compression shock of limiting solution  $\mathcal{R}_{\mathcal{N}^{2+}}^{[5]}$ . As discussed above, any shocks originating from a similar state would cause an isentropic pattern transition, from three sonic points to one only. Therefore a single shock is observed, instead of the shock-splitting configuration. The mentioned discontinuity itself is computed exactly like the shock in intermediate solution  $\mathcal{R}_{\mathcal{N}^{2+}}^{[1-2]}$ , recalling however that the upstream entropy is not the reservoir value, but the entropy downstream of the limiting rarefaction shock upstream of the throat.

$$\mathcal{R}_{\mathcal{N}^{2+}}^{[6-7]} : \beta_7 < \beta < \beta_6$$

For any  $\beta_7 < \beta < \beta_6$  the solution equals case  $\mathcal{R}_{\mathcal{N}^{2+}}^{[7]}$  over the entire nozzle. The outflow is supersonic and the exit pressure is lower than the ambient value, causing an over-expanded jet outside of the nozzle.

Finally, when  $\beta < \beta_7$ , the solution is equal to  $\mathcal{R}_{\mathcal{N}^{2+}}^{[7]}$  over the entire nozzle and an under-expanded jet lies outside of the nozzle.

### Functioning regime $\mathcal{R}_{\mathcal{N}^{2-}}$

The present functioning regime is a slight variation of the previous one,  $\mathcal{R}_{\mathcal{N}^{2+}}$ , as the terms indicate. Actually, the only difference lies in one of the limiting

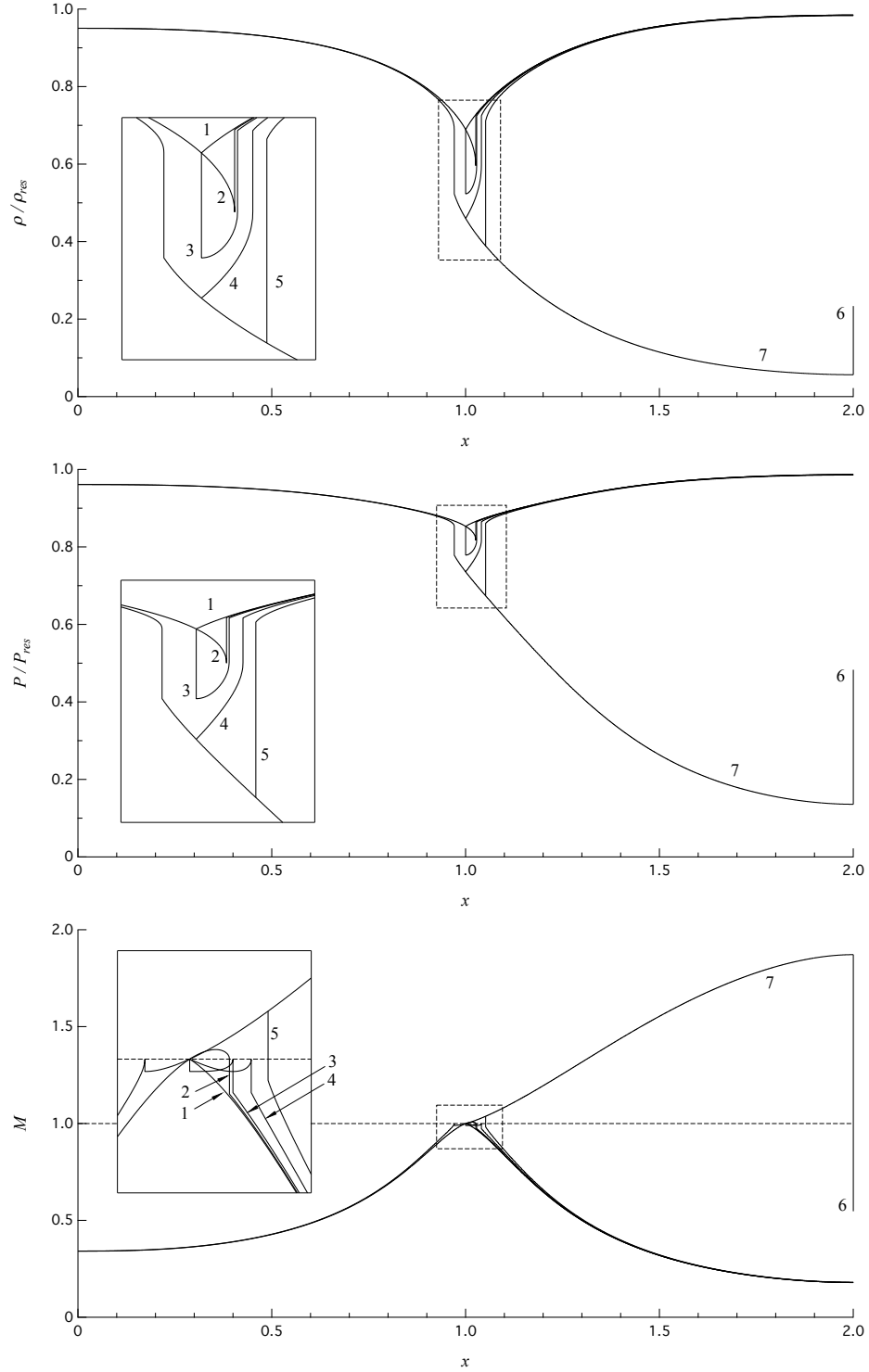


Figure 3.13: Density, pressure and Mach number limiting solutions for  $\mathcal{R}_{N^2-}$  functioning regime. Solutions computed from the polytropic van der Waals model with  $\delta = 1/50$ , corresponding to a BZT fluid. Reservoir conditions:  $v_{\text{res}} = 0.7880v_c$ ,  $P_{\text{res}} = 1.2931P_c$ .

solutions, the one which represents the end of the shock-splitting configuration. Limiting solutions are shown in Fig. 3.13. Solution  $\mathcal{R}_{\mathcal{N}^{2+}}^{[5]}$  is characterized by the presence of an infinite slope point, downstream of a generic compression shock. This is related to the isentropic pattern transition induced by the shock, from  $\mathcal{S}_{\mathcal{N}-}$  to  $\mathcal{S}_{\mathcal{N}-}/\mathcal{S}_{\mathcal{M}-}$ . Conversely, in the present case, no infinite slope points occur in the final isentropic branch. The shock delimiting the shock-splitting configuration in  $\mathcal{R}_{\mathcal{N}^{2-}}$  indeed induces no isentropic pattern transition. The peculiar property of the present shock is that it is tangent to the shock adiabat in an intermediate sonic step. That is, this shock can be seen as a unique, generic shock or as a composition of a post-sonic shock with a subsequent pre-sonic shock, Fig. 3.14. A slight change in the mass flux, namely the slope of the Rayleigh line from pre- to post-shock states, causes two different situations to occur. If the mass flux is larger a unique shock with generic pre- and post-shock states is observed. On the other hand, if the mass flux is lower the shock-splitting configuration occurs, see also [11, 22]. The intermediate sonic step is computed through the following system:

$$\begin{cases} \rho_r c(s_r, \rho_r) = \rho_l M_l c(s_l, \rho_l) \\ P(s_r, \rho_r) + \rho_r c^2(s_r, \rho_r) = P(s_l, \rho_l) + \rho_l M_l^2 c^2(s_l, \rho_l) \\ h(s_r, \rho_r) + \frac{1}{2} c^2(s_r, \rho_r) = h^t \\ h(s_l, \rho_l) + \frac{1}{2} M_l^2 c^2(s_l, \rho_l) = h^t. \end{cases} \quad (3.10)$$

With subscripts  $l$  and  $r$  for the pre- and post-shock variables, the quantities  $s_l = s_{\text{res}}$ ,  $M_r = 1$  and  $h^t$  are imposed, so that the unknown vector reduces to  $(\rho_l, \rho_r, M_l, s_r)$ . Once the post-shock state of the intermediate sonic step is obtained, we use this as a pre-shock state and, through Eq. (2.14), the sought post-shock state is determined. That is, the procedure simply consists in extending the Rayleigh line from the intermediate sonic step.

There is no need to show the intermediate solutions for the present case, since they are qualitatively the same of case  $\mathcal{R}_{\mathcal{N}^{2+}}$  and their computation is performed with the methods previously described.

### Functioning regime $\mathcal{R}_{\mathcal{N}^{1+}}$

Stagnation conditions exhibiting  $\mathcal{S}_{\mathcal{N}^+}$  isentropic pattern are selected. The flux function presents three sonic points, the one for highest density corresponding to the global maximum. Limiting solutions, shown in Fig. 3.15, are described as follows:

$$\mathcal{R}_{\mathcal{N}^{1+}}^{[0]} : \beta = 1$$

The exit pressure equals the reservoir value, no flow.

$$\mathcal{R}_{\mathcal{N}^{1+}}^{[1]} : \beta = \beta_1$$

Subsonic flow except at the throat station, which is sonic with density  $\rho_{s_1}(s_{\text{res}})$ . This value is related to the global maximum of the flux function, so that mass flow rate is the maximum dischargeable,

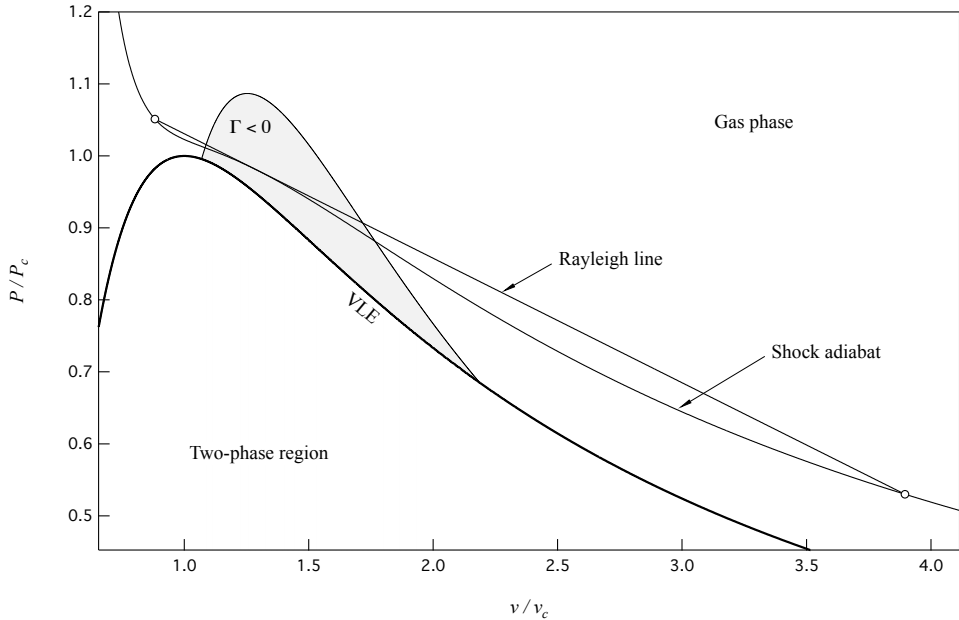


Figure 3.14: Compression shock with intermediate sonic step, in which the Rayleigh line is tangent to the shock adiabat, computed from a polytropic van der Waals model with  $\delta = 1/50$ . A slight decrease of the mass flux causes a shock-splitting configuration.

$$\dot{m} = \dot{m}_{\max} = \dot{m}_c(s_{\text{res}}, h^t)$$

and the nozzle is choked. This is the main difference with respect to  $\mathcal{R}_{\mathcal{N}^2}$  functioning regimes: no shock exist upstream of the throat section. The solution is computed exactly like  $\mathcal{R}_{\mathcal{I}}^{[1]}$  or  $\mathcal{R}_{\mathcal{N}^{2+}}^{[1]}$ . Any pressure ratios  $\beta < \beta_1$  result in a choked flow.

$$\mathcal{R}_{\mathcal{N}^{1+}}^{[2]} : \beta = \beta_2$$

The flow is choked and, like any other solution with  $\beta < \beta_1$ , the convergent portion of the nozzle is the same as solution  $\mathcal{R}_{\mathcal{N}^{1+}}^{[1]}$ . The divergent part of the nozzle is supersonic until density assumes the sonic value  $\rho_{s_2}(s_{\text{res}})$ . The occurrence of a shock is required to continue the flow. Downstream of the latter the flow is subsonic up to the exhaust section. The layout of the present solution, as well as the computation procedure, is identical to case  $\mathcal{R}_{\mathcal{N}^{2+}}^{[2]}$ .

$$\mathcal{R}_{\mathcal{N}^{1+}}^{[3]} : \beta = \beta_3$$

The current limiting solution consists of three isentropic branches matched by two shocks: a post-sonic rarefaction shock and a pre-sonic compression shock. For the first one, the unknown vector is  $(\rho_l, \rho_r, M_l, s_r)$  and given the known quantities  $s_l = s_{\text{res}}$  and  $h^t$ , system (3.10) is solved. Once the upstream and downstream states are obtained, the shock position is given by

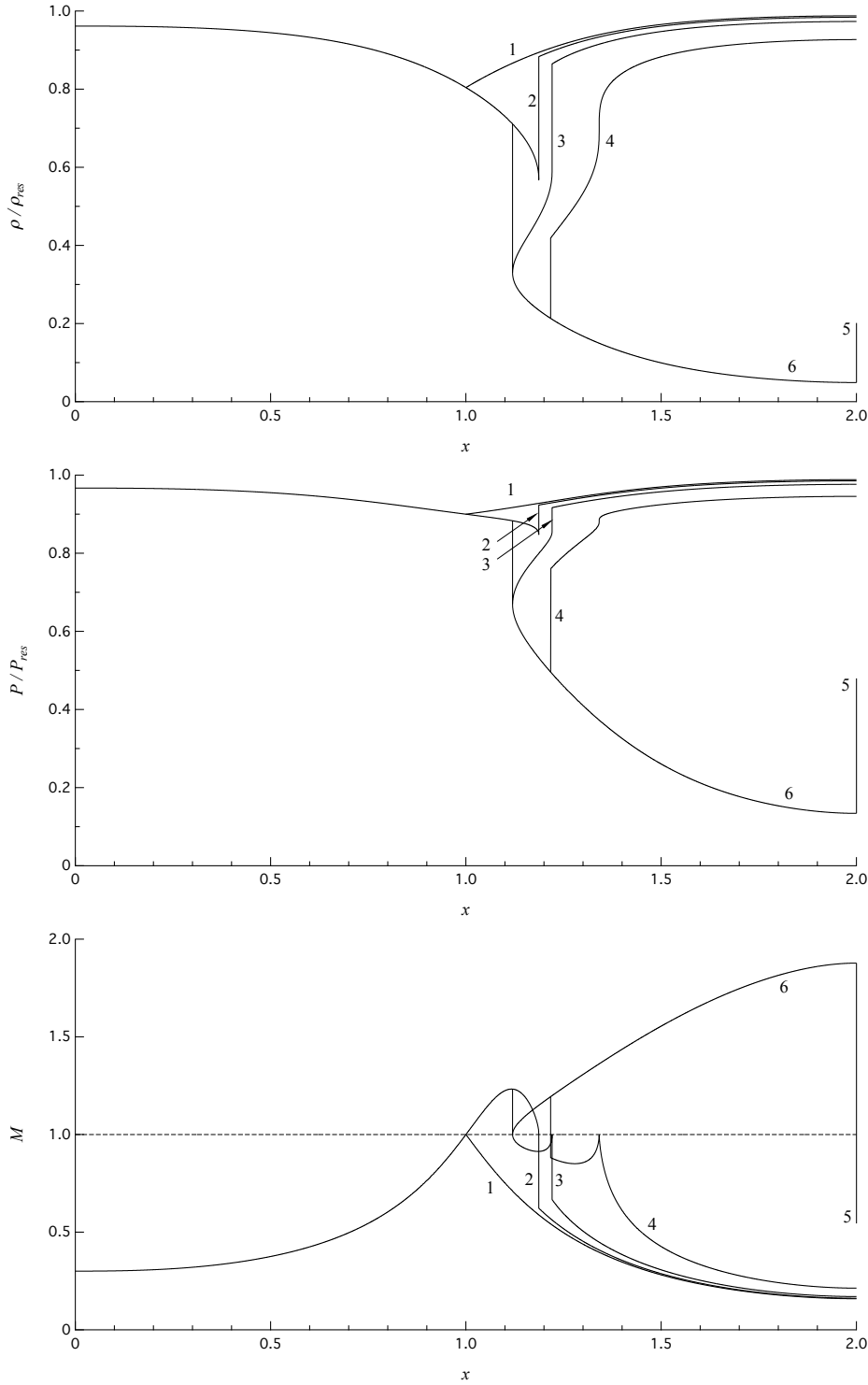


Figure 3.15: Density, pressure and Mach number limiting solutions for  $\mathcal{R}_{N^{1+}}$  functioning regime. Solutions computed from the polytropic van der Waals model with  $\delta = 1/50$ , corresponding to a BZT fluid. Reservoir conditions:  $v_{\text{res}} = 0.7600v_c$ ,  $P_{\text{res}} = 1.1453P_c$ .

the mass balance equation, Eq. (3.6). Downstream of the forementioned shock the isentropic pattern shows again three sonic points (in this case whether it is  $\mathcal{S}_{\mathcal{N}^+}$  or  $\mathcal{S}_{\mathcal{N}^-}$  is not relevant). The flow follows a compressive branch up to the sonic point corresponding to the local minimum of the related flux function,  $\rho_{s_2}(s_r)$ . The flow cannot be continued isentropically and a pre-sonic compression shock is required. The post-shock state is computed with the same procedure used for other solutions including the current type of shock. Equation (3.2) finally provides the solution in the three isentropic branches.

$$\mathcal{R}_{\mathcal{N}^{1+}}^{[4]} : \beta = \beta_4$$

For any  $\beta < \beta_3$  the solution equals  $\mathcal{R}_{\mathcal{N}^{1+}}^{[3]}$  up to the post-sonic rarefaction shock. In this case, downstream of the latter, the flow continues the expansion. A compression shock occurs, causing an isentropic pattern transition from three sonic points to two. That is, the post-shock isentropic pattern is precisely the one realizing transition  $\mathcal{S}_{\mathcal{N}^-}/\mathcal{S}_{\mathcal{M}^-}$ . It is the same configuration exhibited by limiting solution  $\mathcal{R}_{\mathcal{N}^{2+}}^{[5]}$ . The solution up to the post-sonic rarefaction shock is available from the previous limiting solution, whereas the following compression shock is computed as in  $\mathcal{R}_{\mathcal{N}^{2+}}^{[5]}$ .

$$\mathcal{R}_{\mathcal{N}^{1+}}^{[5]} : \beta = \beta_5$$

The solution represents a complete expansion up to a compression shock which occurs at the exhaust sections of the nozzle.

$$\mathcal{R}_{\mathcal{N}^{1+}}^{[6]} : \beta = \beta_6$$

The nozzle is adapted and the solution equals the previous one except for the exit shock. Similarly to functioning regimes  $\mathcal{R}_{\mathcal{N}^{2+}}$  and  $\mathcal{R}_{\mathcal{N}^{2-}}$ , a complete expansion from rest to arbitrarily large Mach numbers cannot be attained isentropically, requiring instead the presence of a rarefaction shock. However, in this case the shock is post-sonic and located downstream of the throat section.

Representative intermediate solutions are shown in Fig. 3.16 and are detailed as follows:

$$\mathcal{R}_{\mathcal{N}^{1+}}^{[0-1]} : \beta_1 < \beta < 1$$

The flow is subsonic all over the nozzle, which is not choked. The computation is similar to case  $\mathcal{R}_{\mathcal{T}}^{[1]}$ .

$$\mathcal{R}_{\mathcal{N}^{1+}}^{[1-2]} : \beta_2 < \beta < \beta_1$$

The nozzle is choked. The present solution is qualitatively similar to  $\mathcal{R}_{\mathcal{N}^{2+}}^{[1-2]}$ , though now the mass flow rate is the maximum dischargeable by

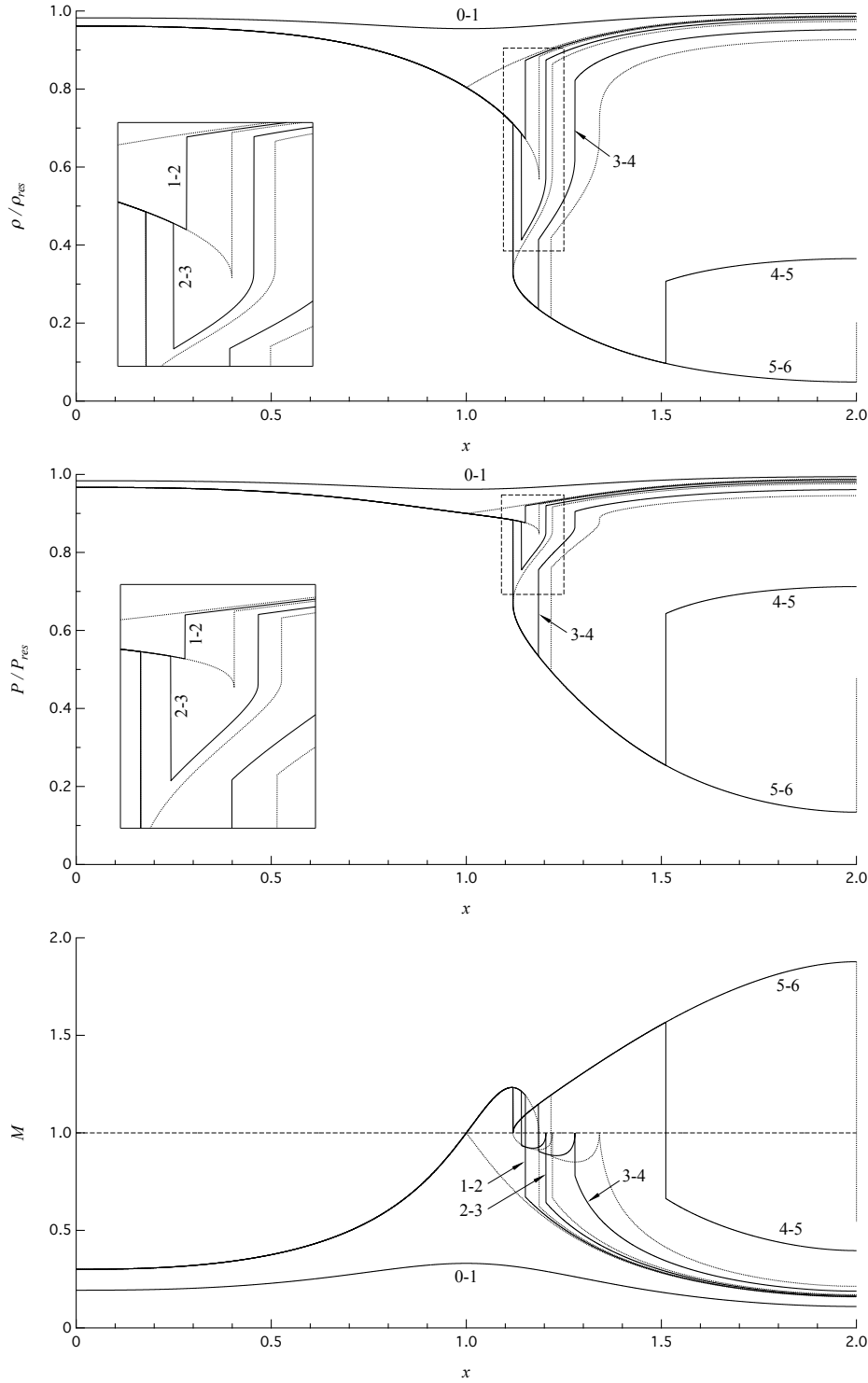


Figure 3.16: Density, pressure and Mach number intermediate solutions (continuous line) and limiting solutions (dotted line) for  $\mathcal{R}_{N^{2+}}$  functioning regime. Solutions computed from the polytropic van der Waals model with  $\delta = 1/50$ , corresponding to a BZT fluid. Reservoir conditions:  $v_{\text{res}} = 0.7600v_c$ ,  $P_{\text{res}} = 1.1453P_c$ .

the nozzle. Downstream of the throat section the flow is supersonic up to a generic compression shock. The latter is bounded above by the limiting shock of solution  $\mathcal{R}_{\mathcal{N}^{1+}}^{[2]}$ . See  $\mathcal{R}_{\mathcal{N}^{2+}}^{[1-2]}$  for the computation.

$$\mathcal{R}_{\mathcal{N}^{1+}}^{[2-3]} : \beta_3 < \beta < \beta_2$$

The layout of the present solution is similar to  $\mathcal{R}_{\mathcal{N}^{2+}}^{[2-3]}$ . Three isentropic branches are matched by a generic rarefaction shock and a pre-sonic compression shock. The first shock is bounded below by the post-sonic shock of limiting solution  $\mathcal{R}_{\mathcal{N}^{1+}}^{[3]}$  and bounded above by the pre-sonic shock of  $\mathcal{R}_{\mathcal{N}^{1+}}^{[2]}$ . Unlike functioning regimes  $\mathcal{R}_{\mathcal{N}^{2+}}$  and  $\mathcal{R}_{\mathcal{N}^{2-}}$ , in  $\mathcal{R}_{\mathcal{N}^{1+}}$  rarefaction shocks cannot exist arbitrarily close to the throat. The second shock is bounded below and above by the pre-sonic compression shocks of solutions  $\mathcal{R}_{\mathcal{N}^{1+}}^{[2]}$  and  $\mathcal{R}_{\mathcal{N}^{1+}}^{[3]}$  respectively. The computation is similar to case  $\mathcal{R}_{\mathcal{N}^{2+}}^{[2-3]}$ .

$$\mathcal{R}_{\mathcal{N}^{1+}}^{[3-4]} : \beta_4 < \beta < \beta_3$$

The solution equals  $\mathcal{R}_{\mathcal{N}^{1+}}^{[4]}$  up to a shock-splitting configuration which occurs downstream of the post-sonic rarefaction shock. The computation of the shock-splitting structure is explained in intermediate solution  $\mathcal{R}_{\mathcal{N}^{2+}}^{[4-5]}$ . Equation (3.6) provides the locations of the two shocks. The first two isentropic branches, separated by the post-sonic rarefaction shock, are available from limiting solution  $\mathcal{R}_{\mathcal{N}^{1+}}^{[4]}$ .

$$\mathcal{R}_{\mathcal{N}^{1+}}^{[4-5]} : \beta_5 < \beta < \beta_4$$

The present solution equals limiting solution  $\mathcal{R}_{\mathcal{N}^{1+}}^{[6]}$  up to a generic compression shock in the divergent. Its position is bounded below by the compression shock of solution  $\mathcal{R}_{\mathcal{N}^{1+}}^{[4]}$ . Similarly to  $\mathcal{R}_{\mathcal{N}^{2+}}^{[5-6]}$ , the shock-splitting configuration is replaced by a simple shock. The computation is carried out in the same way.

$$\mathcal{R}_{\mathcal{N}^{1+}}^{[5-6]} : \beta_6 < \beta < \beta_5$$

For any  $\beta_6 < \beta < \beta_5$  the solution equals  $\mathcal{R}_{\mathcal{N}^{1+}}^{[6]}$  all over the nozzle. The outflow is supersonic and the exit pressure is lower than the ambient value, causing an over-expanded jet outside of the nozzle.

Finally, when  $\beta < \beta_6$ , the solution is equal to  $\mathcal{R}_{\mathcal{N}^{1+}}^{[6]}$  over the entire nozzle and an under-expanded jet lies outside of the nozzle.

### Functioning regime $\mathcal{R}_{\mathcal{N}^{1-}}$

Previous discussion on  $\mathcal{R}_{\mathcal{N}^{2+}}$  and  $\mathcal{R}_{\mathcal{N}^{2-}}$  nozzle flows has remarked that the transition between the shock-splitting and the simple shock configurations can be performed in two different ways:

- A shock with downstream isentropic pattern corresponding to transition  $\mathcal{S}_{\mathcal{N}^-}/\mathcal{S}_{\mathcal{M}^-}$ . Shocks occurring ahead of this limiting shock exhibit a downstream isentropic pattern with three sonic points. Then another shock is required as soon as density assumes the sonic value  $\rho_{s_2}$ . Shocks occurring downstream of the limiting shock exhibit a downstream isentropic pattern with one sonic point only. A simple shock configuration takes place. This is the type of transition shown by  $\mathcal{R}_{\mathcal{N}^{2+}}$  and  $\mathcal{R}_{\mathcal{N}^{1+}}$ , i.e. by functioning regimes denoted with a '+' symbol.
- A shock which induces no transition from three to one sonic point. Rather, this shock is tangent to the shock adiabat in an intermediate sonic step. This is the type of transition shown by  $\mathcal{R}_{\mathcal{N}^{2-}}$  and by the current functioning regime,  $\mathcal{R}_{\mathcal{N}^{1-}}$ . The '-' symbol indicates this circumstance.

Figure 3.17 shows the limiting solutions pattern for  $\mathcal{R}_{\mathcal{N}^{1-}}$  functioning regime. As mentioned, the only difference with respect to  $\mathcal{R}_{\mathcal{N}^{1+}}$  lies in limiting solution  $\mathcal{R}_{\mathcal{N}^{1-}}^{[4]}$ . The computation of the shock which distinguish the shock-splitting and the simple shock configuration has already been explained in  $\mathcal{R}_{\mathcal{N}^{2-}}^{[5]}$ .

### Functioning regime $\mathcal{R}_{\mathcal{M}^+}$

Functioning regime  $\mathcal{R}_{\mathcal{M}^+}$  was introduced for HMC fluids. The current functioning regime presents the same features seen for HMC fluids. That is, the limiting solutions layout is the same. In order to observe this regime, stagnation conditions exhibiting  $\mathcal{S}_{\mathcal{M}^+}$  isentropic pattern are selected. An important remark should be made. Recalling (2.26), any transition could be observed from this isentropic pattern. We stress however that the current functioning regime exhibits the same layout of limiting solutions observed for HMC fluid, despite the possible shock-induced isentropic pattern transitions.

### Functioning regime $\mathcal{R}_{\mathcal{N}^3}$

In the description of functioning regime  $\mathcal{R}_{\mathcal{M}^+}$ , shock-induced transitions of isentropic patterns were found not to affect the limiting solutions layout, with respect to what observed for HMC fluids. On the contrary, for  $\mathcal{R}_{\mathcal{N}^3}$  functioning regime these transitions are significant and lead to an alteration of the limiting solutions pattern, shown in Fig. 3.18. Limiting solutions are detailed below:

$$\mathcal{R}_{\mathcal{N}^3}^{[0]} : \beta = 1$$

Not displayed, no flow occurs.

$$\mathcal{R}_{\mathcal{N}^3}^{[1]} : \beta = \beta_1$$

The usual subsonic-sonic-subsonic solution. The nozzle is choked.

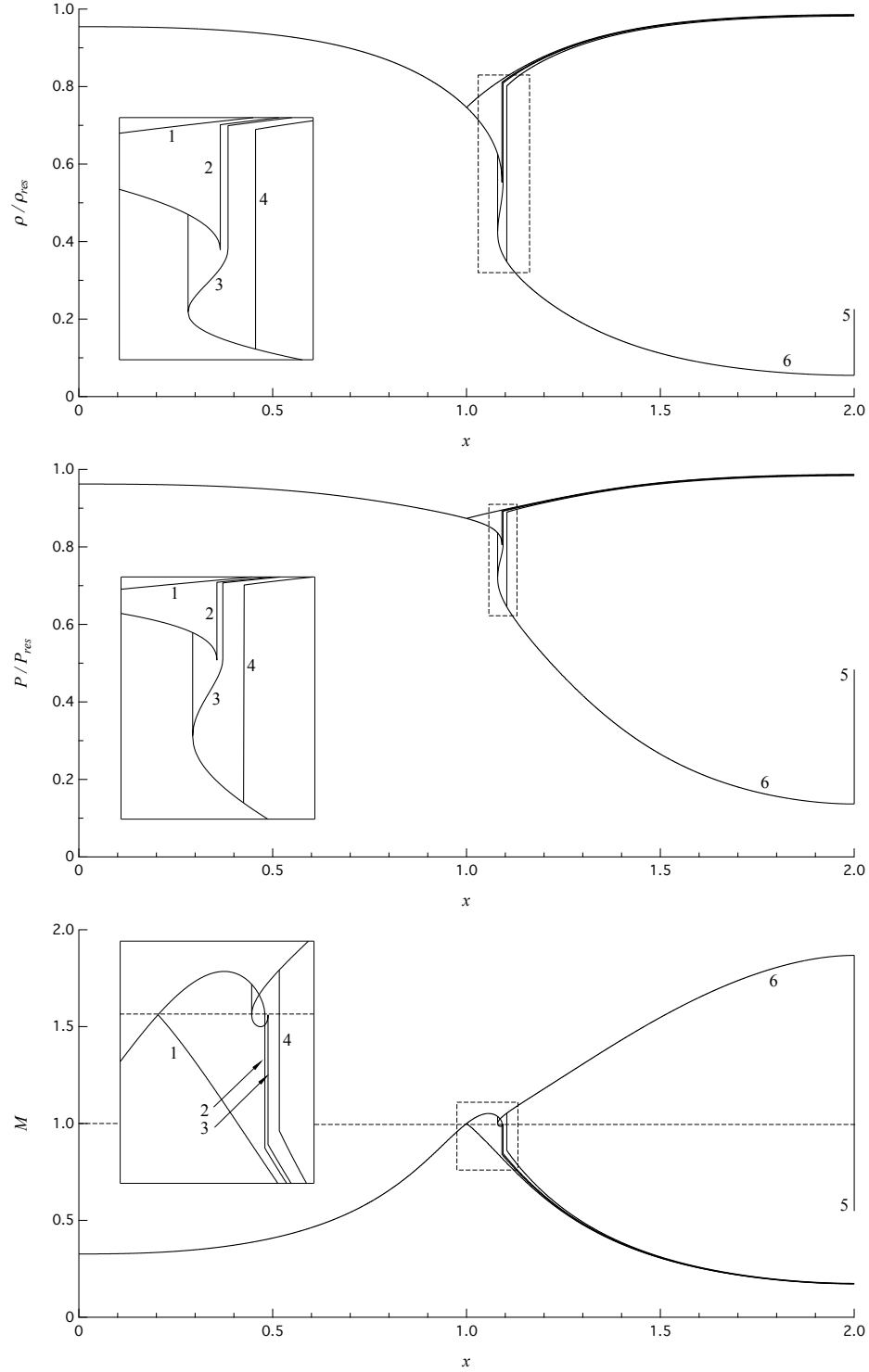


Figure 3.17: Density, pressure and Mach number limiting solutions for  $\mathcal{R}_{N^1-}$  functioning regime. Solutions computed from the polytropic van der Waals model with  $\delta = 1/50$ , corresponding to a BZT fluid. Reservoir conditions:  $v_{\text{res}} = 0.7760v_c$ ,  $P_{\text{res}} = 1.2576P_c$ .

$$\mathcal{R}_{\mathcal{N}^3}^{[2]} : \beta = \beta_2$$

This solution determines the beginning of a shock-splitting region. It contains a shock which has generic upstream and downstream states but it is tangent to the shock adiabat in an intermediate sonic step. This is the same discontinuity which closes the shock-splitting configuration in limiting solutions  $\mathcal{R}_{\mathcal{N}^2-}^{[5]}$  and  $\mathcal{R}_{\mathcal{N}^1-}^{[4]}$ . See the discussion related to the mentioned solutions for the computation of this limiting shock.

$$\mathcal{R}_{\mathcal{N}^3}^{[3]} : \beta = \beta_3$$

The present limiting solution determines the end of the shock-splitting configuration. It is carried out by a shock which provides an isentropic pattern transition from  $\mathcal{S}_{\mathcal{M}+}$  to transition  $\mathcal{S}_{\mathcal{N}-}/\mathcal{S}_{\mathcal{M}-}$ . The computation of this part of the solution is performed as in limiting solutions  $\mathcal{R}_{\mathcal{N}^2+}^{[5]}$  and  $\mathcal{R}_{\mathcal{N}^1+}^{[4]}$ .

$$\mathcal{R}_{\mathcal{N}^3}^{[4]} : \beta = \beta_4$$

Complete isentropic expansion up to exhaust section, where a shock takes place.

$$\mathcal{R}_{\mathcal{N}^3}^{[5]} : \beta = \beta_5$$

Adapted nozzle, the variables equal the previous case except for the exit shock.

Representative intermediate solutions, shown in Fig. 3.19, are described as follows:

$$\mathcal{R}_{\mathcal{N}^3}^{[0-1]} : \beta_1 < \beta < 1$$

This is the usual completely subsonic solution relative to a non-choked flow.

$$\mathcal{R}_{\mathcal{N}^3}^{[1-2]} : \beta_2 < \beta < \beta_1$$

The flow is choked and a single shock occurs downstream of the throat. Its location is bounded above by the shock of limiting solution  $\mathcal{R}_{\mathcal{N}^3}^{[2]}$ .

$$\mathcal{R}_{\mathcal{N}^3}^{[2-3]} : \beta_3 < \beta < \beta_2$$

The present solution exhibits a shock-splitting configuration. The first shock determines an isentropic pattern transition from  $\mathcal{S}_{\mathcal{M}+}$  to a pattern with three sonic points,  $\mathcal{S}_{\mathcal{N}+}$  or  $\mathcal{S}_{\mathcal{N}-}$ . Downstream of this shock a compressive branch is followed until density reaches sonic value  $\rho_{s2}$  (relative to the post-shock flux function). A pre-sonic compression shock is required to continue the flow. To compute this part of the solution see  $\mathcal{R}_{\mathcal{N}^2+}^{[4-5]}$  or

any other solution containing a shock-splitting configuration.

$$\mathcal{R}_{\mathcal{N}^3}^{[3-4]} : \beta_4 < \beta < \beta_3$$

For  $\beta < \beta_3$  a single shock occurs, downstream of the shock of limiting solution  $\mathcal{R}_{\mathcal{N}^3}^{[3]}$ . The shock induces a transition to an isentropic pattern displaying one sonic point only, namely  $\mathcal{S}_{\mathcal{M}^-}$  or  $\mathcal{S}_{\mathcal{I}}$ .

$$\mathcal{R}_{\mathcal{N}^3}^{[4-5]} : \beta_5 < \beta < \beta_4$$

The solution equals  $\mathcal{R}_{\mathcal{N}^3}^{[5]}$  over the entire nozzle. An over expanded jet is present outside of the nozzle.

Finally, when  $\beta < \beta_5$ , the solution is equal to  $\mathcal{R}_{\mathcal{N}^3}^{[5]}$  over the entire nozzle and an under-expanded jet lies outside of the nozzle.

### 3.6 Summary of functioning regimes

Nozzle flows of BZT exhibit the most interesting behavior due to the impossibility, for certain reservoir conditions, to attain a complete isentropic expansion, from rest to arbitrarily large Mach numbers. Complex limiting solutions layouts have been observed when the isentropic pattern related to an isentropic branch exhibits three sonic points. With respect to LMC and HMC fluids, six new regimes were introduced. Functioning regime  $\mathcal{R}_{\mathcal{M}^-}$  is a slight variation of  $\mathcal{R}_{\mathcal{I}}$ , since they differ only in the subsonic Mach number behavior. Two classes,  $\mathcal{R}_{\mathcal{N}^1}$  and  $\mathcal{R}_{\mathcal{N}^2}$  exhibit the full non-ideal features of BZT fluids. For these regimes a complete isentropic expansion cannot be attained isentropically, indeed a rarefaction shock is required. In  $\mathcal{R}_{\mathcal{N}^2}$  this is a pre-sonic rarefaction shock located upstream of the throat section. For  $\mathcal{R}_{\mathcal{N}^1}$  the shock is post-sonic and located downstream of the throat. Inside each of the two classes another distinction has been made, based upon the shape of limiting solution identifying the transition from a shock-splitting to a simple shock configuration. Functioning regime  $\mathcal{R}_{\mathcal{M}^+}$  exhibits the same limiting solutions layout observed for HMC fluid, whereas in  $\mathcal{R}_{\mathcal{N}^3}$  shock-induced transitions of isentropic pattern are significant and lead to the possibility of shock-splitting configurations. The following Table 3.1 summarizes the possible regimes the different classes can exhibit. We stress that, despite the possible isentropic pattern transitions which a shock may possibly induce,  $\mathcal{R}_{\mathcal{M}^+}$  functioning regime for HMC and BZT fluids should be considered equivalent, since they exhibit the same limiting solutions layout.

LMC	$\mathcal{R}_{\mathcal{I}}$
HMC	$\mathcal{R}_{\mathcal{I}}, \mathcal{R}_{\mathcal{M}^+}$
BZT	$\mathcal{R}_{\mathcal{I}}, \mathcal{R}_{\mathcal{M}^-}, \mathcal{R}_{\mathcal{N}^1-}, \mathcal{R}_{\mathcal{N}^1+}, \mathcal{R}_{\mathcal{N}^2-}, \mathcal{R}_{\mathcal{N}^2+}, \mathcal{R}_{\mathcal{M}^+}, \mathcal{R}_{\mathcal{N}^3}$

Table 3.1: Possible functioning regimes for the different fluid classes.

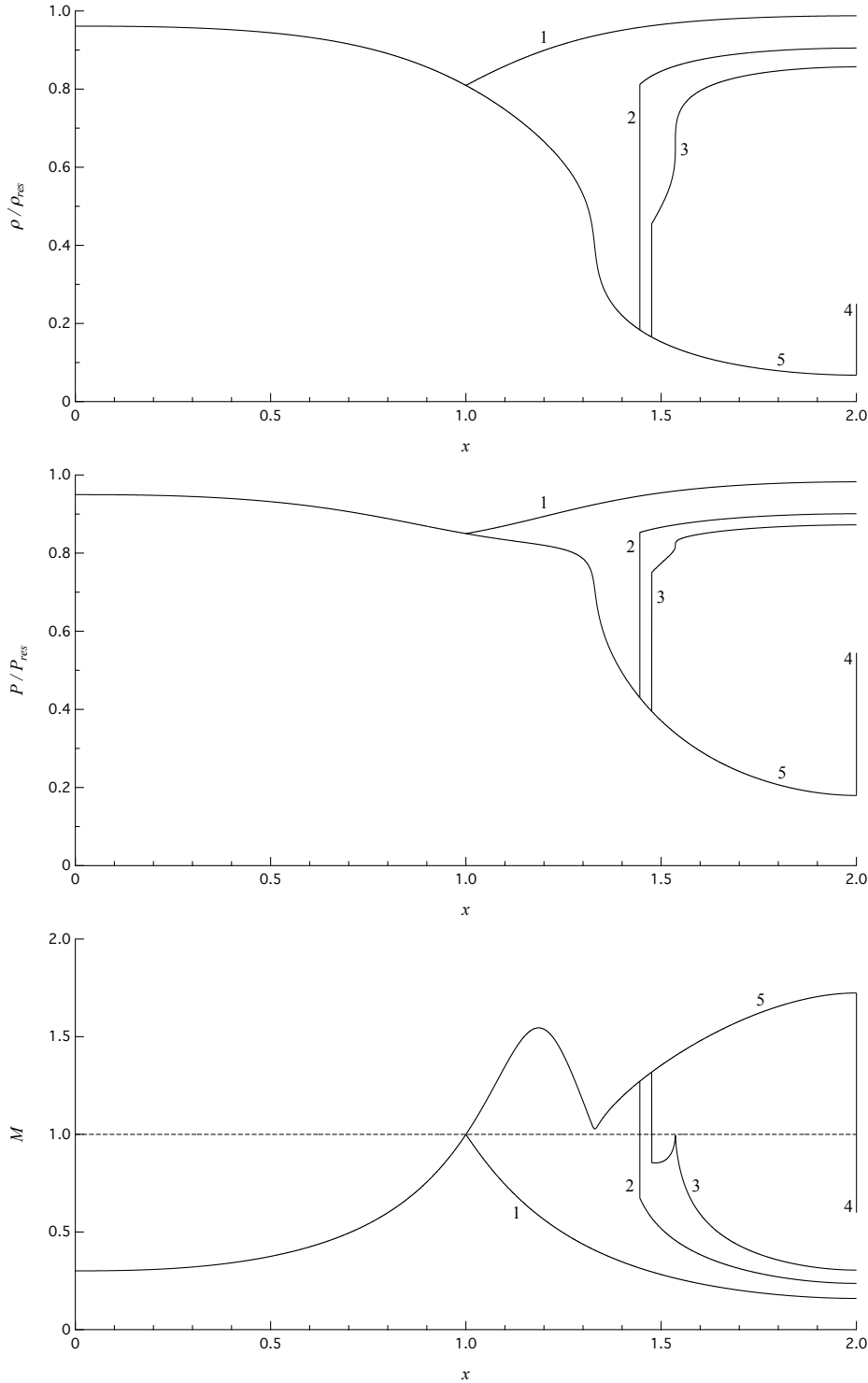


Figure 3.18: Density, pressure and Mach number limiting solutions for  $\mathcal{R}_{N^3}$  functioning regime. Solutions computed from the polytropic van der Waals model with  $\delta = 1/50$ , corresponding to a BZT fluid. Reservoir conditions:  $v_{\text{res}} = 0.6775v_c$ ,  $P_{\text{res}} = 1.3566P_c$ .

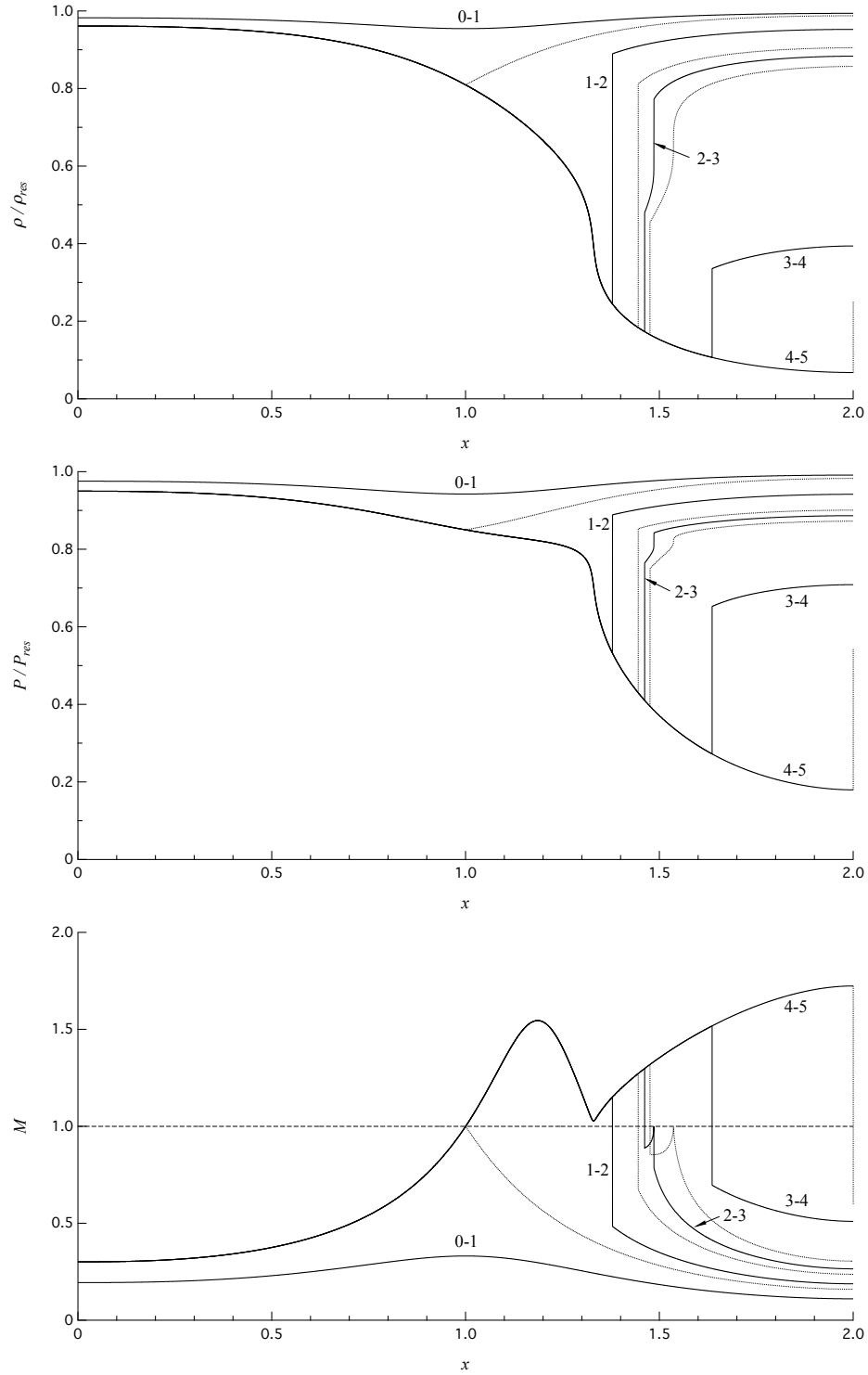


Figure 3.19: Density, pressure and Mach number intermediate solutions (continuous line) and limiting solutions (dotted line) for  $\mathcal{R}_{N^3}$  functioning regime. Solutions computed from the polytropic van der Waals model with  $\delta = 1/50$ , corresponding to a BZT fluid. Reservoir conditions:  $v_{\text{res}} = 0.6775v_c$ ,  $P_{\text{res}} = 1.3566P_c$ .

## Chapter 4

# Comparison with a quasi 1-D shock capturing method

The present chapter presents a comparison between some of the previously computed exact solutions and the numerical solutions of a shock capturing method. First and second order results are presented and are found to agree with the exact solutions. Two main approaches can be used in the computation of steady states: methods specifically designed to compute stationary solutions and time-marching methods. The latter approach is undertaken in the present work and amounts to determine the steady state by starting with some arbitrary initial data and then marching forward in time until a steady state is reached [28].

### 4.1 Governing equations for quasi 1-D unsteady flow

In order to use a time-marching method, the governing equations for unsteady flows are recalled. Under the requirements of the quasi 1-D approximation, all properties are assumed to spatially vary only along the streamwise direction and the governing equations can be written as

$$\begin{cases} \frac{\partial}{\partial t}(\rho A) + \frac{\partial}{\partial x}(\rho u A) = 0 \\ \frac{\partial}{\partial t}(\rho u A) + \frac{\partial}{\partial x}(\rho u^2 A + P A) = P \frac{dA}{dx} \\ \frac{\partial}{\partial t}(\rho e^t A) + \frac{\partial}{\partial x}((\rho e^t + P)u A) = 0, \end{cases} \quad (4.1)$$

where,  $e^t = e + u^2/2$  is the specific total energy and  $A = A(x)$ . Introducing

$$R = \rho A, \quad M = \rho u A, \quad \Sigma^t = \rho e^t A,$$

as the balance variables, Eq. (4.1) is the general form of a 1-D balance law with spatially varying flux and source term:

$$\frac{\partial}{\partial t}\mathbf{w} + \frac{\partial}{\partial x}\mathbf{f}(\mathbf{w}, x) = \boldsymbol{\psi}(\mathbf{w}, x), \quad (4.2)$$

with

$$\mathbf{w} = \begin{bmatrix} R \\ M \\ \Sigma^t \end{bmatrix} \quad \mathbf{f}(\mathbf{w}, x) = \begin{bmatrix} M \\ M^2/R + \tilde{\Pi} \\ (\Sigma^t + \Pi)M/R \end{bmatrix} \quad \psi(\mathbf{w}, x) = \frac{A'}{A} \begin{bmatrix} 0 \\ \tilde{\Pi} \\ 0 \end{bmatrix}. \quad (4.3)$$

The function  $\tilde{\Pi}$  expresses the pressure as a function of the balance variables. With the thermodynamic equation of state assumed in the form  $P = P(e, \rho)$ , the closure of the hyperbolic system is provided by the introduction of the composed function of the balance variables:

$$\tilde{\Pi}(\mathbf{w}, x) = P \left( \frac{\Sigma^t}{R} - \frac{M^2}{2R^2}, \frac{R}{A} \right) A.$$

If the flux function is spatially varying,  $\mathbf{f} = \mathbf{f}(\mathbf{w}, x)$ , then the balance law is said to be *non autonomous*. On the contrary, when the flux function depends only on the vector of balance variables,  $\mathbf{f} = \mathbf{f}(\mathbf{w})$ , the balance law is *autonomous*. In the present case, whether the balance law is autonomous or not, depends on the  $\tilde{\Pi}$  function. It is easy to see that in the very simple case of a polytropic ideal gas,  $\tilde{\Pi} = \tilde{\Pi}(\mathbf{w})$ , whereas for more complex equation of state, like the polytropic van der Waals one,  $\tilde{\Pi} = \tilde{\Pi}(\mathbf{w}, x)$ . Therefore in our case, system (4.1) is actually a non autonomous balance law. However, it turns out that it is possible to modify the equations in order to obtain an autonomous system of balance laws, which is more simple to deal with. Given:

$$m = \rho u, \quad E^t = \rho e^t,$$

system (4.1) may be rewritten in form 4.2, with:

$$\mathbf{w} = \begin{bmatrix} \rho \\ m \\ E^t \end{bmatrix} \quad \mathbf{f}(\mathbf{w}) = \begin{bmatrix} m \\ m^2/\rho + \Pi \\ (E^t + \Pi)m/\rho \end{bmatrix} \quad \psi(\mathbf{w}, x) = -\frac{A'}{A} \begin{bmatrix} m \\ m^2/\rho \\ (E^t + \Pi)m/\rho \end{bmatrix}. \quad (4.4)$$

Here the function:

$$\Pi(\mathbf{w}) = P \left( \frac{E^t}{\rho} - \frac{m^2}{2\rho^2}, \rho \right)$$

is not spatially varying, since it does not include a dependence on the cross sectional area. Both formulations (4.3) and (4.4) will be tested, especially to inspect whether the different form of the source terms influences the numerical results.

## 4.2 Numerical methods for balance laws

Several numerical methods have been proposed to take into account the presence of a source term in a conservation law. We recall here three simple methods in the finite volume context.

### Jin's formula

Let  $\mathbf{W}_j(t)$  represent a discrete approximation to the cell average of  $\mathbf{w}$  over the  $j$ th cell,  $x_{j-1/2} < x < x_{j+1/2}$ , at time  $t$ :

$$\mathbf{W}_j(t) \approx \frac{1}{\Delta x_j} \int_{x_{j-1/2}}^{x_{j+1/2}} \mathbf{w}(x, t) dx \quad (4.5)$$

and let  $\mathbf{F}_{j+1/2}$  approximate the interface flux  $\mathbf{f}(\mathbf{w}(x_{j+1/2}, t))$ . Then the semi-discrete form of the balance law (4.2) is

$$\frac{d}{dt} \mathbf{W}_j = -\frac{1}{\Delta x_j} (\mathbf{F}_{j+1/2} - \mathbf{F}_{j-1/2}) + \frac{1}{\Delta x_j} \int_{x_{j-1/2}}^{x_{j+1/2}} \psi(\mathbf{w}(x, t), x) dx. \quad (4.6)$$

A similar procedure is performed by some of the so-called *unsplitted* methods. The numerical flux can be one of the standard numerical fluxes used for conservation laws, for instance the Roe flux. The critical part is handling the source term. It is well-known that using a space-centered numerical source leads to spurious numerical results. A convenient property of a numerical method for balance law is the *well-balancing*, which means that the method is able to preserve steady state numerically. This is indeed important here, since the time-marching method is used to reach a steady state condition. A simple way to handle geometrical source terms,

$$\psi(\mathbf{w}, x) = -z'(x) \mathbf{b}(\mathbf{w}) \quad (4.7)$$

is given by Jin [19]. The proposed method preserves steady state solutions approximately with a formally second order accuracy at the cell interfaces. In Jin's formula, the treatment of the source term in (4.6) is

$$\frac{1}{\Delta x_j} \int_{x_{j-1/2}}^{x_{j+1/2}} \psi(\mathbf{w}, x) dx \approx -\frac{z_{j+1/2} - z_{j-1/2}}{\Delta x_j} \frac{\mathbf{b}_{j+1/2} + \mathbf{b}_{j-1/2}}{2}, \quad (4.8)$$

where  $\mathbf{b}_{j+1/2} = \mathbf{b}(\mathbf{W}_{+1/2})$ , with  $\mathbf{W}_{+1/2}$  representing the numerical interface value of  $\mathbf{w}$ . Moreover, the interface value is already available if a Roe type flux is used.

### Wave propagation method for balance laws

Another unsplitted method is given in [2] and [28]. This is a simple extension of the *wave-propagation* method to balance laws. Considering a uniform grid, the idea is to replace the source term  $\psi(\mathbf{w}, x)$  by a function  $\Psi(\mathbf{w}, x)$  that is a sum of delta-function sources at the interface points,

$$\Psi(\mathbf{w}, x) = \Delta x \sum_i \Psi_{j+1/2} \delta(x - x_{j+1/2}). \quad (4.9)$$

Considering now the interface Riemann problem, the presence of the delta function source at  $x_{j+1/2}$  produces the following jump in the flux:

$$\mathbf{f}(\mathbf{W}_{j+1/2}^r) - \mathbf{f}(\mathbf{W}_{j+1/2}^l) = \Delta x \Psi_{j+1/2}. \quad (4.10)$$

The cell averages evolve according to

$$\frac{d}{dt} \mathbf{W}_j = -\frac{1}{\Delta x} (\mathbf{F}_{j+1/2}^l - \mathbf{F}_{j-1/2}^r), \quad (4.11)$$

where the  $l$  and  $r$  superscripts stand for the left and right of the interface, since now the flux is discontinuous. The computation of the numerical fluxes is based on the following decomposition

$$\mathbf{f}(\mathbf{W}_{j+1}) - \mathbf{f}(\mathbf{W}_j) - \Delta x \Psi_{j+1/2} = \sum_p \mathcal{Z}_{j+1/2}^p. \quad (4.12)$$

If a Roe type solver is used, the  $p$ -th wave is proportional to the  $p$ -th eigenvector of the approximate Jacobian,  $\mathcal{Z}_{j+1/2}^p = \beta_{j+1/2}^p \mathbf{r}_{j+1/2}^p$ . As pointed out by the authors themselves, the method can be advantageous for quasi-steady problems, since the forementioned waves describe only the information propagating relative to the background steady state solution.

## Splitting methods

The idea behind *splitting* or *fractional step* methods is to alternate between solving the associated hyperbolic homogeneous problem:

$$\frac{\partial}{\partial t} \mathbf{w} + \frac{\partial}{\partial x} \mathbf{f}(\mathbf{w}, x) = 0 \quad (4.13)$$

and the associated ODE:

$$\frac{d}{dt} \mathbf{w} = \psi(\mathbf{w}, x). \quad (4.14)$$

The procedure allows us to use standard methods for (4.13) without any modification, coupling it with a classical numerical tool for ODE, like Runge-Kutta or predictor-corrector methods. In the *Godunov splitting*, the time advance consists in solving (4.13) over a time step  $\Delta t$  and using the result to solve (4.14) over  $\Delta t$  again. This method is formally first order accurate [28]. In the *Strang splitting* method, the time advance is based on solving (4.13) over a time step  $\Delta t/2$ , then (4.14) is solved on a full step  $\Delta t$  and a final  $\Delta t/2$  step is taken again on (4.13). If appropriate solvers for the two subproblems are chosen, then second order accuracy is gained.

As mentioned above, we are interested in finding a steady state solution. The steady state results from a balance between two dynamic processes, associated to advection (flux term) and production (source term), that are handled separately in a fractional-step method. In some cases, the numerical balance could fail and the numerical solution may not converge, oscillating in time near the correct solution. That is, the splitting procedure may lead to schemes that are not well balanced [14]. Whether fractional-step methods can be used to successfully compute steady-state is rather problem-dependent, but it is also related to the choice of the numerical schemes involved in solving (4.13) and (4.14).

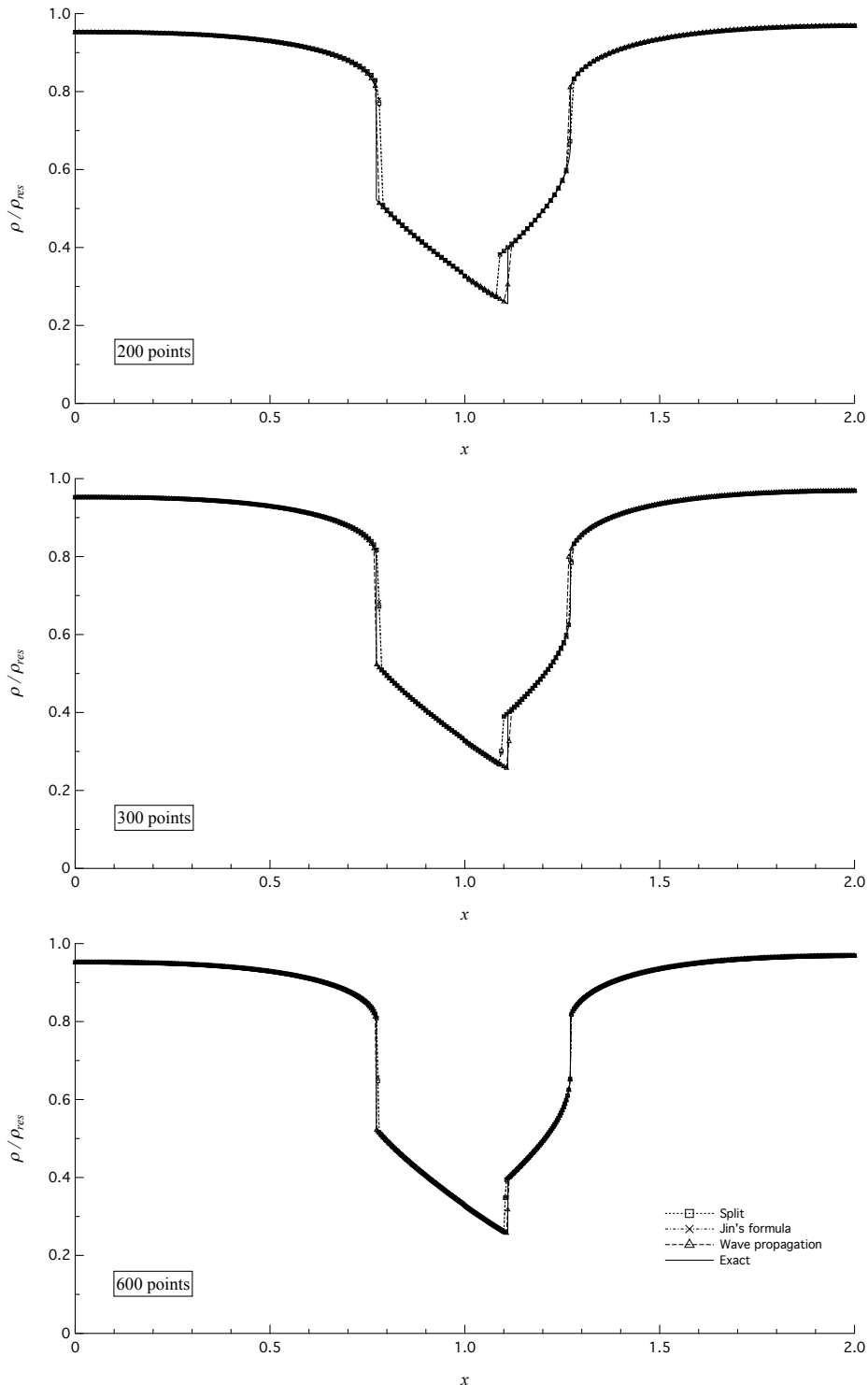


Figure 4.1: Formulation (4.3): comparison between different numerical methods, on case  $\mathcal{R}_{N^{2+}}^{[4-5]}$ , for 200, 300, 600 cells on a uniform grid.

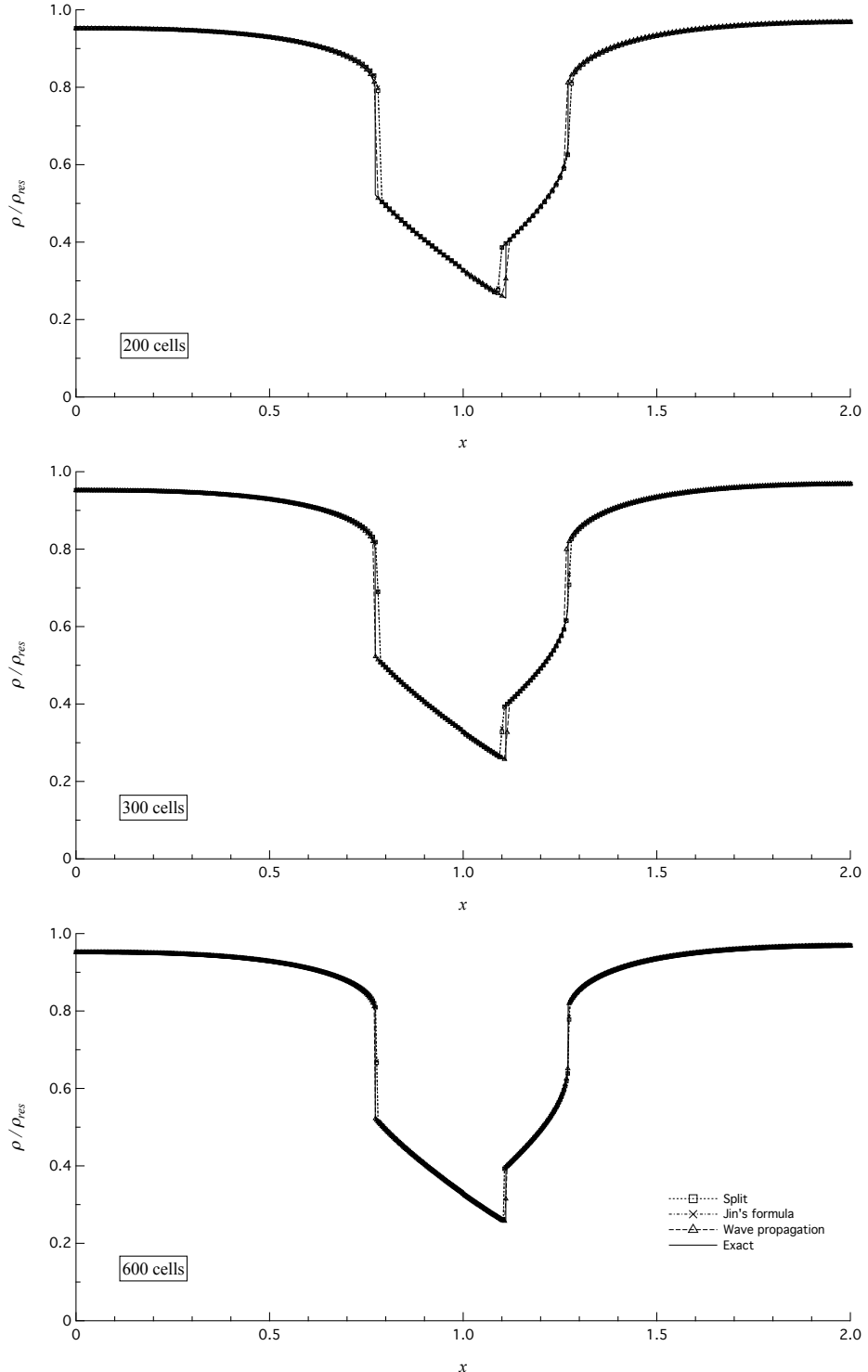


Figure 4.2: Formulation (4.4): comparison between different numerical methods, on case  $\mathcal{R}_{\mathcal{N}^{2+}}^{[4-5]}$ , for 200, 300, 600 cells on a uniform grid.

## 4.3 Numerical results

In the present section a brief comparison between the forementioned numerical methods is first performed, considering also the two different formulations introduced, Eqs. (4.3) and (4.4). Then a single method is chosen to compare its results with some of the exact solutions patterns obtained in the previous chapter.

The time advance is based on simple explicit methods, like the forward Euler for first order methods and the second order TVD Runge-Kutta (RK2) for second order methods. Some stability issue is likely to arise if the source term is stiff, which however is not the case here. For instance, in fractional step methods, solving (4.14) may require smaller time steps, compared to (4.13). In principle, given that we are interested in the steady state solutions, the order of time discretization is not important and the time-marching method may be the simple forward Euler even for second order (in space) method. However, for the second order scheme, the RK2 method has been implemented, due to its better stability region. This is confirmed by simulations with the Strang splitting scheme. We report that, in general, reaching a steady state condition with the forward Euler time advance requires a smaller CFL number or a smaller  $\Delta t$  for (4.14), with respect to RK2.

For the hyperbolic part of the balance law a numerical flux is to be chosen. The present method has been based on a Roe type flux [28, 38]. In particular, the linearization proposed by Guardone and Vigevano [16] has been implemented, resulting in sharper shock profiles with respect to the simple algebraic mean.

### 4.3.1 Comparison of the different methods

An exact solution is selected to perform a comparison between the different methods. We have chosen case  $\mathcal{R}_{\mathcal{N}^{2+}}^{[4-5]}$ , since it is a rather complex solution, including three discontinuities, namely a pre-sonic rarefaction shock and a shock-splitting configuration. For the two proposed formulations, (4.3) and (4.4), Figs. 4.1 and 4.2 respectively show a comparison between the split method, Jin's formula and the wave propagation algorithm for increasing number of grid cells, on a uniform grid. The stopping criteria is given by the 2-norm of the difference between the balance quantities  $\mathbf{w}$  in two consecutive time steps, normalized by a reference residual. All numerical solutions converged to a steady state. For the present case the split method is not affected by the balancing problems mentioned in the previous section. We can observe no significant differences between the two formulations. The same was observed for the computation of other solutions. Moreover, the split method and Jin's formula perform almost identically. With relatively few grid points, the wave propagation algorithm seems to work much better than the other methods. This is probably due to its intrinsic feature to deal with information propagating relative to a background steady state solution. With few grid points, for the split method and Jin's formula, we observe a small error in the evaluation of the shocks locations. This is related to their difficulties in approximating the correct entropy value in the central isentropic branch.

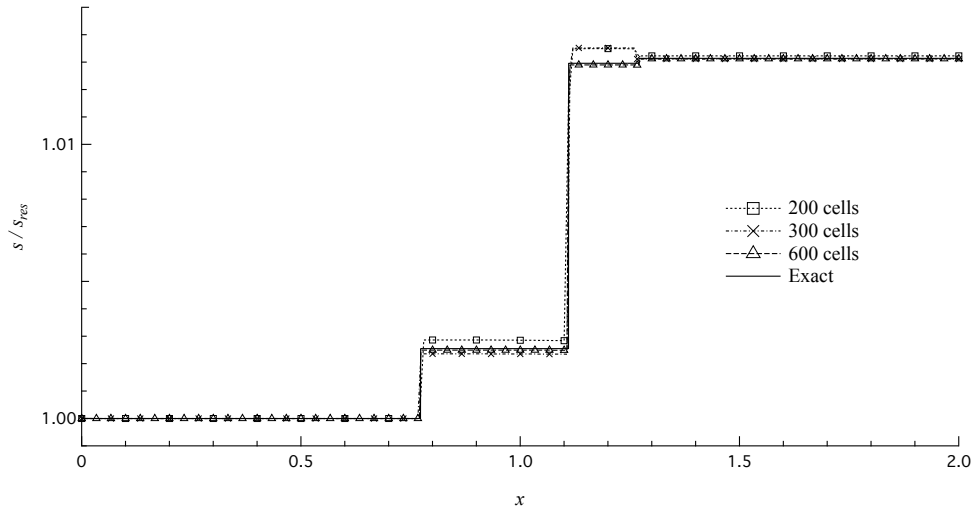


Figure 4.3: Entropy evolution for case  $\mathcal{R}_{N^{2+}}^{[4-5]}$ , with 200, 300, 600 cells on a uniform grid, obtained from the wave propagation method.

It is well-known [29, 28] that Roe-type fluxes need some fix for transonic waves in the interface Riemann problem. In the split method and in Jin's formula the flux term and the source term are handled separately, so that one of the classical entropy fix can be used for transonic waves. Here we have used the Harten and Hyman entropy fix [18, 33]. However, there is a major concern regarding the wave propagation scheme. The idea of splitting the flux difference and the source term as a single entity makes it difficult to perform an efficient fix for transonic waves. As reported by the authors of [2], proper handling of such sonic point is a critical task. Contrary to Jin's formula and to the split method, for the wave propagation scheme the results of Figs. 4.1 and 4.2 are computed without an entropy fix. Figure 4.3 shows the entropy evolution for the latter scheme. We can see that for relatively few grid points the third discontinuity is not entropy satisfying. Here as initial conditions we used a linear function between the inlet and outlet boundary conditions, but we report that different steady state solutions have been observed, starting from different initial conditions. This is again a negative consequence of the absence of an entropy fix. The resulting wave propagation algorithm works well near steady states, but it is not able to select the entropy satisfying steady state. Some sort of extension of the classical entropy fixes has been implemented, but with unsuccessful results.

#### 4.3.2 Comparison with exact solutions

This section presents the numerical results for some of the solutions of §3.5, obtained from a given numerical scheme. Previous discussion highlighted the main advantages and drawbacks of the proposed schemes. The two formulations are found to give equivalent numerical results. The wave propagation works well near steady states, but suffers from the lack of a successful cure for transonic

waves. On the contrary, the split method and Jin's formula are less accurate with few grid cells, but are not affected by entropic issues, since the usual entropy fixes can be simply applied. For this reason the numerical results shown below are produced from the Strang splitting method with formulation (4.4). Though not shown here, simulations using Jin's formula have been performed and are found to give very similar results. Figures 4.4, 4.5, 4.6 show first order results, computed on a uniform grid with 600 cells, for some of the most peculiar functioning regimes in nozzle flows of BZT fluids. A good agreement between numerical and exact solutions is observed. We note some difficulties of first order methods in approximating the correct entropy value in the central isentropic branches of the solutions. The most evident of such a situation is case  $\mathcal{R}_{\mathcal{N}^{2+}}^{[3-4]}$ , in which the entropy error downstream of the first shock causes a quite relevant error in the shock location. Figure 4.7 shows the limiting solutions distinguishing  $\mathcal{R}_{\mathcal{N}^{1+}}$  and  $\mathcal{R}_{\mathcal{N}^{2+}}$  functioning regimes from  $\mathcal{R}_{\mathcal{N}^{1-}}$  and  $\mathcal{R}_{\mathcal{N}^{2-}}$  respectively, confirming the differences mentioned in the previous chapter. Computation of limiting solutions is actually a quite subtle task, since these solutions are inherently unstable. A small perturbation causes a change from the desired limiting solution to an intermediate one, which is also different according to the sign of the perturbation.

Extension to second order is performed through a flux limiter scheme. Second order results are shown in Figs. 4.8, 4.9 and 4.10, again on a uniform grid with 600 cells. As expected, there is a significant improvement with respect to first order results. However, convergence problems were often encountered. For instance, almost all of the second order  $\mathcal{R}_{\mathcal{N}^{1+}}$  solutions do not converge, but oscillate around the correct steady state solutions. A possible candidate for this kind of problems is non-balancing. Fractional step methods, in general, are not steady state preserving. However, we report the same problems with Jin's formula, which should not suffer from balancing issues. A remark about the latter method is that it preserves steady states for smooth solutions. Then, its well-balancing is not guaranteed for shocked flows. We indeed report that, when such residual oscillations arise, most of the oscillation is related to cells including discontinuities.

We also report low frequency oscillations which we believe are due to slowly moving shocks, which are often encountered close to steady states. In some of the simulation we performed steady state was not reached due to recognizable waves that are continuously produced near some shock discontinuity. As reported by many authors [1, 21, 20], slowly moving shocks often cause the presence of post-shock oscillations. In our context, getting closer to the steady state solution implies that any discontinuities slow down. If post-shock oscillations arise, they are likely to prevent the numerical solution to reach a steady state condition. This phenomenon does not depend on the order of the space discretization, and could arise with both first and second order schemes. Usually first order methods are dissipative enough to adequately damp these oscillations and allow the solution to reach a steady state. These kind of oscillations have indeed been observed with second order methods, or with first order ones on a very fine grid. We haven't performed an extensive study on this phenomenon, since it is not

the purpose of the thesis. However, we observed this kind of oscillations only when some non-classical shocks, like rarefaction or sonic ones, are present in the solution. The causes of these residual oscillations are not clear. Moreover, we are not sure whether the two types of oscillations we have observed are of different nature, or are somehow related to a unique cause.

Simulations were also reported in which the two formulations proposed give very similar results, in terms of discrepancy with the exact solutions, but they behave quite different with respect to the mentioned residual oscillations. We have observed simulations in which only one of the two formulations results in successful convergence and vice versa.

We recall that the purpose of the present work is not to perform a deep investigation on numerical methods and their related behavior, the focus being on the exact solutions and on the features of non-ideal functioning regimes. Nevertheless, the comparison of the present section has revealed an excellent agreement between the exact and numerical solutions, providing a successful numerical assessment of the results of the exact computation procedure.

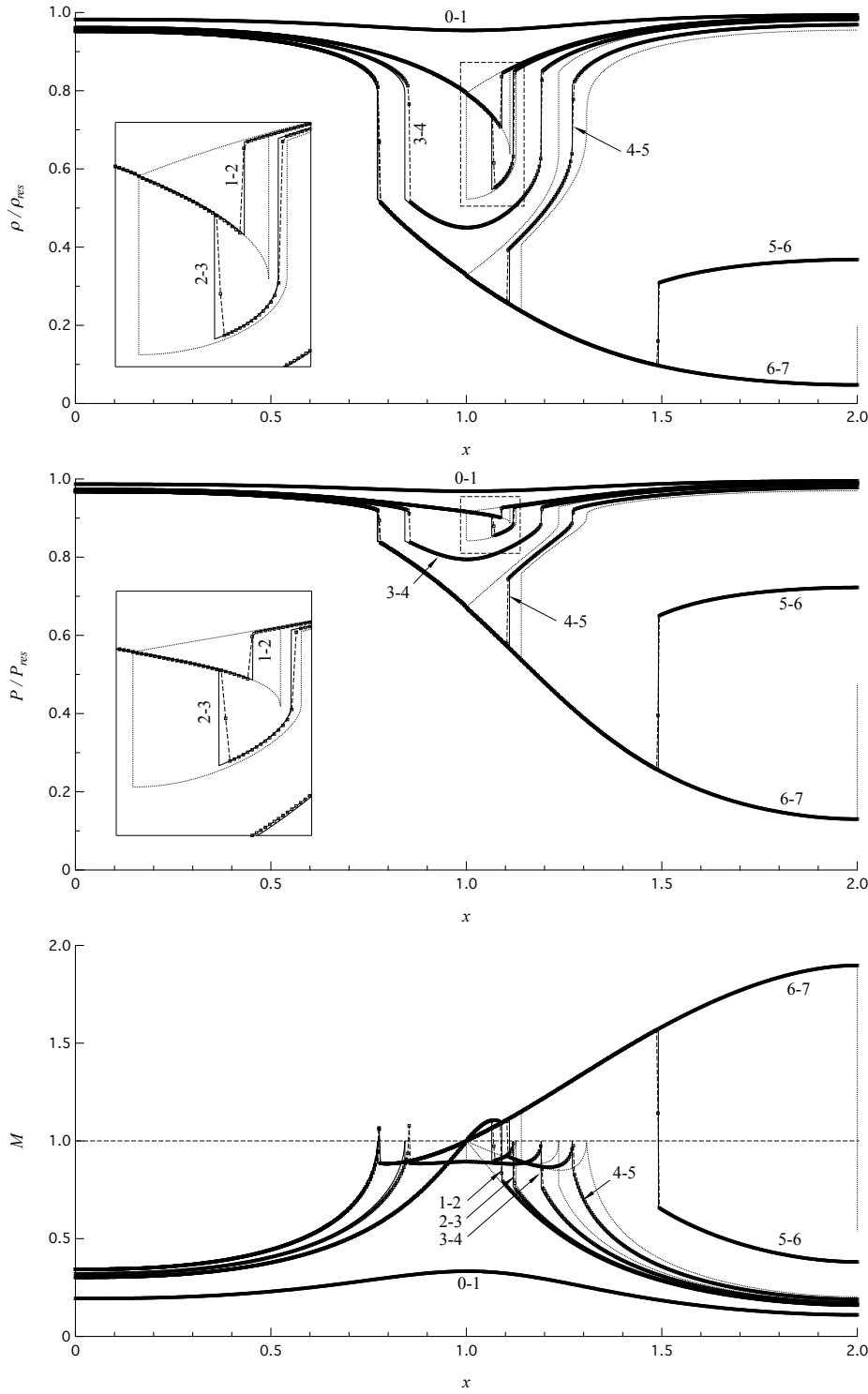


Figure 4.4: Numerical intermediate solutions (dashed-marked line), exact intermediate solutions (solid line) and exact limiting solutions (dashed line) for functioning regime  $\mathcal{R}_{N^{2+}}$ , computed from the polytropic van der Waals model with  $\delta = 1/50$ . The numerical solutions are computed on a uniform grid with 600 cells, by means of the first order split method based on formulation (4.4), the Roe solver of [16] and forward Euler time advance.

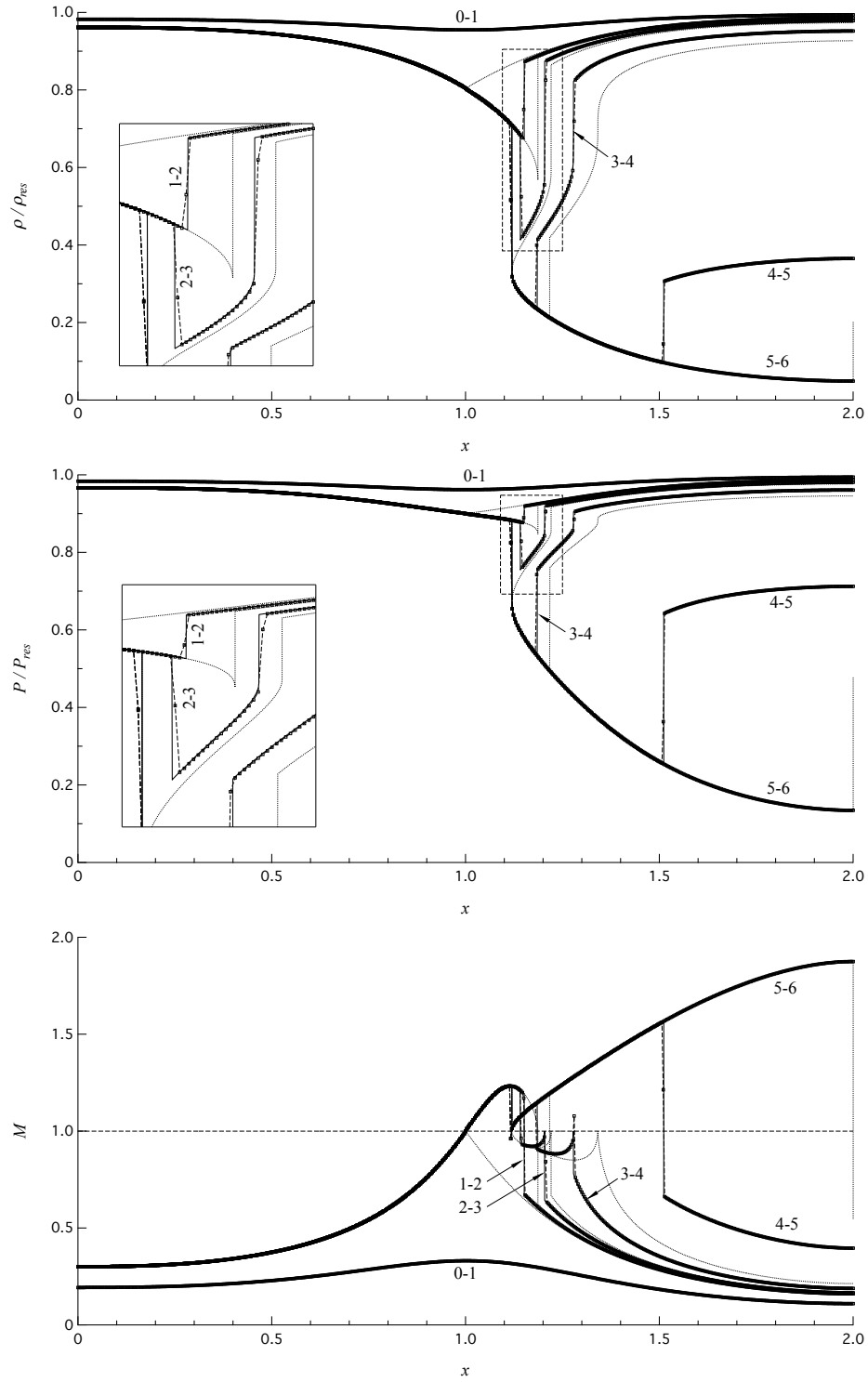


Figure 4.5: Numerical intermediate solutions (dashed-marked line), exact intermediate solutions (solid line) and exact limiting solutions (dashed line) for functioning regime  $\mathcal{R}_{N^{1+}}$ , computed from the polytropic van der Waals model with  $\delta = 1/50$ . The numerical solutions are computed on a uniform grid with 600 cells, by means of the first order split method based on formulation (4.4), the Roe solver of [16] and forward Euler time advance.

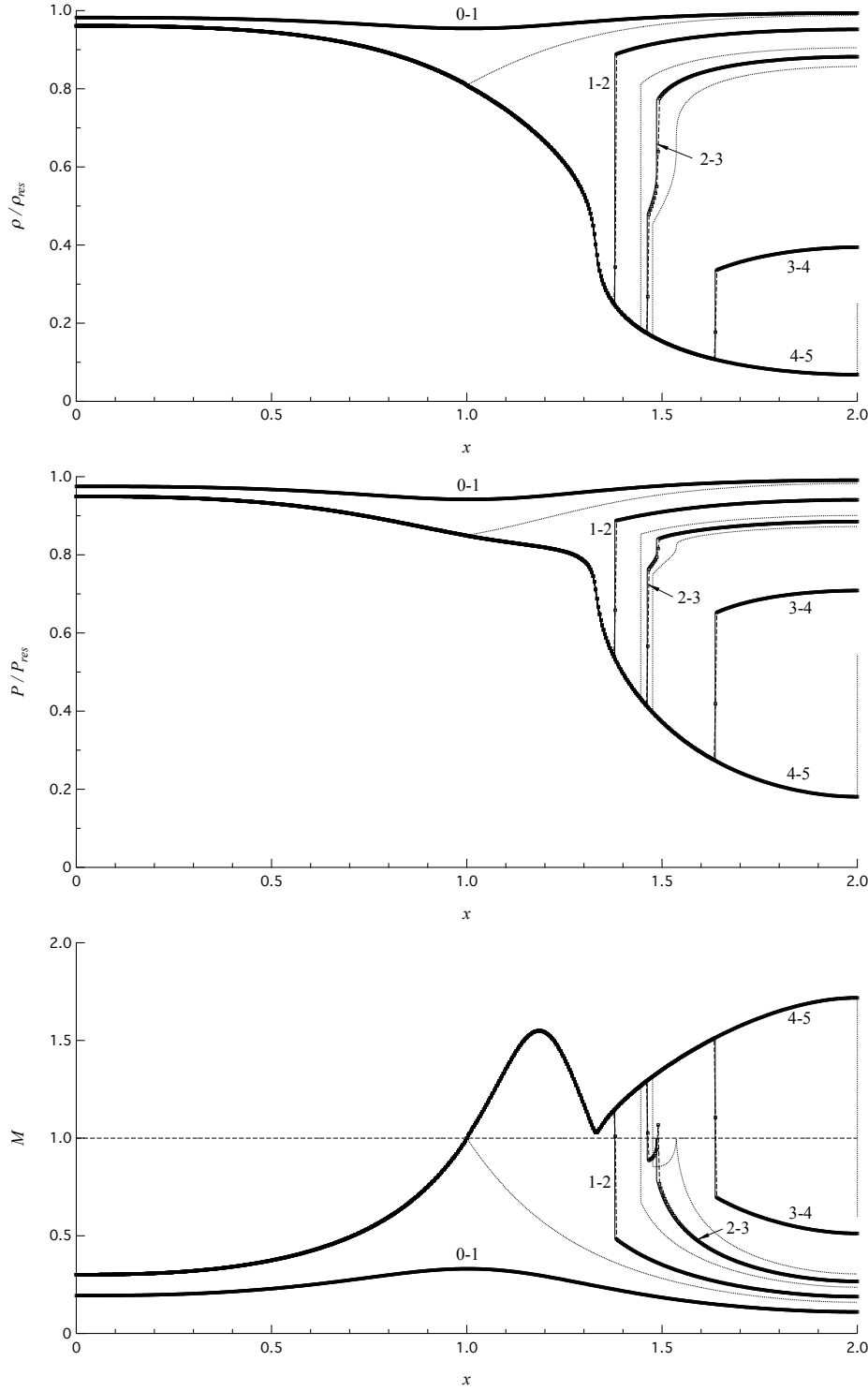


Figure 4.6: Numerical intermediate solutions (dashed-marked line), exact intermediate solutions (solid line) and exact limiting solutions (dashed line) for functioning regime  $\mathcal{R}_{N^3}$ , computed from the polytropic van der Waals model with  $\delta = 1/50$ . The numerical solutions are computed on a uniform grid with 600 cells, by means of the first order split method based on formulation (4.4), the Roe solver of [16] and forward Euler time advance.

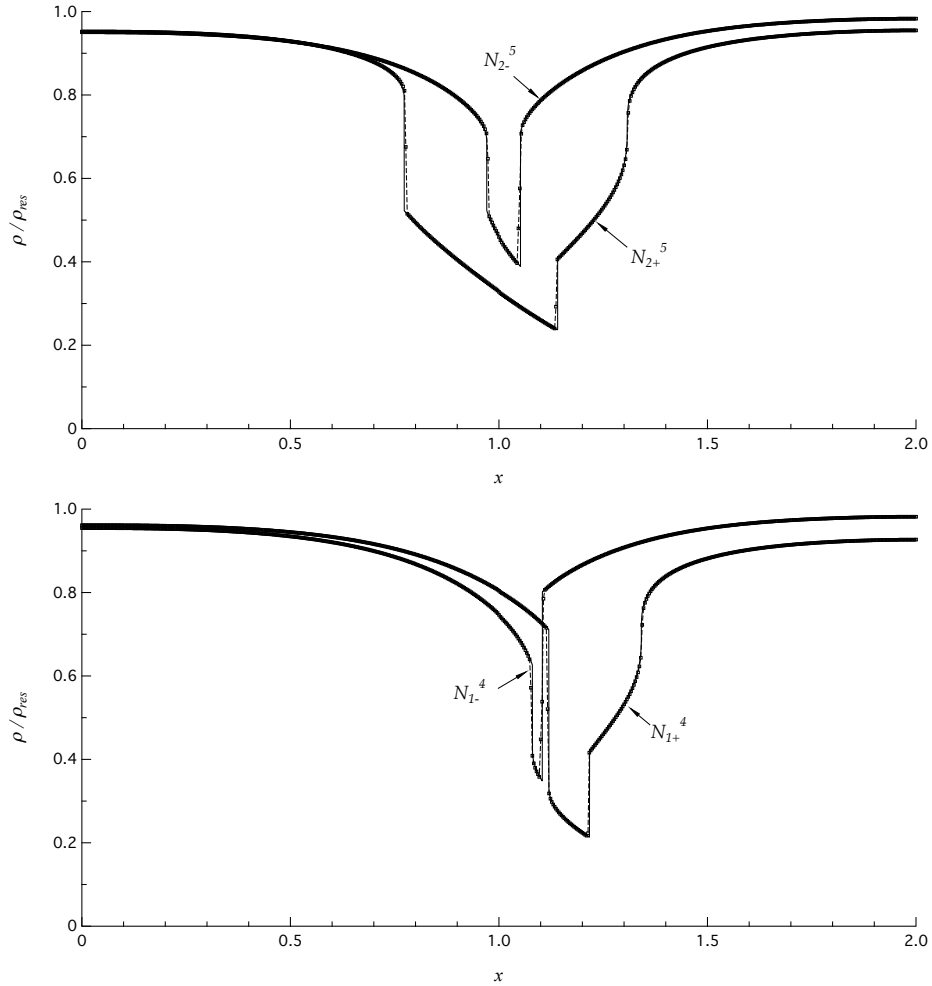


Figure 4.7: Numerical limiting solutions (dashed-marked line) and exact limiting solutions (solid line) of density for cases  $\mathcal{R}_{N_2^+}^{[5]}$  and  $\mathcal{R}_{N_2^-}^{[5]}$  above,  $\mathcal{R}_{N_1^+}^{[4]}$  and  $\mathcal{R}_{N_1^-}^{[4]}$  below. Solutions computed from the polytropic van der Waals model with  $\delta = 1/50$ . The numerical solutions are computed on a uniform grid with 600 cells, by means of the first order split method based on formulation (4.4), the Roe solver of [16] and forward Euler time advance.

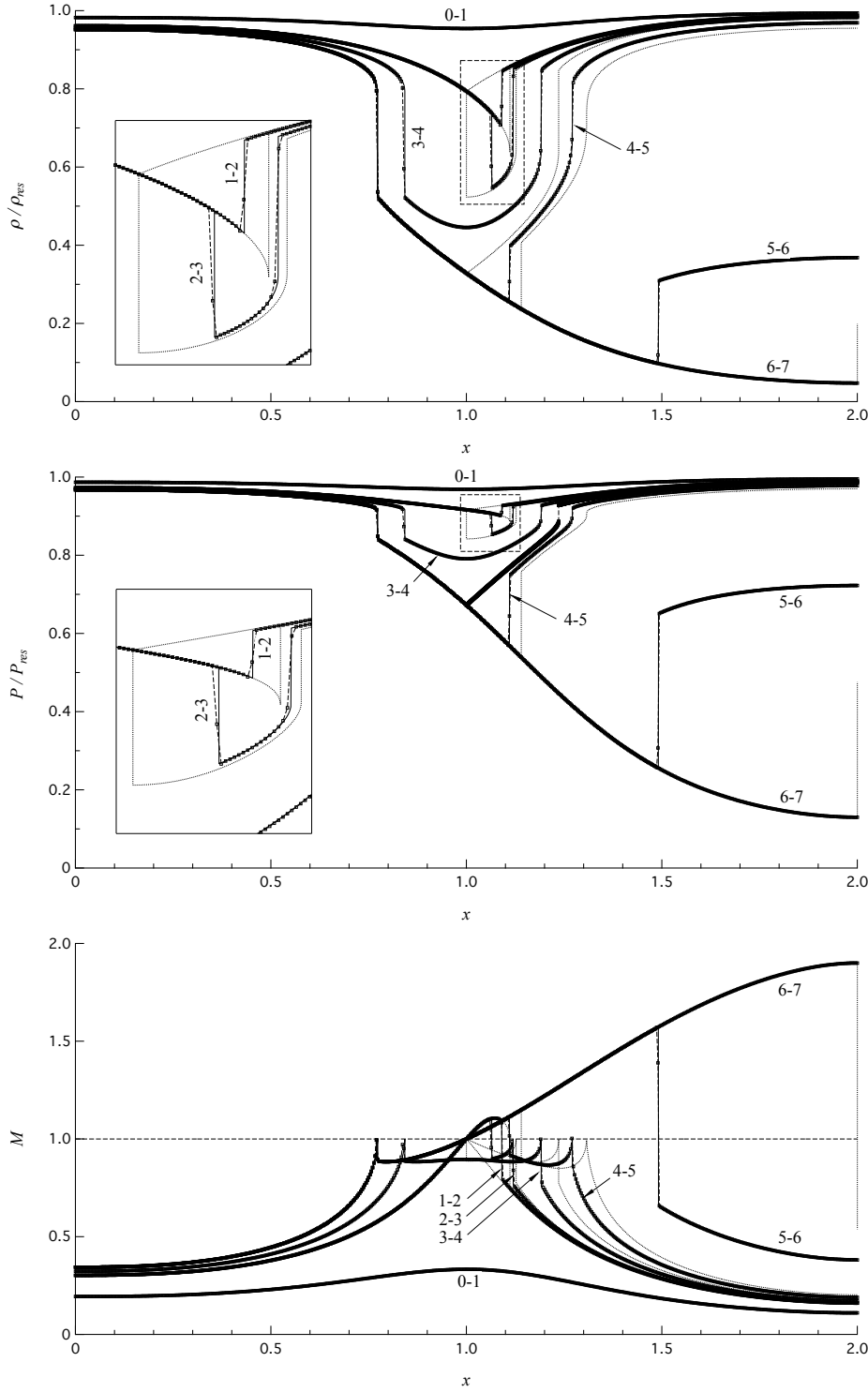


Figure 4.8: Numerical intermediate solutions (dashed-marked line), exact intermediate solutions (solid line) and exact limiting solutions (dashed line) for functioning regime  $\mathcal{R}_{N^{2+}}$ , computed from the polytropic van der Waals model with  $\delta = 1/50$ . The numerical solutions are computed on a uniform grid with 600 cells, by means of the second order split method based on formulation (4.4), the Roe solver of [16] with van Leer limiter and the second order TVD Runge-Kutta time advance.

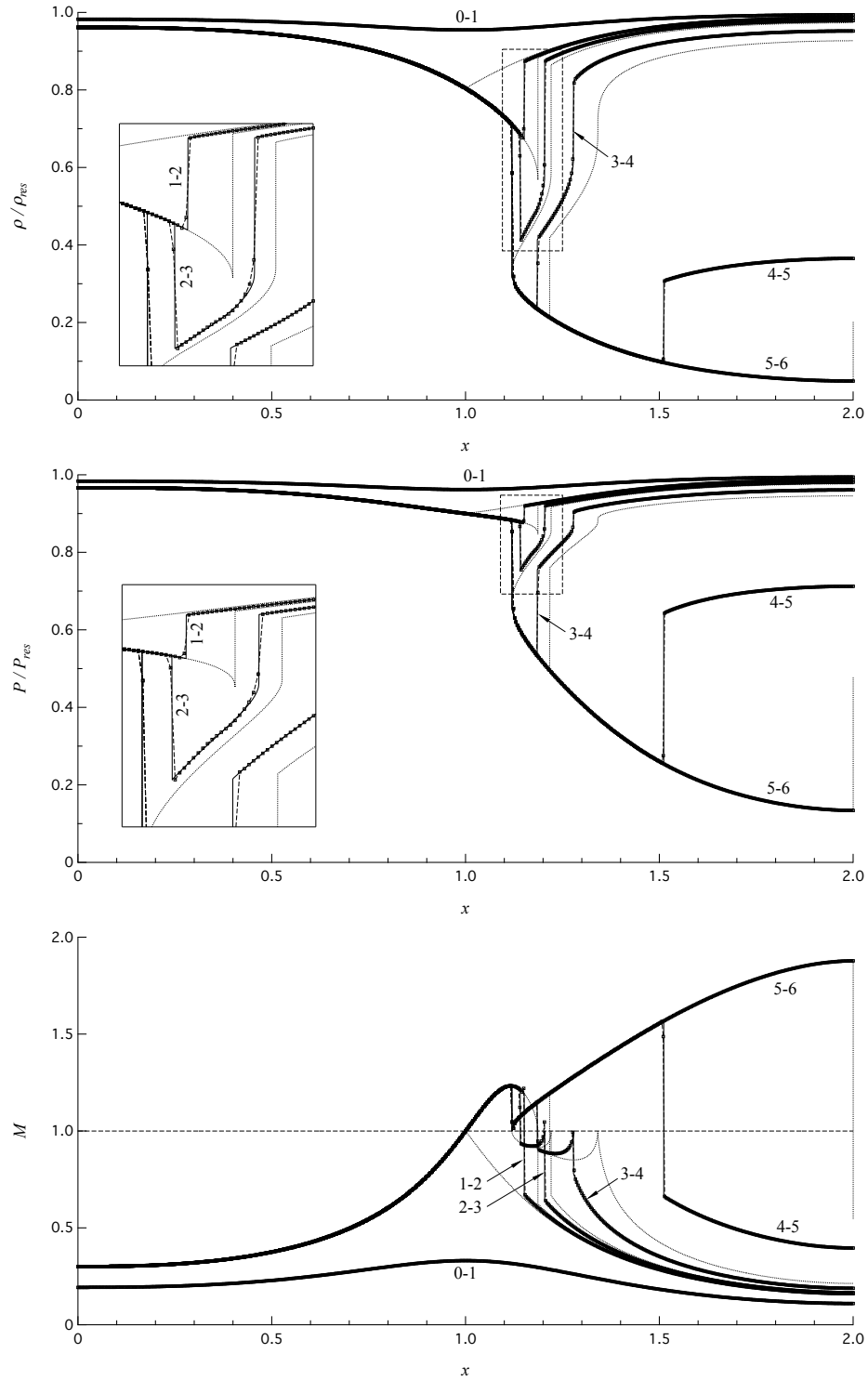


Figure 4.9: Numerical intermediate solutions (dashed-marked line), exact intermediate solutions (solid line) and exact limiting solutions (dashed line) for functioning regime  $\mathcal{R}_{N^{1+}}$ , computed from the polytropic van der Waals model with  $\delta = 1/50$ . The numerical solutions are computed on a uniform grid with 600 cells, by means of the second order split method based on formulation (4.4), the Roe solver of [16] with van Leer limiter and the second order TVD Runge-Kutta time advance.

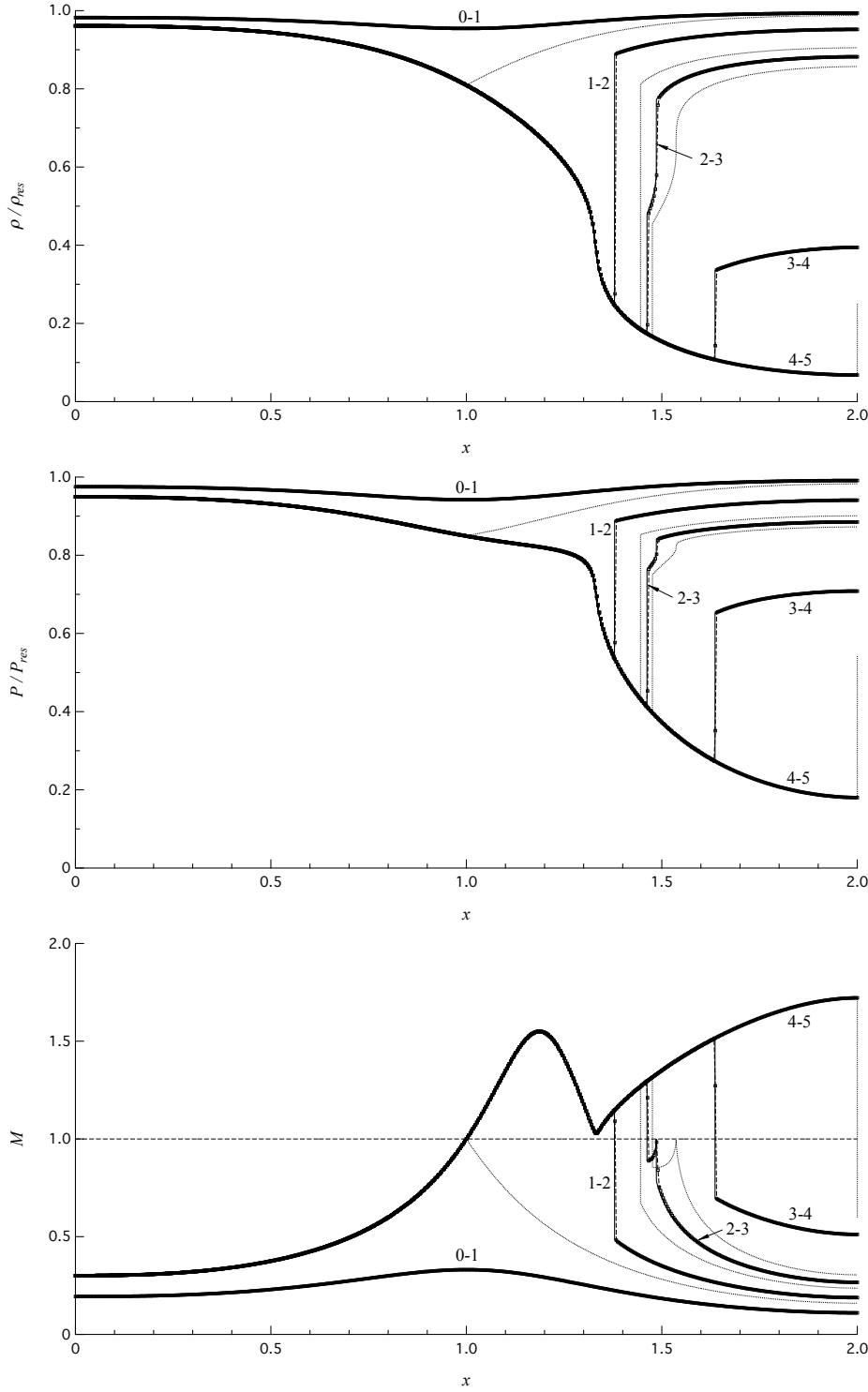


Figure 4.10: Numerical intermediate solutions (dashed-marked line), exact intermediate solutions (solid line) and exact limiting solutions (dashed line) for functioning regime  $\mathcal{R}_{N^3}$ , computed from the polytropic van der Waals model with  $\delta = 1/50$ . The numerical solutions are computed on a uniform grid with 600 cells, by means of the second order split method based on formulation (4.4), the Roe solver of [16] with van Leer limiter and the second order TVD Runge-Kutta time advance.



# Chapter 5

## Thermodynamic map of functioning regimes

The current section is devoted to the definition of the set of reservoir states leading to each functioning regime. We recall that the functioning regime is to be considered along with low subsonic inlet conditions and expansions to arbitrarily large Mach numbers, in order to fully appreciate the non-ideal features of BZT fluids, see §3.4.1. In so doing the nozzle geometry doesn't play any role except for the assumed convergent-divergent shape. Therefore it is possible to associate thermodynamic regions of reservoir conditions to the previously defined functioning regimes.

### 5.1 Transitional regimes

The thermodynamic map of functioning regimes, computed from the polytropic van der Waals model with  $c_v/R = 50$  is shown in Fig. 5.1 and Fig. 5.2, in the  $P$ - $v$  and  $T$ - $s$  planes respectively. The different regions in these diagrams represent the sets of stagnation states leading to each of the functioning regimes previously introduced. Due to the assumption of considering single phase flows, the thermodynamic regions are bounded by isentrope  $s = s_{\text{vle}}$ , tangent to the vapor dome. In order to compute the map, it is necessary to identify the curves related to transitional regimes. Their computation is now described.

#### Transition $\mathcal{R}_{\mathcal{I}}/\mathcal{R}_{\mathcal{M}-}$

Functioning regimes  $\mathcal{R}_{\mathcal{I}}$  and  $\mathcal{R}_{\mathcal{M}-}$  are both characterized by the presence of one sonic point only. The only difference is in the subsonic Mach number behavior. Inside of the nozzle no shock occurs in the limiting solutions, which therefore are also isentropic solutions (except for the exit shock of solutions  $\mathcal{R}_{\mathcal{I}}^{[2]}$  and  $\mathcal{R}_{\mathcal{M}-}^{[2]}$ ). The transition between these two regimes takes place when the isentropic pattern of reservoir conditions changes from  $\mathcal{S}_{\mathcal{I}}$  to  $\mathcal{S}_{\mathcal{M}-}$ . Indeed the line, in Fig. 5.1, which distinguish the current regimes coincides with the  $\mathcal{S}_{\mathcal{I}}/\mathcal{S}_{\mathcal{M}-}$  line in Fig. 2.12.

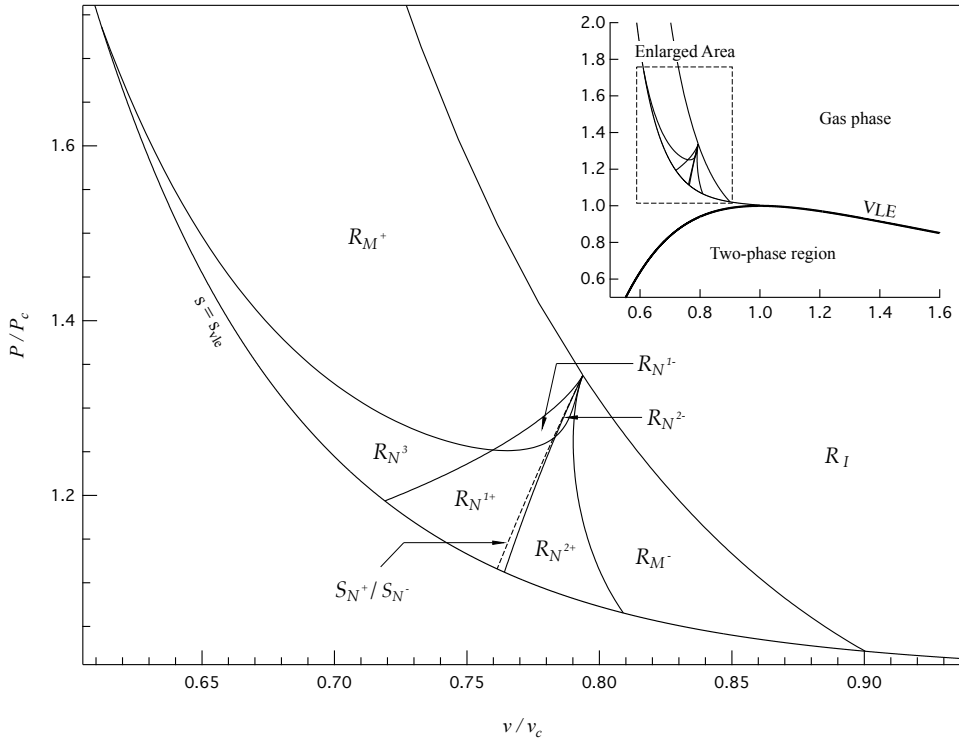


Figure 5.1:  $P$ - $v$  plane regions where reservoir couples lead to different functioning regimes. The curves are computed from the polytropic van der Waals model with  $\delta = 1/50$ .

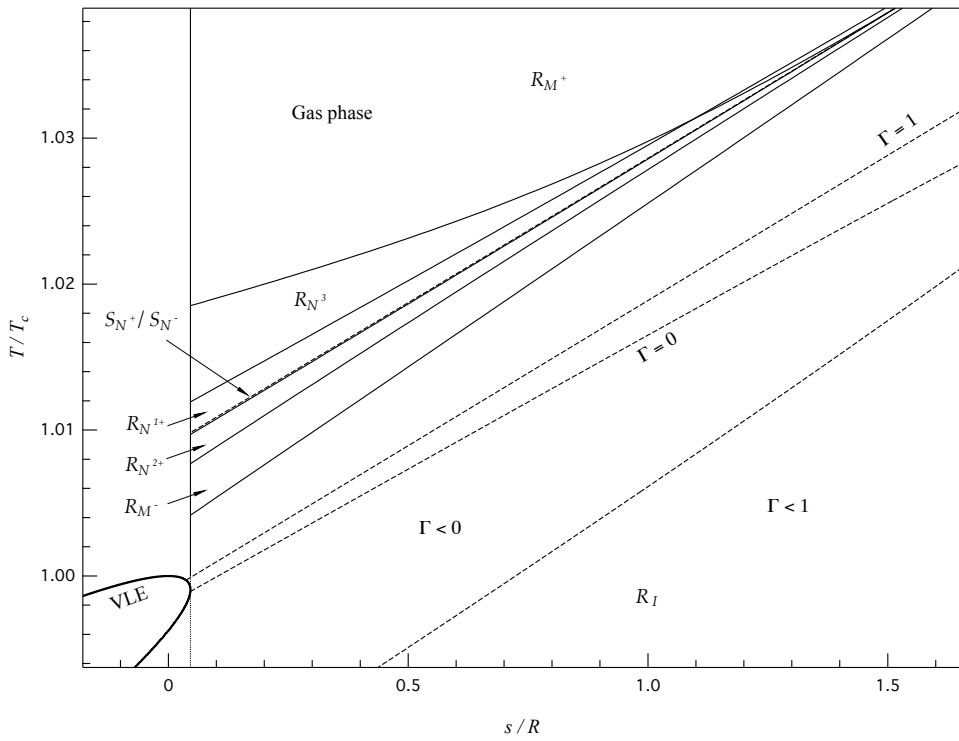


Figure 5.2:  $T$ - $s$  plane regions where reservoir couples lead to different functioning regimes. The curves are computed from the polytropic van der Waals model with  $\delta = 1/50$ .

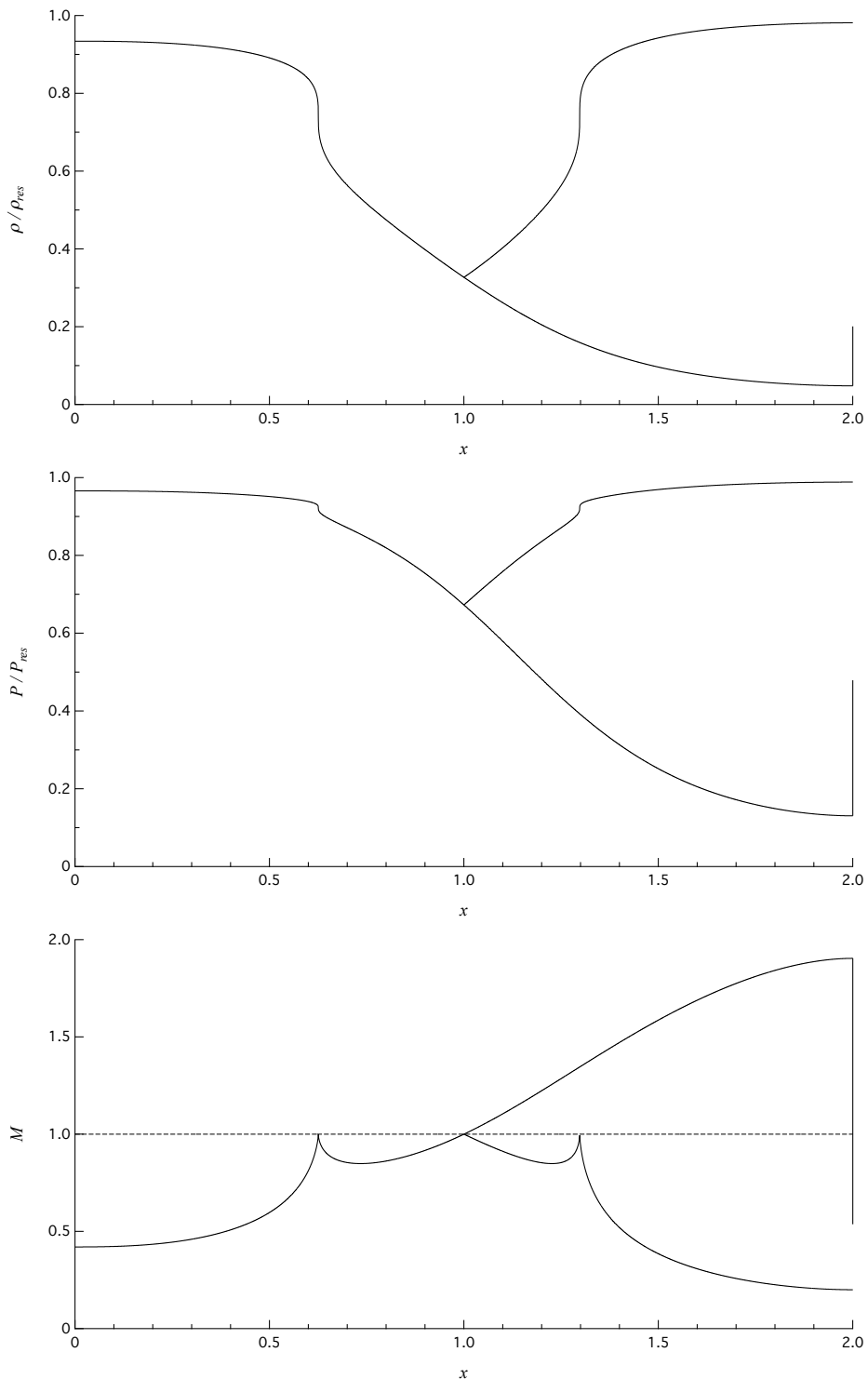


Figure 5.3: Limiting solutions for representative transitional regime  $\mathcal{R}_{\mathcal{M}-}/\mathcal{R}_{\mathcal{N}^{2+}}$ , computed from the polytropic van der Waals model with  $\delta = 1/50$ .

### Transition $\mathcal{R}_{\mathcal{M}^-}/\mathcal{R}_{\mathcal{N}^{2+}}$

Functioning regimes  $\mathcal{R}_{\mathcal{M}^-}$  and  $\mathcal{R}_{\mathcal{N}^{2+}}$  exhibit very different exact solutions layouts. The former, due to the non-monotone Mach number region, can be regarded as a slight variation of the standard nozzle flows of polytropic ideal gases. The latter is much more complex and shows several limiting solutions. In  $\mathcal{R}_{\mathcal{N}^{2+}}$ , in order to attain supersonic flow at the exhaust section, a rarefaction shock upstream of the throat section is required. A necessary condition for this occurrence is that the isentropic pattern of reservoir conditions exhibits three sonic points. The transitional case is the one in which stagnation conditions exhibit  $\mathcal{R}_{\mathcal{M}^-}/\mathcal{R}_{\mathcal{N}^-}$  pattern. Recalling §2.3.5, it is defined by the presence of two sonic points, a local maximum and a stationary inflection point. The latter, see Fig. 2.10, corresponds to a local maximum of the  $M(\rho)$  function, so that Mach number values in the neighborhood are subsonic. This leads to infinite slope points in subsonic portions of the limiting solutions, see Fig. 5.3. The features of these points have been discussed in the description of  $\mathcal{R}_{\mathcal{N}^{2+}}^{[5]}$ .

### Transition $\mathcal{R}_{\mathcal{N}^1}/\mathcal{R}_{\mathcal{N}^2}$

Transition between the  $\mathcal{R}_{\mathcal{N}^1}$  and  $\mathcal{R}_{\mathcal{N}^2}$  classes, i.e.  $\mathcal{R}_{\mathcal{N}^{1+}}/\mathcal{R}_{\mathcal{N}^{2+}}$  and  $\mathcal{R}_{\mathcal{N}^{1-}}/\mathcal{R}_{\mathcal{N}^{2-}}$  are now detailed. They are discussed in the same section since the current transition shows the same features for both of them. Previous discussion pointed out the main differences between  $\mathcal{R}_{\mathcal{N}^1}$  and  $\mathcal{R}_{\mathcal{N}^2}$  nozzle flows. These are the density value at throat for a choked flow and the location of the limiting rarefaction shock, which is in the divergent for  $\mathcal{R}_{\mathcal{N}^1}$  and in the convergent for  $\mathcal{R}_{\mathcal{N}^2}$ . The former is post-sonic, whereas the latter is pre-sonic. The transitional case is indeed the one which exhibits a double sonic shock exactly placed at throat. For a given total enthalpy, the unknown vector is the thermodynamic part of the pre- and post-shock states,  $(\rho_l, s_l, \rho_r, s_r)$ . The following system for a double sonic shock is to be solved,

$$\begin{cases} \rho_r c(s_r, \rho_r) = \rho_l c(s_l, \rho_l) \\ P(s_r, \rho_r) + \rho_r c^2(s_r, \rho_r) = P(s_l, \rho_l) + \rho_l c^2(s_l, \rho_l) \\ h(s_r, \rho_r) + \frac{1}{2} c^2(s_r, \rho_r) = h^t \\ h(s_l, \rho_l) + \frac{1}{2} c^2(s_l, \rho_l) = h^t. \end{cases} \quad (5.1)$$

Figures 5.4 and 5.5 show density, pressure and Mach number limiting solutions for transition  $\mathcal{R}_{\mathcal{N}^{1+}}/\mathcal{R}_{\mathcal{N}^{2+}}$  and  $\mathcal{R}_{\mathcal{N}^{1-}}/\mathcal{R}_{\mathcal{N}^{2-}}$ . In the latter limiting shocks are closer one to the other, since the reservoir entropy is higher and the interval of negative- $\Gamma$  values along the isentrope is smaller. The only qualitative difference is, as expected, in the limiting solution which defines the end of the shock-splitting configuration.

The transitional curve in Fig. 5.1 gathers the points from which, moving along the related isentrope, a double sonic shock is observed. As a further explanation, Fig. 5.6 shows the Double Sonic Locus (DSL), which identifies thermodynamic states that can be connected by a double sonic shock [40]. The Rarefaction Shock Region (RSR), which contains all the states that can possibly

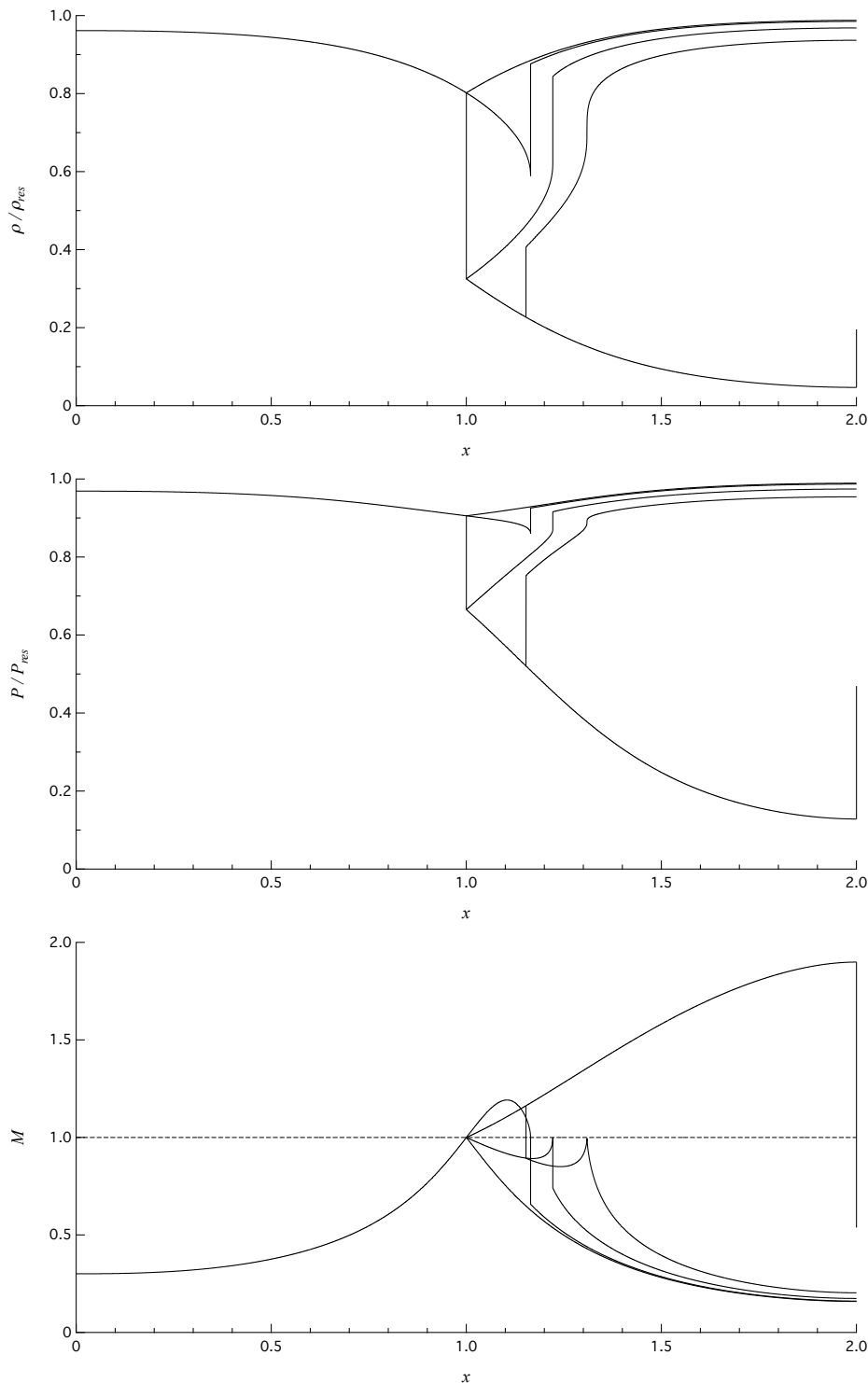


Figure 5.4: Limiting solutions for representative transitional regime  $\mathcal{R}_{\mathcal{N}^{1+}}/\mathcal{R}_{\mathcal{N}^{2+}}$ , computed from the polytropic van der Waals model with  $\delta = 1/50$ .

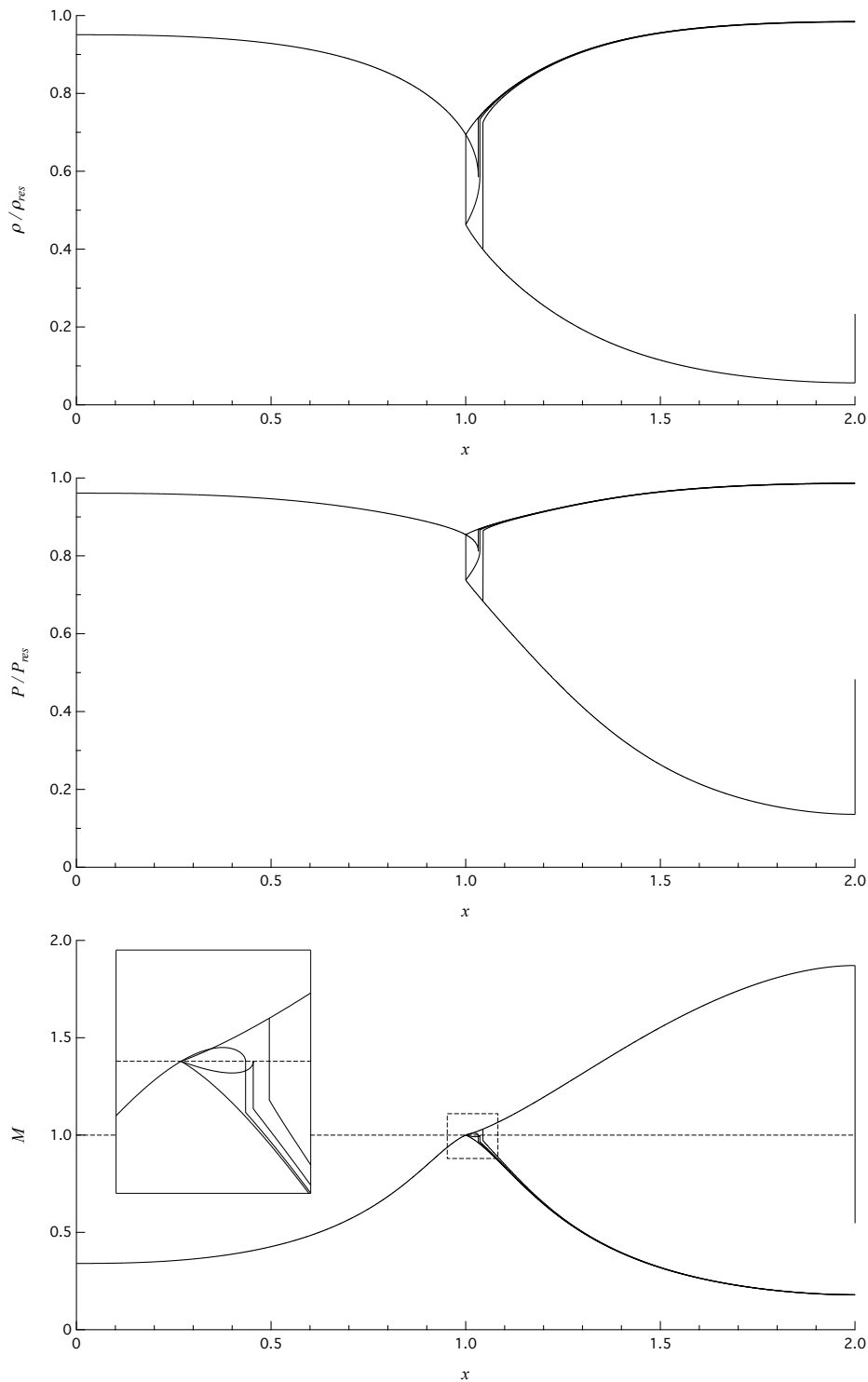


Figure 5.5: Limiting solutions for representative transitional regime  $\mathcal{R}_{\mathcal{N}^1-}/\mathcal{R}_{\mathcal{N}^2-}$ , computed from the polytropic van der Waals model with  $\delta = 1/50$ .

be connected by a rarefaction shock, is indeed bounded above by the DSL. The lower bound is represented by: a portion of the Limiting Rankine-Hugoniot curve, the one tangent to VLE, which is barely discernible from the isentrope tangent to the VLE; the saturation curve itself; the line representing post-sonic states of shock with pre-state lying on the saturation curve (PSV).

We can see from Fig. 5.1 that the transitional curve is located to the right of the  $\mathcal{S}_{\mathcal{N}^+}/\mathcal{S}_{\mathcal{N}^-}$  line, i.e. in the region of  $\mathcal{S}_{\mathcal{N}^-}$  reservoir conditions. Moreover,  $\mathcal{S}_{\mathcal{N}^+}$  reservoir conditions cannot lead to  $\mathcal{R}_{\mathcal{N}^2}$  functioning regimes. A proof of this claim is given also by alternative reasoning. Consider the shape of the flux function of  $\mathcal{S}_{\mathcal{N}^+}$  type. We are interested in the possible rarefaction shocks occurring from sonic point  $\rho_{s_1}$ . For  $\mathcal{S}_{\mathcal{N}^+}$  stagnation conditions this sonic point is the global maximum of the associated flux function. It has been previously shown that, as entropy increases across a shock, the flux function decreases, see Eq. (3.7). Therefore, given that in the  $f$ - $\rho$  plane a shock is represented by a horizontal segment, no rarefaction shock is possible from  $\rho_{s_1}$ , for  $\mathcal{S}_{\mathcal{N}^+}$  stagnation conditions. Conversely, in the  $\mathcal{S}_{\mathcal{N}^-}$  case, sonic point  $\rho_{s_1}$  is no longer the global maximum of the flux function. However, if the reservoir state is chosen between the  $\mathcal{S}_{\mathcal{N}^+}/\mathcal{S}_{\mathcal{N}^-}$  and  $\mathcal{R}_{\mathcal{N}^2}/\mathcal{R}_{\mathcal{N}^1}$  line, the resulting functioning regime is  $\mathcal{R}_{\mathcal{N}^1}$ . Consider to move along the reference isentrope, on the expansion branch, Fig. 5.7. The sonic density value  $\rho_{s_1}$  is assumed before entering the RSR, so that

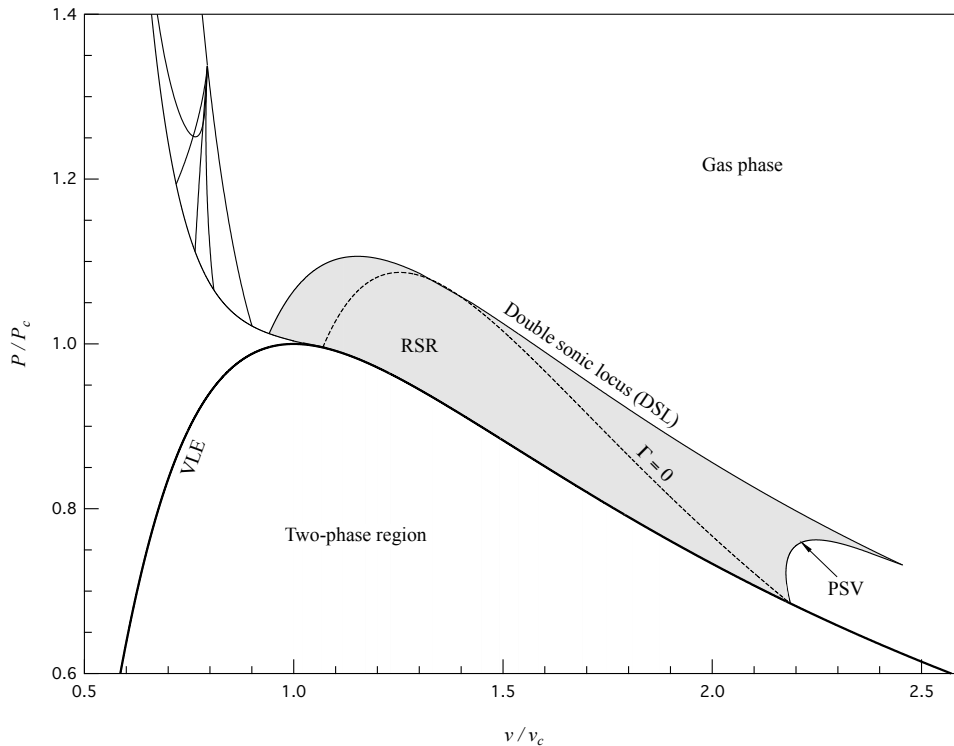


Figure 5.6: Rarefaction shock region computed from the polytropic van der Waals model with  $\delta = 1/50$ . The DSL line collects all the states which could be connected by a double sonic shock. The PSV line collects post-shock states of rarefaction shocks originating on the saturation curve.

no rarefaction shocks are admissible from this point. This leads to a limiting solutions layout similar to that of  $\mathcal{R}_{\mathcal{N}^1}$  regime. Moreover, the nozzle is choked with density value  $\rho_{s_1}$  at throat, despite this being an anomalous condition, since it is not the sonic density corresponding to the global maximum of the reservoir flux function.

### Transition $\mathcal{R}_{\mathcal{N}^+}/\mathcal{R}_{\mathcal{N}^-}$

The present section describes the conditions which define the transition between the  $\mathcal{R}_{\mathcal{N}^+}$  and  $\mathcal{R}_{\mathcal{N}^-}$  classes, i.e.  $\mathcal{R}_{\mathcal{N}^{2+}}/\mathcal{R}_{\mathcal{N}^{2-}}$  and  $\mathcal{R}_{\mathcal{N}^{1+}}/\mathcal{R}_{\mathcal{N}^{1-}}$ . As previously discussed, the difference lies in the limiting solution defining the end of the shock-splitting configuration. For '+' labeled regimes the portion of this solution consists of a compression shock with downstream isentropic pattern corresponding to transition  $\mathcal{S}_{\mathcal{N}^-}/\mathcal{S}_{\mathcal{M}^-}$ . Therefore, the final isentropic branch of the density or pressure exact solutions exhibits an infinite slope point. On the contrary, for '-' labeled regimes the end of the shock-splitting configuration is determined by a shock which is tangent to the *RH* curve in an intermediate sonic step. We recall that this shock could be regarded as the composition of two consecutive shocks, a post-sonic and a pre-sonic compression shock. Moreover, sonic points in compression shocks are admissible if they exhibit negative, null in the limit, fundamental derivative, see §2.4.2.

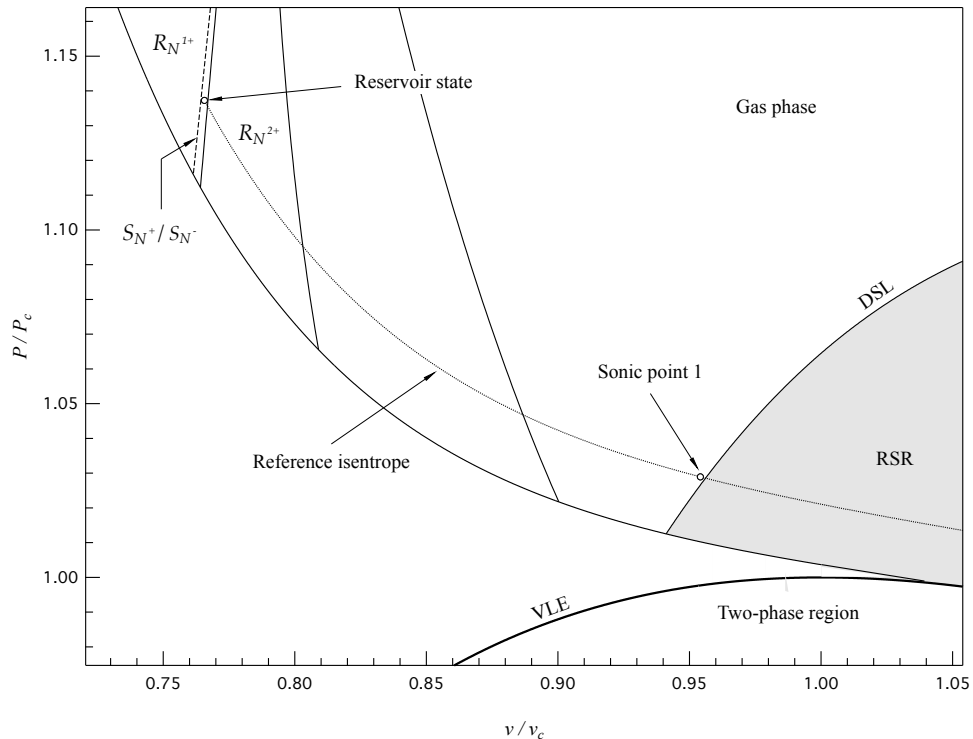


Figure 5.7: The stagnation state is located between the  $\mathcal{S}_{\mathcal{N}^+}/\mathcal{S}_{\mathcal{N}^-}$  and  $\mathcal{R}_{\mathcal{N}^2}/\mathcal{R}_{\mathcal{N}^1}$  line. Sonic conditions  $\rho = \rho_{s_1}$  occur before entering the RSR. Diagram computed from the polytropic van der Waals model with  $\delta = 1/50$ .

The limiting shock between  $\mathcal{R}_{\mathcal{N}^+}$  and  $\mathcal{R}_{\mathcal{N}^-}$  classes is indeed a compression shock exhibiting mixed features: the downstream isentropic pattern is  $\mathcal{S}_{\mathcal{N}^-}/\mathcal{S}_{\mathcal{M}^-}$  and the intermediate sonic step becomes coincident with the post-shock state, resulting in a post-sonic state with null fundamental derivative, see Fig. 5.8. This requires a shock which ends precisely on the stationary inflection point of the post-shock flux function of  $\mathcal{S}_{\mathcal{N}^-}/\mathcal{S}_{\mathcal{M}^-}$  type. For a given pre-shock entropy  $s_l$ , the system for the current shock is

$$\begin{cases} \rho_r c(s_r, \rho_r) = \rho_l M_l c(s_l, \rho_l) \\ P(s_r, \rho_r) + \rho_r c^2(s_r, \rho_r) = P(s_l, \rho_l) + \rho_l M_l^2 c^2(s_l, \rho_l) \\ h(s_r, \rho_r) + \frac{1}{2} c^2(s_r, \rho_r) = h(s_l, \rho_l) + \frac{1}{2} M_l^2 c^2(s_l, \rho_l) \\ \Gamma(s_r, \rho_r) = 0, \end{cases} \quad (5.2)$$

where the unknown vector is  $(\rho_l, \rho_r, M_l, s_r)$ . It has to be noted that the shock we are looking for occurs downstream of the limiting rarefaction shock. Then  $s_l$  is the entropy value downstream of this shock and not the reservoir value. The transitional curves  $\mathcal{R}_{\mathcal{N}^{2+}}/\mathcal{R}_{\mathcal{N}^{2-}}$  and  $\mathcal{R}_{\mathcal{N}^{1+}}/\mathcal{R}_{\mathcal{N}^{1-}}$  in Fig. 5.1 gathers the stagnation states from which a similar shock is observed. Figures 5.9 and 5.10 show the limiting solutions layout relative to the forementioned transitions. With respect to the limiting solution determining the end of the shock-splitting configuration, immediately downstream of the current limiting shock, the slope is infinite in the density and pressure solutions, due to the fact that the post-shock state is sonic.

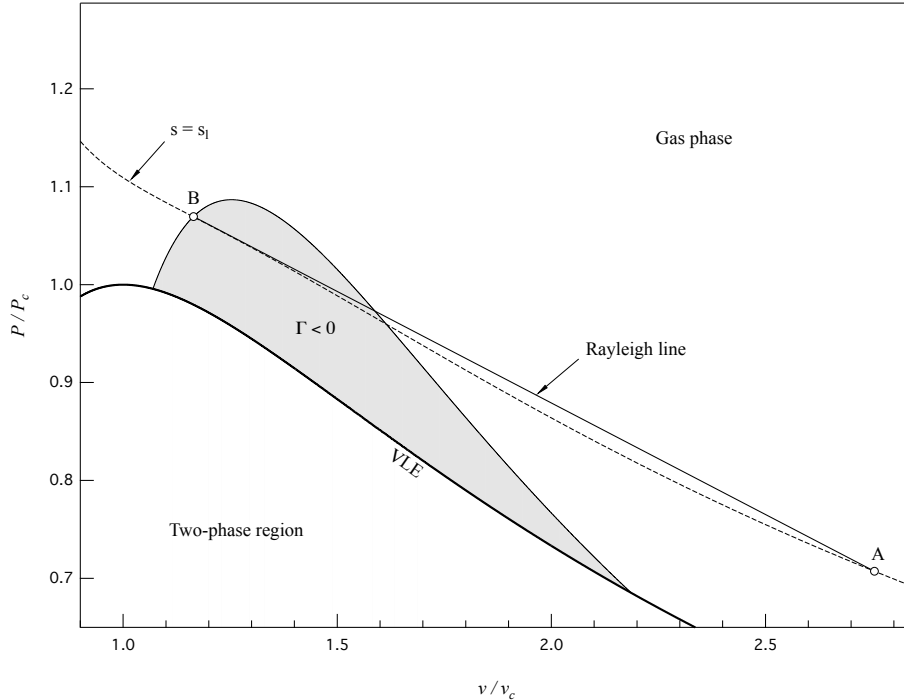


Figure 5.8: Post-sonic compression shock exhibiting  $\Gamma = 0$  at post-shock state, computed from a polytropic van der Waals model with  $\delta = 1/50$ .

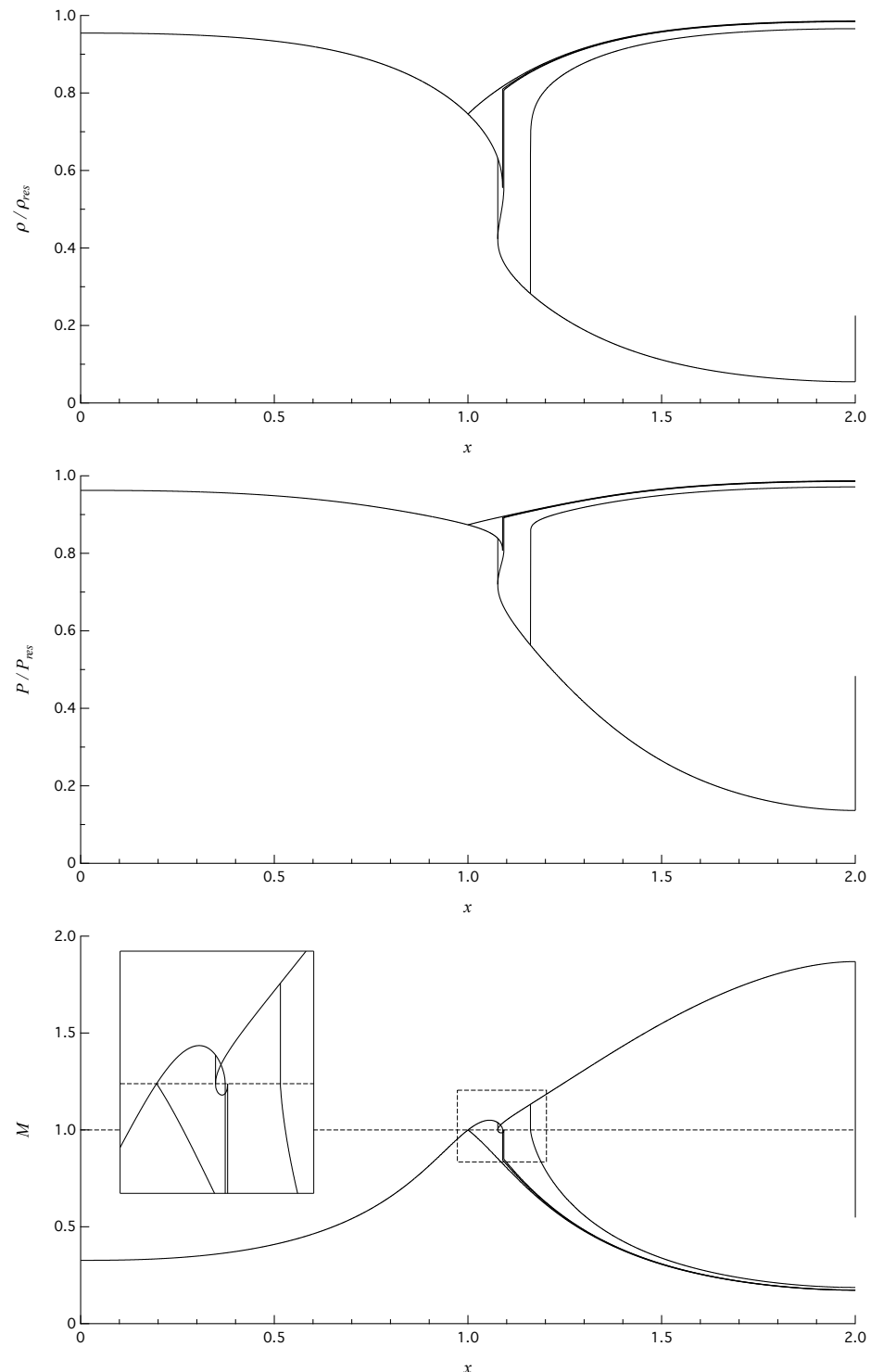


Figure 5.9: Limiting solutions for representative transitional regime  $\mathcal{R}_{\mathcal{N}^{1+}}/\mathcal{R}_{\mathcal{N}^{1-}}$ , computed from the polytropic van der Waals model with  $\delta = 1/50$ .

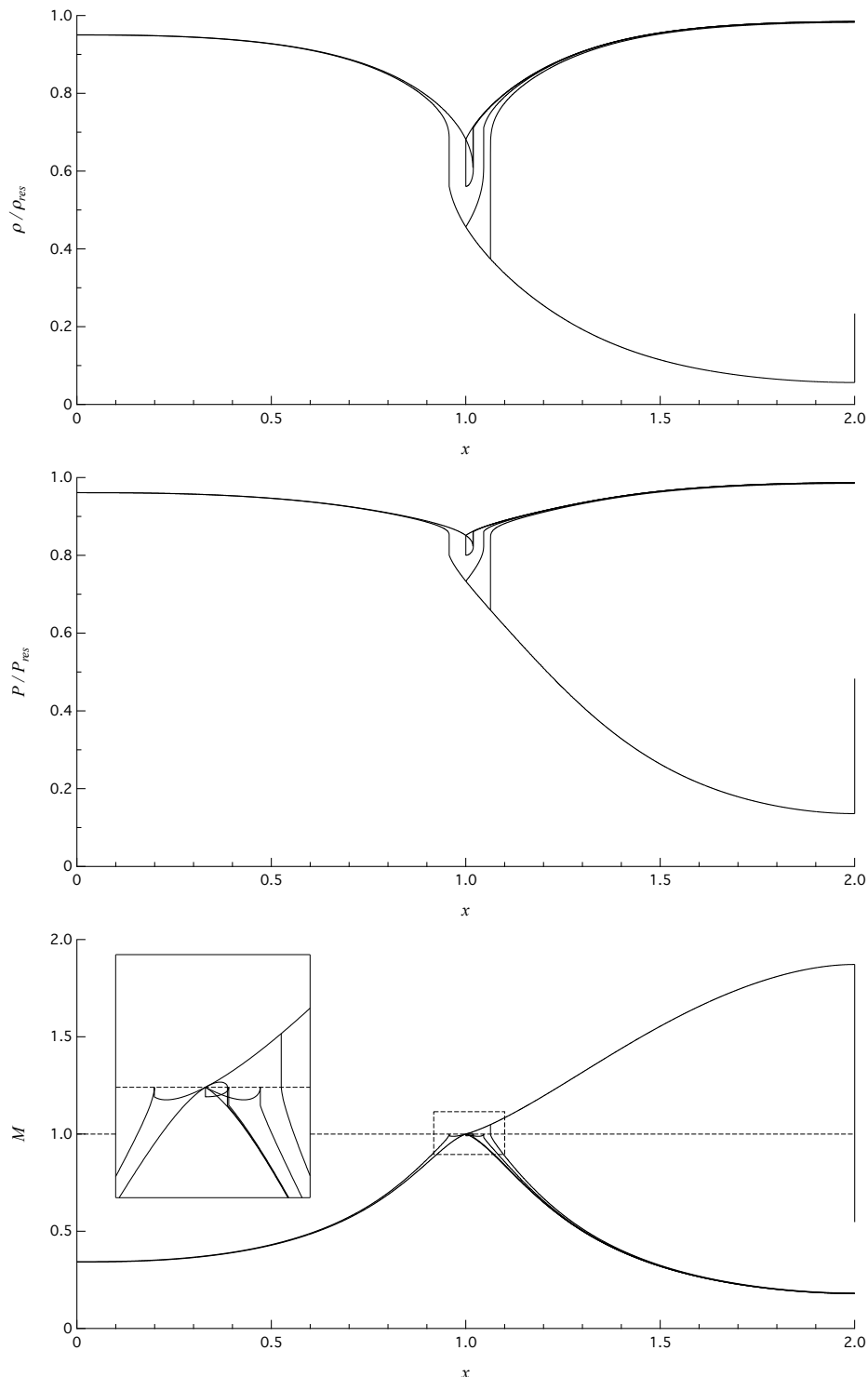


Figure 5.10: Limiting solutions for representative transitional regime  $\mathcal{R}_{N^{2+}}/\mathcal{R}_{N^{2-}}$ , computed from the polytropic van der Waals model with  $\delta = 1/50$ .

### Transitions $\mathcal{R}_{\mathcal{N}^{1+}}/\mathcal{R}_{\mathcal{N}^3}$ and $\mathcal{R}_{\mathcal{N}^{1-}}/\mathcal{R}_{\mathcal{M}^+}$

Transitions  $\mathcal{R}_{\mathcal{N}^{1+}}/\mathcal{R}_{\mathcal{N}^3}$  and  $\mathcal{R}_{\mathcal{N}^{1-}}/\mathcal{R}_{\mathcal{M}^+}$  are described in the same section since they are associated to the same occurrence, the transition from  $\mathcal{S}_{\mathcal{N}^+}$  to  $\mathcal{S}_{\mathcal{M}^+}$  isentropic pattern of reservoir conditions. Consider a  $\mathcal{S}_{\mathcal{N}^+}$  reservoir state. As the reservoir state moves closer to the  $\mathcal{S}_{\mathcal{N}^+}/\mathcal{S}_{\mathcal{M}^+}$  line in Fig. 2.12, the two sonic points for lower densities move closer to each other and in the limit of  $\mathcal{S}_{\mathcal{N}^+}/\mathcal{S}_{\mathcal{M}^+}$  pattern they overlap in a single sonic point, which exhibit null fundamental derivative, see §2.3.5. The latter is a stationary inflection point of the related flux function and it causes, see Figs. 5.12 and 5.13, the supersonic portions of the limiting solutions to show an infinite slope point. The only difference lies in the presence of a shock-splitting region in  $\mathcal{R}_{\mathcal{N}^{1+}}/\mathcal{R}_{\mathcal{N}^3}$  transitional regime. The main feature of  $\mathcal{R}_{\mathcal{N}^1}$  functioning regimes is the presence of a post-sonic rarefaction shock downstream of the throat section. If we consider reservoir states located on the same isenthalpic line, an increase of the reservoir density, i.e. getting closer to the  $\mathcal{S}_{\mathcal{N}^+}/\mathcal{S}_{\mathcal{M}^+}$  line, causes the limiting shock to become weaker and, in the limit, to have zero-intensity. Indeed, Fig. 5.11, shows that from the aforementioned sonic point with null fundamental derivative, no rarefaction shocks is admissible except the trivial one. As a matter of fact, no rarefaction shock wave can originate from states located on the right of the negative- $\Gamma$  region, because the rarefactive portion of the shock adiabat is always concave up for all possible pre-shock state [17]. These reasoning lead us to iden-

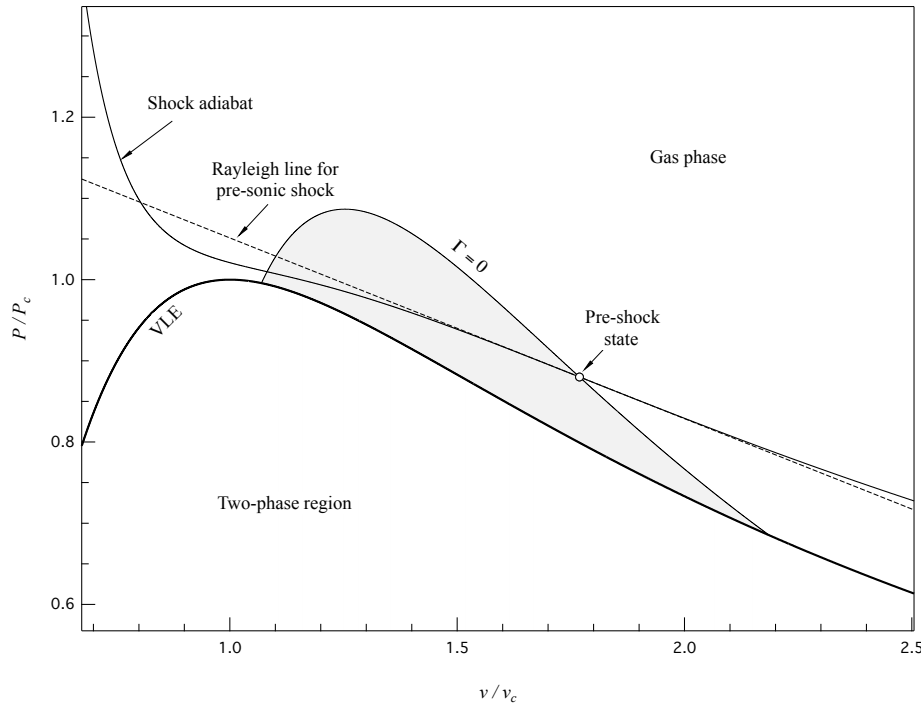


Figure 5.11: Shock adiabat through a point exhibiting null fundamental derivative, computed from the polytropic van der Waals model with  $\delta = 1/50$ . The Rayleigh line corresponds to a pre-sonic shock.

tify the  $\mathcal{R}_{\mathcal{N}^{1+}}/\mathcal{R}_{\mathcal{N}^3}$  and  $\mathcal{R}_{\mathcal{N}^{1-}}/\mathcal{R}_{\mathcal{M}^+}$  curves in Fig. 5.1 with the  $\mathcal{S}_{\mathcal{N}^+}/\mathcal{S}_{\mathcal{M}^+}$  line of Fig. 2.12.

### Transition $\mathcal{R}_{\mathcal{N}^3}/\mathcal{R}_{\mathcal{M}^+}$

The difference between  $\mathcal{R}_{\mathcal{M}^+}$  and  $\mathcal{R}_{\mathcal{N}^3}$  functioning regime lies in the presence of a shock-splitting region. The latter, observed in  $\mathcal{R}_{\mathcal{N}^3}$ , originates with a shock which is tangent to the shock adiabat in an intermediate sonic step, and runs out with a shock causing the downstream isentropic pattern to be  $\mathcal{S}_{\mathcal{N}^-}/\mathcal{S}_{\mathcal{M}^-}$ . Consider a given reservoir state exhibiting functioning regime  $\mathcal{R}_{\mathcal{N}^3}$ . If the reservoir density is increased at constant entropy, the shock-splitting region becomes smaller. For a particular reservoir value the two limiting solutions delimiting the shock-splitting region became coincident in a solution which presents a post-sonic compression shock with null post-shock fundamental derivative. The same situation has been described in distinguishing  $\mathcal{R}_{\mathcal{N}^+}$  and  $\mathcal{R}_{\mathcal{N}^-}$  functioning regimes. The separation curve  $\mathcal{R}_{\mathcal{M}^+}/\mathcal{R}_{\mathcal{N}^3}$  in Fig. 5.1 is indeed the continuation of the  $\mathcal{R}_{\mathcal{N}^{1+}}/\mathcal{R}_{\mathcal{N}^{1-}}$  curve.

### Transition $\mathcal{R}_{\mathcal{I}}/\mathcal{R}_{\mathcal{M}^+}$

The only difference between these two functioning regimes is the supersonic Mach number behavior. No shock occurs in the limiting solutions, which are therefore isentropic solutions. Transition  $\mathcal{R}_{\mathcal{I}}/\mathcal{R}_{\mathcal{M}^+}$  is associated to transition  $\mathcal{S}_{\mathcal{I}}/\mathcal{S}_{\mathcal{M}^+}$  between the isentropic patterns of reservoir conditions. The separating line in Fig. 5.1 indeed coincides with the  $\mathcal{S}_{\mathcal{I}}/\mathcal{S}_{\mathcal{M}^+}$  line of Fig. 2.12.

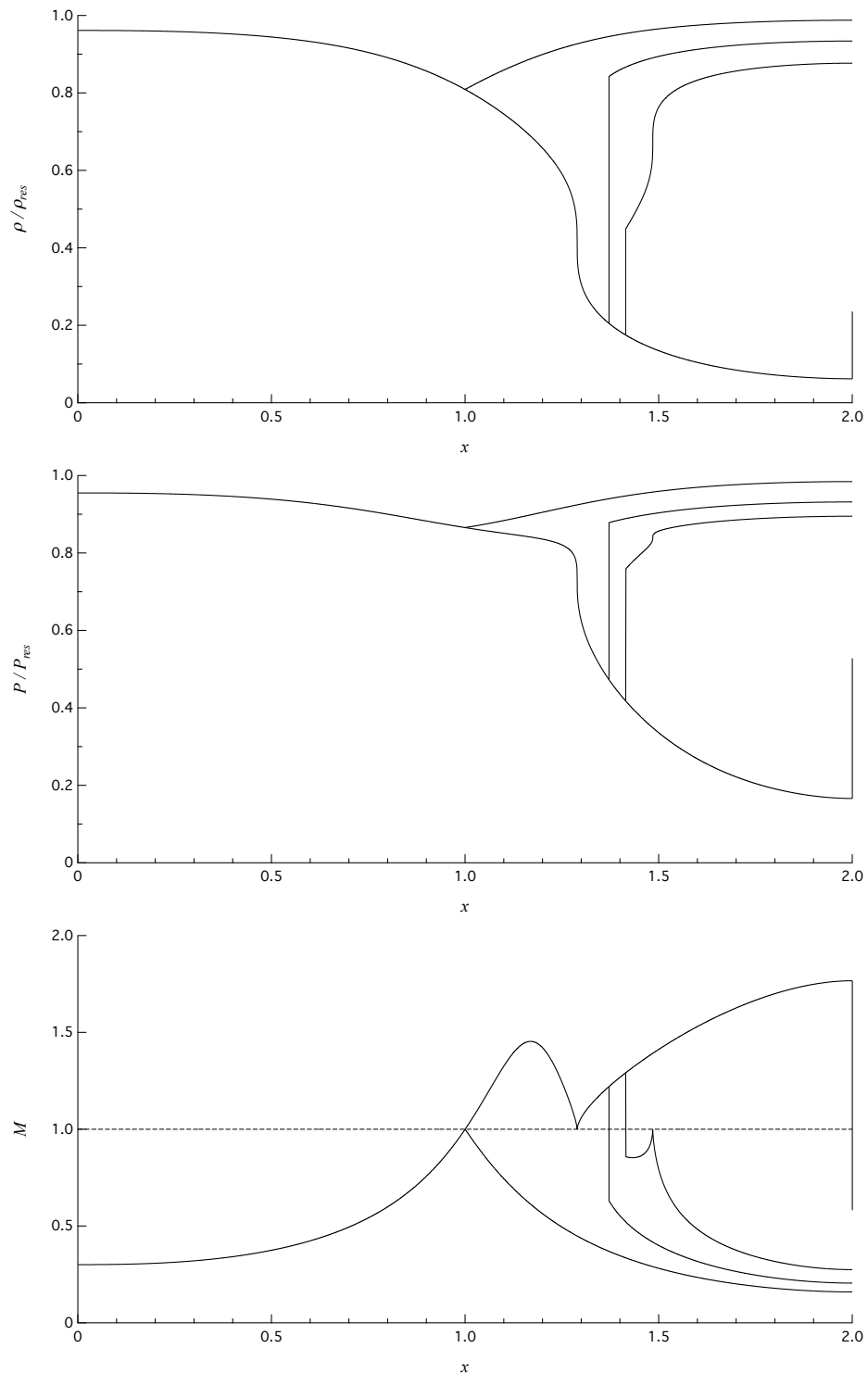


Figure 5.12: Limiting solutions for representative transitional regime  $\mathcal{R}_{\mathcal{N}^{1+}}/\mathcal{R}_{\mathcal{N}^3}$ , computed from the polytropic van der Waals model with  $\delta = 1/50$ .

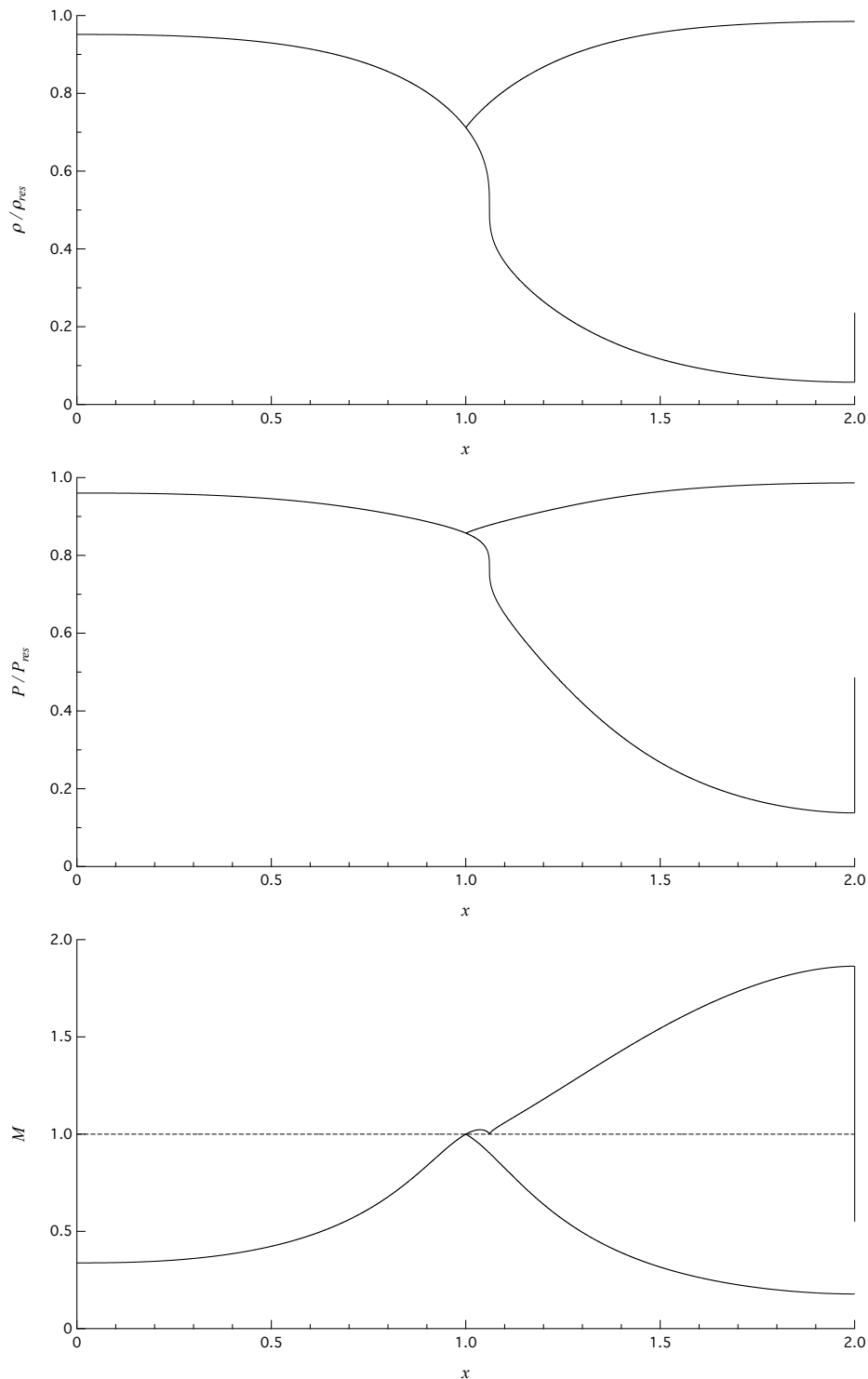


Figure 5.13: Limiting solutions for representative transitional regime  $\mathcal{R}_{N^1-}/\mathcal{R}_{M^+}$ , computed from the polytropic van der Waals model with  $\delta = 1/50$ .

## 5.2 The maximum mass flow rate

Considering a simple convergent-divergent nozzle, the critical mass flow rate function has been defined in Eq. (2.12). From nozzle theory of polytropic ideal gases one could identify the maximum mass flow rate as simply  $\dot{m}_{\max} = \dot{m}_c(s_{\text{res}}, h^t)$ . Regardless of the thermodynamic model, this is what happens if the flux function related to reservoir conditions exhibits one sonic point only, as we have seen in the description of functioning regimes having this feature. Previous discussion has shown that this is not always the case. More complex situations appear if the isentropic pattern of reservoir conditions exhibits three sonic points. Three different scenarios have been identified:

- The reservoir conditions exhibit  $\mathcal{S}_{N^+}$  isentropic pattern. The stationary point corresponding to the global maximum of the flux function is the one for the largest density,  $\rho_{s_1}$ . In this case the maximum mass flow rate equals the critical value relative to reservoir entropy, similarly to the ideal gas case.
- The reservoir conditions exhibit  $\mathcal{S}_{N^-}$  isentropic pattern. Following the contour line for the critical mass flow rate, Fig. 2.9, density assumes the sonic value  $\rho_{s_2}$  upstream of the throat. A shock with upstream state  $s = s_{\text{res}}$ ,  $\rho = \rho_{s_2}$ ,  $M = 1$  is required to continue the flow. This is precisely the behavior shown by  $\mathcal{R}_{N^{2+}}$  and  $\mathcal{R}_{N^{2-}}$  functioning regimes. We recall from discussion relative to  $\mathcal{R}_{N^{2+}}$  that

$$\dot{m}_{\max} = \dot{m}_c(s_t, h^t),$$

Admissibility requires entropy not to decrease, so that the throat entropy  $s_t$  exceed the reservoir value, causing  $\dot{m}_c(s_t, h^t) < \dot{m}_c(s_{\text{res}}, h^t)$ .

- The reservoir conditions exhibit  $\mathcal{S}_{N^-}$  isentropic pattern. However, unlike the previous case, a pre-sonic shock is not admissible from state  $(s_{\text{res}}, \rho_{s_2})$ . Considering the related phase plane, this implies that any isentropic branches for mass flow rates greater than  $f(\rho_{s_1}, s_{\text{res}}, h^t)A_t$  cannot be continued downstream of point  $\rho_{s_2}$ . This lead to limiting solutions layout of  $\mathcal{R}_{N^1}$  type. This situation had already been mentioned, for stagnation states located between the  $\mathcal{S}_{N^+}/\mathcal{S}_{N^-}$  and the  $\mathcal{R}_{N^2}/\mathcal{R}_{N^1}$  lines in Fig. 5.1. Then the only admissible density value at throat is  $\rho_{s_1}$ , resulting in

$$\dot{m}_{\max} = f(\rho_{s_1}, s_{\text{res}}, h^t)A_t,$$

which does not correspond to a critical value.

### 5.3 Map's variation with molecular complexity

The results presented so far have been computed through the polytropic van der Waals model with a relatively large value of the dimensionless specific heat,  $c_v/R = 50$ . The unrealistically large extension of the non-classical region makes it suitable for a qualitative analysis of the nozzle flow features. The present section is devoted to study the effect of varying the molecular complexity, i.e. the  $c_v/R$  value, on the exact solutions. However, instead of presenting again the exact solutions layout for all the functioning regimes, we will focus on the modifications to the thermodynamic map of functioning regimes induced by a decrease in the dimensionless specific heat. Under the assumption of considering low subsonic inlet and possibly high supersonic outlet conditions, the functioning regimes map represents the most concise way of analyzing nozzle flows.

Recalling §5.1, the map contains a set of transitional curves, delimiting the regions of reservoir conditions leading to different regimes. Some of these curves, for instance  $\mathcal{R}_{\mathcal{I}}/\mathcal{R}_{\mathcal{M}-}$ , are related to isentropic pattern transitions. Decreasing the dimensionless specific heat causes the negative- $\Gamma$  region to shrink. Considering a given isentrope, the density interval for negative- $\Gamma$  values becomes smaller. Therefore we expect the forementioned transitional curves to get closer to each other. On the other hand, some other curves in the thermodynamic map of functioning regimes are not associated to isentropic behavior. This is the case for transitional curves  $\mathcal{R}_{\mathcal{N}^2}/\mathcal{R}_{\mathcal{N}^1}$ ,  $\mathcal{R}_{\mathcal{N}^+}/\mathcal{R}_{\mathcal{N}^-}$  and  $\mathcal{R}_{\mathcal{N}^3}/\mathcal{R}_{\mathcal{M}^+}$ . Indeed, as detailed below, alterations of one of these lines lead to important changes in the map's layout.

Figures 5.14 to 5.17 show the  $P$ - $v$  map for different values of dimensionless specific heat. The dashed line in these diagrams is the one gathering reservoir states from which a post-sonic shock, with null post-shock fundamental derivative, is observed. That is, with reference to the case previously computed in §5.1, it is the line representing the union of curves  $\mathcal{R}_{\mathcal{N}^+}/\mathcal{R}_{\mathcal{N}^-}$  and  $\mathcal{R}_{\mathcal{N}^3}/\mathcal{R}_{\mathcal{M}^+}$ . The qualitative features of the present curve are significantly affected by a variation in the molecular complexity. On the contrary, curves representing isentropic pattern transitions, as well as the curve representing reservoir states from which a double sonic shock is observed, remain qualitatively unchanged.

With  $c_v/R = 30$ , the situation is very similar to the reference case,  $c_v/R = 50$ . It is possible to observe that the intersection between the isentrope tangent to the vapor dome,  $s = s_{\text{vle}}$ , and the current line moves to higher values of specific volumes. It then becomes progressively closer to curve  $\mathcal{S}_{\mathcal{M}^-}/\mathcal{S}_{\mathcal{N}^-}$ , as the dimensionless specific heat decreases towards the limit value  $c_v/R \approx 16.67$ , the lower bound for a BZT behavior. This is responsible of major changes in the map's layout. With  $c_v/R = 25$  the forementioned line doesn't cross the  $\mathcal{S}_{\mathcal{N}^+}/\mathcal{S}_{\mathcal{M}^+}$ , causing functioning regime  $\mathcal{R}_{\mathcal{N}^3}$  to disappear. With a further decrease of the dimensionless specific heat,  $c_v/R = 20$ , also regime  $\mathcal{R}_{\mathcal{N}^{1+}}$  disappears.

We also note that the thermodynamic region of interest, related to the most peculiar nozzle flows, reduces with decreasing values of  $c_v/R$ . This is a clear consequence of the shrinking of the negative- $\Gamma$  region.

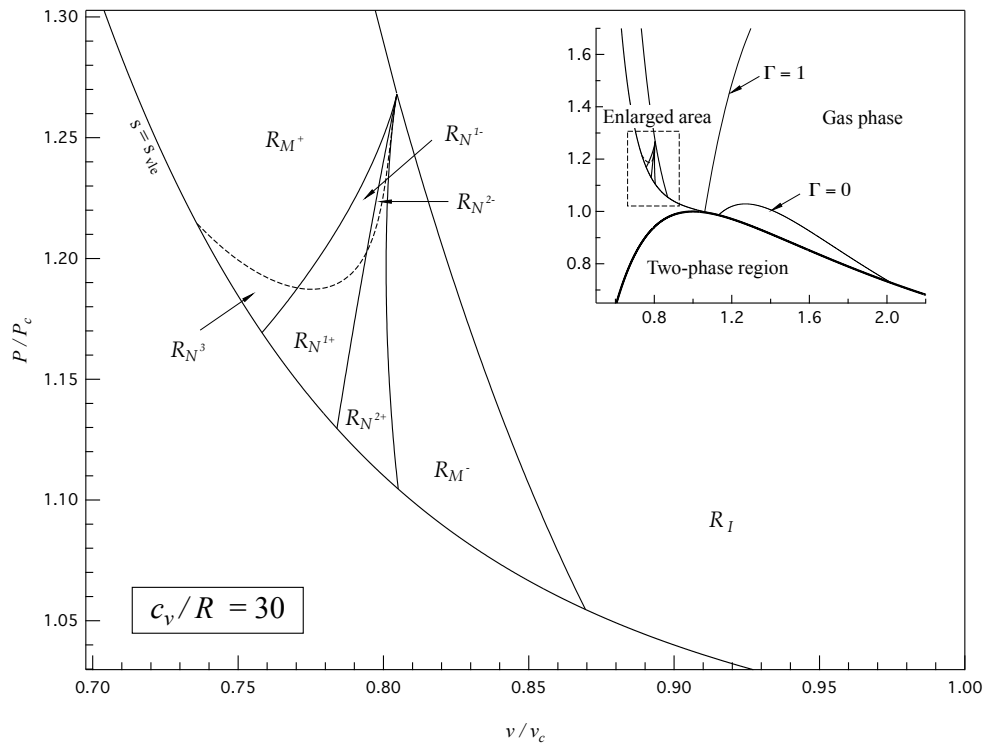


Figure 5.14:  $P$ - $v$  map of functioning regimes, computed from the polytropic van der Waals model with  $\delta = 1/30$ .

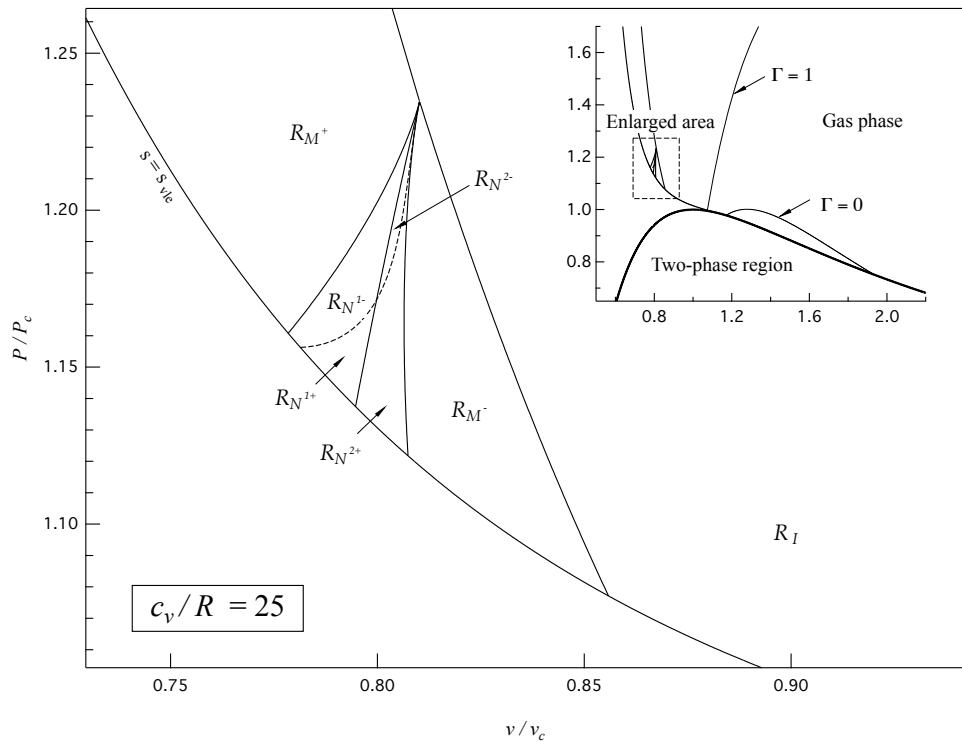


Figure 5.15:  $P$ - $v$  map of functioning regimes, computed from the polytropic van der Waals model with  $\delta = 1/25$ .

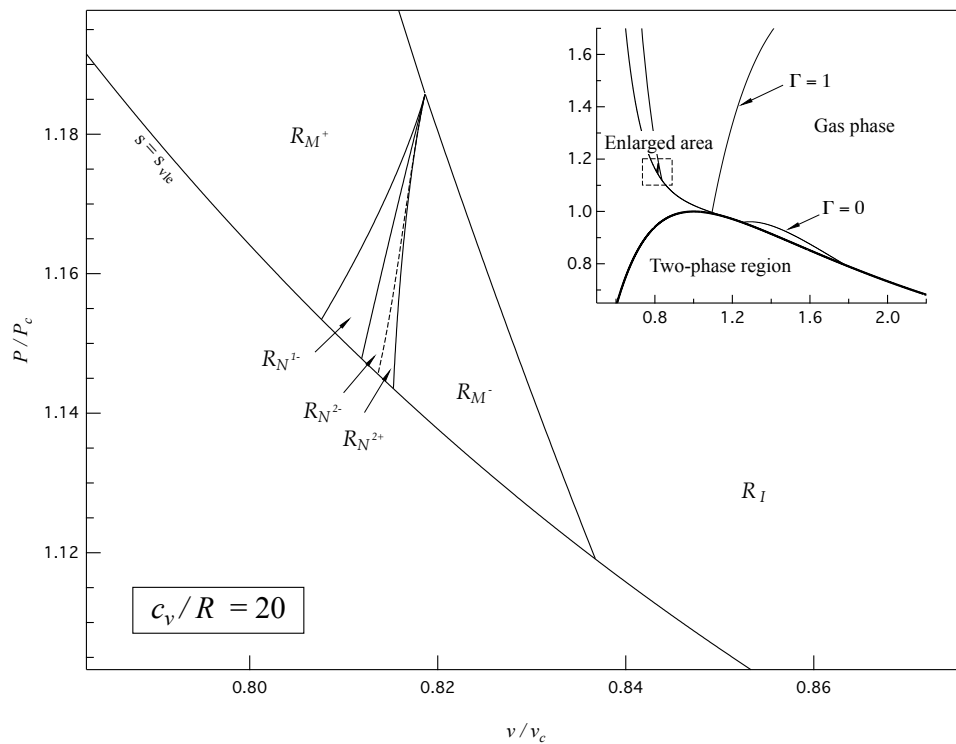


Figure 5.16:  $P$ - $v$  map of functioning regimes, computed from the polytropic van der Waals model with  $\delta = 1/20$ .

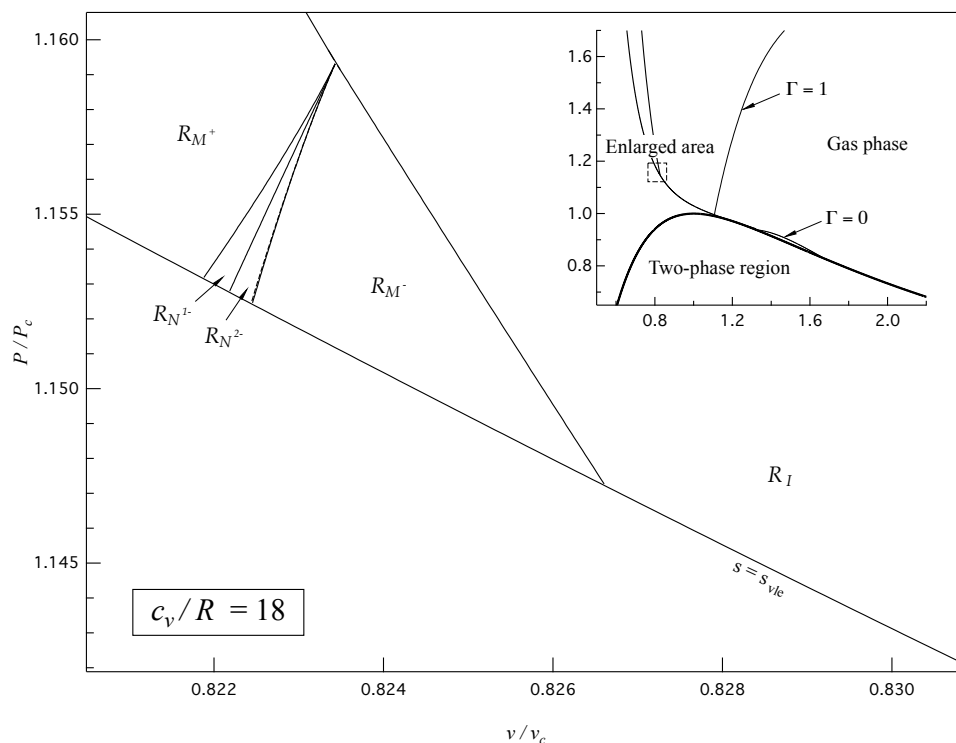


Figure 5.17:  $P$ - $v$  map of functioning regimes, computed from the polytropic van der Waals model with  $\delta = 1/18$ .



# Chapter 6

## Conclusions

Steady nozzle flows of BZT fluids, in a convergent-divergent geometry, were investigated within a quasi-1D approach. The governing differential equation were integrated obtaining uniform mass flow rate, entropy and total enthalpy along the nozzle axis. General solutions contain shock waves matching these isentropic portions by means of the Rankine-Hugoniot jump relations. For a given cross-sectional area distribution, knowledge of the entropy, the total enthalpy and the mass flow rate allowed us to use Eq. (3.2) for the computation of density along every isentropic branches, from which all the thermodynamic and kinematic variables can be obtained. The study of isentropic portions, for stagnation condition near the negative- $\Gamma$  region, is complicated by the presence three sonic points along isentropic expansions. A new tool, the isentropic pattern of a given stagnation pair, was introduced with the aim of merging information provided by standard analysis, namely inspection of the Mach-density diagram, the flux function and the phase plane.

Using the polytropic van der Waals model with large dimensionless specific heat, a set of functioning regimes was defined, considering low subsonic inlet conditions and expansion to arbitrarily large Mach numbers. This assumption allows a full examination of the non-ideal phenomena related to a particular choice of reservoir conditions, regardless of the actual nozzle area distribution. Indeed, the only geometric feature of the nozzle entering the computation process is the convergent-divergent shape.

In the computation of exact solutions, particular attention was devoted to shock-induced transitions of isentropic patterns. The entropy condition imposes a direction in which this process can possibly occur, supporting the study of limiting solutions. An example of the significance of such a transition is given by functioning regime  $\mathcal{R}_{\mathcal{N}^3}$ . Despite the reservoir conditions display isentropic pattern  $\mathcal{S}_{\mathcal{M}^+}$ , exhibiting one sonic point only, a shock-induced transition is responsible for the shock-splitting configuration in the limiting solutions layout. New functioning regimes has also been introduced on the ground of the possible transition between the shock-splitting and the simple shock configurations.

A shock capturing method was implemented, with the purpose of comparing and eventually verifying the exact solutions. The investigation has successfully confirmed the previously computed exact solutions, though some convergence

problems have been reported, especially with second order methods.

A map of functioning regimes was computed. The map defines, in a typical thermodynamic plane, the regions of stagnation conditions resulting in each functioning regimes. It is remarkable that the map's layout is independent of the actual nozzle geometry, except for the assumption of it to be convergent-divergent. The analysis reveals that the region of interest, for non-ideal nozzle flows, is located quite close to the critical point, for slightly larger pressure and density values. The extension of this region is seen to decrease as the negative- $\Gamma$  region decreases. Most important, the qualitative layout of the aforementioned region changes as the dimensionless specific heat approaches the critical value  $c_v/R \approx 16.66$ , the minimum value for a BZT behavior.

The polytropic van der Waals model was used throughout the work, it being the most simple allowing for a BZT behavior. The use of more accurate thermodynamic models is certainly one of the possible future developments.

The roles of viscosity and thermal conductivity are also to be investigated. Simulations of two-dimensional and three-dimensional steady flows represent a natural extension of this study, especially for those solutions including multiple non-classical phenomena. In this respect, the exact solutions computed in the present work may be used as starting solutions for the simulation.

# Appendices



# Appendix A

## Nozzle geometry

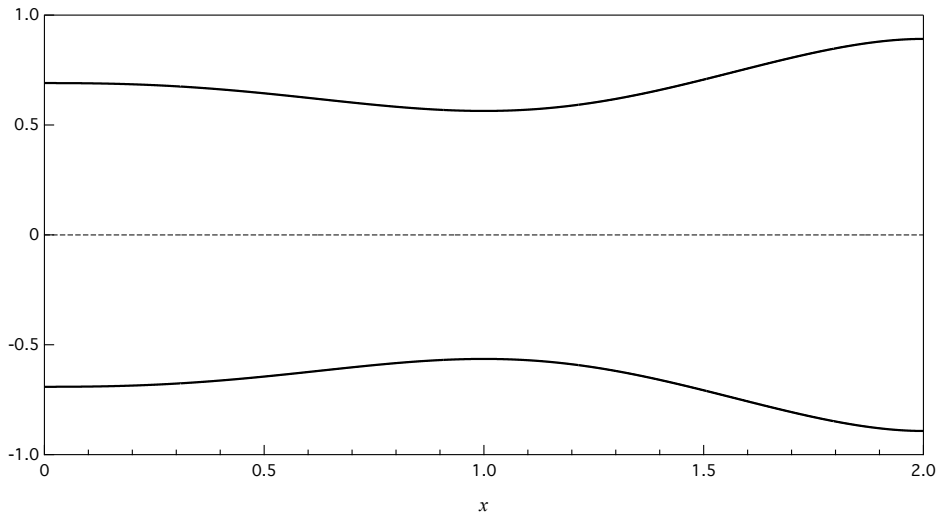


Figure A.1: Nozzle geometry.

The nozzle used throughout the present work is displayed in Fig. A.1. It is a classical converging-diverging geometry, whose cross-sectional area is described by the following polynomial equation:

$$A(x) = -0.75x^5 + 2.75x^4 - 2.25x^3 - 0.25x^2 + 1.5$$

The features of the main nozzle stations are reported in the following table.

Station	Location	Cross-sectional area
Inlet	0	1.5
Throat	1	1
Exit	2	2.5

Table A.1: Nozzle characteristics.

The six coefficients of the fifth order polynomial are computed imposing the values of Table A.1 and that the inlet, throat and exit stations are stationary points of the cross-sectional area distribution.

## Appendix B

# Shock adiabat concavity at a sonic point

A characteristic of the shock adiabat which proves to be useful in dealing with to possible solution to nozzle flows is represented by its concavity at a sonic point. For ease of notation, we will proceed with the same notation employed in §2.4.1, where variables with no subscript are used for the post-shock quantities and symbol  $[.]$  stand for the difference between post-shock and pre-shock quantities. Where necessary superscript 'RH,1' will be used to indicate evaluation along the shock adiabat from state pre-shock state. First, Eq. (2.16) is obtained. The shock adiabat  $P^{RH}(v; P_1, v_1) = P^{RH,1}(v)$  is implicitly defined by:

$$\Phi(P, v; P_1, v_1) = h(P, v) - h(P_1, v_1) - \frac{1}{2}(P - P_1)(v + v_1) = 0.$$

Hence

$$\frac{dP^{RH,1}(v)}{dv} = - \left( \frac{\partial \Phi}{\partial v} \right)_P \Bigg/ \left( \frac{\partial \Phi}{\partial P} \right)_v.$$

The two partial derivatives read:

$$\begin{aligned} \left( \frac{\partial \Phi}{\partial v} \right)_P &= \left( \frac{\partial h}{\partial v} \right)_P - \frac{1}{2}(P - P_1) = \frac{c^2}{Gv} - \frac{1}{2}[P], \\ \left( \frac{\partial \Phi}{\partial P} \right)_v &= \left( \frac{\partial h}{\partial P} \right)_v - \frac{1}{2}(v + v_1) = \frac{v}{G} + v - \frac{1}{2}(v + v_1) = \frac{v}{G} + \frac{1}{2}[v], \end{aligned}$$

given

$$\left( \frac{\partial h}{\partial v} \right)_P = \frac{c^2}{Gv} \quad \text{and} \quad \left( \frac{\partial h}{\partial P} \right)_v = v \left( 1 + \frac{1}{G} \right).$$

Therefore:

$$\frac{dP^{RH,1}(v)}{dv} = - \frac{\frac{c^2}{Gv} - \frac{1}{2}[P]}{\frac{v}{G} + \frac{1}{2}[v]} = \frac{-\frac{c^2}{v^2} + \frac{G}{2v}[P]}{1 + \frac{[v]}{2v}G}$$

and

$$\frac{dP^{RH,1}(v)}{dv} + j^2 = \frac{\frac{c^2}{v^2}(M^2 - 1)}{1 + \frac{[v]}{2v}G}, \quad (\text{B.1})$$

where  $j^2 = -[P]/[v]$  is the squared mass flux. From this follows the well-known result that, at a sonic point, the shock adiabat is tangent to the Rayleigh line. Considering (B.1), the squared mass flux variation along the shock adiabat reads

$$\frac{dj^{2RH,1}(v)}{dv} = \frac{d}{dv} \left( -\frac{P^{RH,1}(v) - P_1}{v - v_1} \right) - \frac{1}{[v]} \frac{\frac{c^2}{v^2} (M^2 - 1)}{1 + \frac{[v]}{2v} G}, \quad (\text{B.2})$$

Consider now the implicit definition of  $s^{RH}(v; P_1, v_1) = s^{RH,1}(v)$ :

$$\Psi(s, v; P_1, v_1) = h(s, v) - h(P_1, v_1) - \frac{1}{2}(P(s, v) - P_1)(v + v_1) = 0.$$

The two partial derivatives read

$$\begin{aligned} \left( \frac{\partial \Psi}{\partial v} \right)_s &= \left( \frac{\partial h}{\partial v} \right)_s - \frac{1}{2} \left( \frac{\partial P}{\partial v} \right)_s (v + v_1) - \frac{1}{2}(P - P_1) = -\frac{1}{2} \frac{c^2}{v^2} [v] - \frac{1}{2} [P], \\ \left( \frac{\partial \Psi}{\partial s} \right)_v &= \left( \frac{\partial h}{\partial s} \right)_v - \frac{1}{2} \left( \frac{\partial P}{\partial s} \right)_v (v + v_1) = T \left( 1 + \frac{[v]}{2v} G \right), \end{aligned}$$

given

$$\left( \frac{\partial h}{\partial s} \right)_v = T(1 + G) \quad \text{and} \quad \left( \frac{\partial P}{\partial s} \right)_v = \frac{TG}{v}.$$

Then the entropy variation along the shock adiabat is given by

$$\frac{ds^{RH,1}(v)}{dv} = \frac{\frac{1}{2} \frac{c^2}{v^2} [v] + \frac{1}{2} [P]}{T \left( 1 + \frac{[v]}{2v} G \right)} = \frac{\frac{[v]}{2} \frac{c^2}{v^2} (1 - M^2)}{T \left( 1 + \frac{[v]}{2v} G \right)} \quad (\text{B.3})$$

Evaluating Eqs. (B.2) and (B.3) at a sonic point provides the following result:

$$\left. \frac{dj^{2RH,1}(v)}{dv} \right|_{M=1} = 0 \quad \text{and} \quad \left. \frac{ds^{RH,1}(v)}{dv} \right|_{M=1} = 0, \quad (\text{B.4})$$

that is, the mass flux and entropy are both stationary at a sonic point. Consider now the Mach number:

$$\frac{dM^{2RH,1}(v)}{dv} = \frac{d}{dv} \left( \frac{j^2 v^2}{c^2} \right) = \frac{d}{dv} \left( -j^2 / \left( \frac{\partial P}{\partial v} \right)_s \right)$$

At a sonic point  $j^2 = \rho^2 c^2$  and its variation is null. Moreover,  $(\frac{d}{dv})_{RH} = (\frac{\partial}{\partial v})_s$ , so that the previous relation can be rewritten as

$$\left. \frac{dM^{2RH,1}(v)}{dv} \right|_{M=1} = j^2 \left( \frac{\partial^2 P}{\partial^2 v} \right)_s / \left( \frac{\partial P}{\partial v} \right)_s^2 = 2 \frac{\Gamma}{v} \quad (\text{B.5})$$

Differentiation of (B.1) yields

$$\begin{aligned} \frac{d^2 P^{RH,1}(v)}{dv^2} = & -\frac{dj^{2^{RH,1}}}{dv} \left( \frac{M^2 - 1}{M^2 \left( 1 + \frac{[v]}{2v} G \right)} - 1 \right) + \\ & + j^2 \frac{2M^3 \frac{dM^{RH,1}}{dv} \left( 1 + \frac{[v]}{2v} G \right) + (M^2 - 1) \frac{d}{dv} \left( M^2 \left( 1 + \frac{[v]}{2v} G \right) \right)}{M^4 \left( 1 + \frac{[v]}{2v} G \right)^2}, \end{aligned}$$

which, evaluated at a sonic point reads

$$\frac{d^2 P^{RH,1}(v)}{dv^2} \Big|_{M=1} = \frac{\frac{2c^2}{v^2} \frac{dM^{RH,1}}{dv} \Big|_{M=1}}{1 + \frac{[v]}{2v} G}.$$

Recalling (B.5), we finally obtain the following result for the shock adiabat concavity at a sonic point:

$$\frac{v^3}{c^2} \frac{d^2 P^{RH,1}(v)}{dv^2} \Big|_{M=1} = \frac{2\Gamma}{1 + \frac{[v]}{2v} G}. \quad (\text{B.6})$$

We recall also that, at the pre-shock state, the shock adiabat shares a second order contact with the pre-shock isentrope. Then the sign of the concavity of the shock adiabat evaluated at pre-shock state is determined by the sign of  $\Gamma$  at pre-shock state. However, this holds true also at a post-shock state, if this is sonic. Indeed, given that the denominator in the right hand side of (B.6) is positive, the sign of the shock adiabat concavity is ruled by the sign of  $\Gamma$  at post-shock state.



## Appendix C

# Solution of nonlinear systems of equations

The computation of exact solutions often involves solving nonlinear systems of equations, with particular attention on those associated to shock waves. Recalling §2.4.1, an admissible shock requires three conditions to be satisfied:

- Entropy condition: the entropy jump from pre-shock to post-shock state must be positive.
- Speed ordering condition: mechanical stability requires the pre-shock Mach number to be greater than or equal to unity and the post-shock Mach number to be lower than or equal to unity.
- The Rayleigh line from pre-shock to post-shock state must not cut the shock adiabat in interior points.

These three criteria represent constraints on the solution of the nonlinear system related to the jump relations. Simple algorithms, like Newton's method, would require some special iteration procedure to ensure that the sought root satisfies the admissibility criteria. In general, an *a posteriori* verification is also necessary.

For the present work, the solver by Bellavia, Macconi and Pieraccini [3] has been employed. It is based on a Trust Region Dogleg method, a widely used procedure for nonlinear systems of equations and optimization problems [13], conveniently modified to handle simple bounds. The reason why this solver is suitable for the present work is explained as follows. The idea, carried out throughout the computation of exact solutions, is to include the entropy and the Mach number in the independent variables of the nonlinear problem. This can be performed for example replacing pressure and velocity with the fore-mentioned variables. Moreover, thanks to the knowledge of the reservoir and boundary conditions, systems for shock waves has been processed in such a order that the pre-shock or post-shock entropy value is known, see §3.5. Hence it is straightforward to impose a bound on the pre- or post shock entropy value. Simple bounds are imposed also for the pre- and post-shock Mach numbers. Therefore solutions obtained from the method proposed in [3] automatically satisfy the entropy and speed ordering conditions.

The third admissibility criteria instead is not enforceable as a bound constraint on the independent variables. A posteriori verification is required to ensure that the shock adiabat is not cut in interior points. However, finding solutions which fulfill the entropy and the speed ordering criteria, but not the present one, is an improbable accident. Even in such a circumstance, the bound constraints on the independent variables can be reformulated to exclude the possible non-admissible root.

# Bibliography

- [1] M. Arora and P. L. Roe. On postshock oscillations due to shock capturing schemes in unsteady flows. *Journal of Computational Physics*, 130(1):25–40, 1997.
- [2] D. S. Bale, R. J. LeVeque, S. Mitran, and J. A. Rossmanith. A wave propagation method for conservation laws and balance laws with spatially varying flux functions. *SIAM Journal on Scientific Computing*, 24(3):955–978, 2003.
- [3] S. Bellavia, M. Macconi, and S. Pieraccini. Constrained dogleg methods for nonlinear systems with simple bounds. *Computational Optimization and Applications*, 53(3):771–794, 2012.
- [4] H. A. Bethe. The theory of shock waves for an arbitrary equation of state. *Technical paper 545, Office Sci. Res. & Dev*, 1942.
- [5] H. B. Callen. *Thermodynamics and an Introduction to Thermostatistics*. John Wiley and Sons, 1985.
- [6] D. Chandrasekar and P. Prasad. Transonic flow of a fluid with positive and negative nonlinearity through a nozzle. *Physics of Fluids A: Fluid Dynamics (1989-1993)*, 3(3):427–438, 1991.
- [7] P. Colonna and A. Guardone. Molecular interpretation of nonclassical gas dynamics of dense vapors under the van der waals model. *Physics of Fluids (1994-present)*, 18(5), 2006.
- [8] M. S. Cramer. Negative nonlinearity in selected fluorocarbons. *Physics of Fluids A: Fluid Dynamics (1989-1993)*, 1(11):1894–1897, 1989.
- [9] M. S. Cramer. Shock splitting in single-phase gases. *Journal of Fluid Mechanics*, 199:281–296, 1989.
- [10] M. S. Cramer and L. M. Best. Steady, isentropic flows of dense gases. *Physics of Fluids A: Fluid Dynamics (1989-1993)*, 3:219–226, 1991.
- [11] M. S. Cramer and R. N. Fry. Nozzle flows of dense gases. *Physics of Fluids A: Fluid Dynamics (1989-1993)*, 5:1246–1259, 1993.
- [12] M. S. Cramer and A. Kluwick. On the propagation of waves exhibiting both positive and negative nonlinearity. *Journal of Fluid Mechanics*, 142:9–37, 1984.

- [13] J. E. Dennis Jr and R. B. Schnabel. *Numerical methods for unconstrained optimization and nonlinear equations*, volume 16. Siam, 1996.
- [14] M. Dumbser, E. F. Toro, and Enaux C. Explicit finite volume schemes of arbitrary high order of accuracy for hyperbolic systems with stiff source terms. *J. Comput. Phys.*, pages 1049–1063, 2007.
- [15] S. H. Ferguson, T. L. Ho, B. M. Argrow, and G. Emanuel. Theory for producing a single-phase rarefaction shock wave in a shock tube. *Journal of Fluid Mechanics*, 445:37–54, 2001.
- [16] A. Guardone and L. Vigevano. Roe linearization for the van der waals gas. *Journal of Computational Physics*, 175:50–78, 2002.
- [17] A. Guardone, C. Zamfirescu, and P. Colonna. Maximum intensity of rarefaction shock waves for dense gases. *Journal of Fluid Mechanics*, 642:127–146, 2010.
- [18] A. Harten and J. M. Hyman. Self adjusting grid methods for one-dimensional hyperbolic conservation laws. *Journal of computational Physics*, 50(2):235–269, 1983.
- [19] S. Jin. A steady-state capturing method for hyperbolic systems with geometrical source terms. *ESAIM: Mathematical Modelling and Numerical Analysis*, 35(04):631–645, 2001.
- [20] S. Jin and J. G. Liu. The effects of numerical viscosities: I. slowly moving shocks. *Journal of Computational Physics*, 126(2):373–389, 1996.
- [21] S. Karni and S. Čanić. Computations of slowly moving shocks. *Journal of Computational Physics*, 136(1):132–139, 1997.
- [22] A. Kluwick. Transonic nozzle flow of dense gases. *Journal of Fluid Mechanics*, 247:661–688, 1993.
- [23] A. Kluwick. Rarefaction shocks. In *Handbook of Shock Waves, Volume 1*, chapter 3.4, pages 339–411. Academic Press, 2001.
- [24] A. Kluwick. Internal flows of dense gases. *Acta mechanica*, 169(1-4):123–143, 2004.
- [25] K. C. Lambrakis and P. A. Thompson. Existence of real fluids with a negative fundamental derivative  $\Gamma$ . *Physics of Fluids (1958-1988)*, 15(5):933–935, 1972.
- [26] L. D. Landau and E. M. Lifshitz. *Fluid Mechanics*, volume 6. Pergamon Press, 1987.
- [27] P. D. Lax. Hyperbolic systems of conservation laws II. *Comm. Pure Appl. Math.*, 10:537–566, 1957.
- [28] R. J. LeVeque. *Finite volume methods for hyperbolic problems*, volume 31. Cambridge university press, 2002.

- [29] Randall J LeVeque and Randall J Le Veque. *Numerical methods for conservation laws*, volume 132. Springer, 1992.
- [30] R. Menikoff and B. J. Plohr. The riemann problem for fluid flow of real materials. *Reviews of modern physics*, 61(1):75, 1989.
- [31] N. R. Nannan. *Advancements in nonclassical gas dynamics*. TU Delft, Delft University of Technology, 2009.
- [32] C. D. Pagani and S. Salsa. *Analisi Matematica*, volume 1. 1991.
- [33] M. Pelanti, L. Quartapelle, and L. Vigevano. Low dissipation entropy fix for positivity preserving roe's scheme. In *Godunov Methods*, pages 685–690. Springer, 2001.
- [34] G. H. Schnerr and P. Leidner. Diabatic supersonic flows of dense gases. *Physics of Fluids A: Fluid Dynamics (1989-1993)*, 3(10):2445–2458, 1991.
- [35] P. A. Thompson. A fundamental derivative in gasdynamics. *Physics of Fluids*, 14:1843–1849, 1971.
- [36] P. A. Thompson. *Compressible Fluid Dynamics*. McGraw-Hill Inc., US, 1972.
- [37] P. A. Thompson and K. C. Lambrakis. Negative shock waves. *Journal of Fluid Mechanics*, 60:187–208, 1973.
- [38] E. F. Toro. *Riemann solvers and numerical methods for fluid dynamics: a practical introduction*. Springer Science & Business Media, 2009.
- [39] N. William. Exact solution to nozzle flows of dense vapors in classical, mixed and nonclassical regimes. Master's thesis, Politecnico di Milano, 2006.
- [40] C. Zamfirescu, A. Guardone, and P. Colonna. Admissibility region for rarefaction shock waves in dense gases. *Journal of Fluid Mechanics*, 599:363–381, 2008.
- [41] Ya. B. Zeldovich. On the possibility of rarefaction shock waves. *Zh. Eksp. Teor. Fiz.*, 16(4):363–364, 1946.
- [42] Ya. B. Zel'dovich and Yu. P. Raizer. *Physics of Shock Waves and High-Temperature Hydrodynamic Phenomena*, volume 1. Academic, 1966.



# Estratto in lingua italiana

## Soluzioni esatte di flussi interni, quasi-1D e stazionari di fluidi di Bethe-Zel'dovich-Thomson

### Introduzione

L'analisi di correnti di gas ideali politropici, ossia con calore specifico a volume costante fissato, occupa un ruolo centrale nello studio delle correnti comprimibili. Tale modello termodinamico si rivela adatto per una vasta area di applicazioni, specialmente in condizioni di temperatura e pressione ordinarie. Ciononostante, avvicinandosi alla curva di vapore saturo, il modello fallisce nel prevedere il comportamento fisicamente corretto, da un punto di vista sia qualitativo che quantitativo. Una misura dell'entità degli effetti di gas reale è fornita dalla cosiddetta derivata fondamentale della gasdinamica,

$$\Gamma = \frac{v^3}{2c^2} \left( \frac{\partial^2 P}{\partial v^2} \right)_s ,$$

in cui  $P$  è la pressione,  $v$  il volume specifico,  $s$  l'entropia specifica e  $c$  la velocità del suono. La derivata fondamentale rappresenta, in maniera adimensionale, la concavità delle isoentropiche nel piano  $P-v$ . La gasdinamica classica, sia ideale che non ideale, si basa sull'assunzione che la derivata fondamentale sia positiva. Sostanze capaci di esibire, in un certo intervallo di temperature e pressioni, valori negativi di  $\Gamma$  sono note come fluidi di Bethe-Zel'dovich-Thompson e sono il principale oggetto di studio della gasdinamica nonclassica. In correnti di fluidi BZT, alcuni dei fenomeni che nel caso classico sono proibiti, come le onde d'urto d'espansione, i ventagli isoentropici di compressione, gli urti sonici e doppio-sonici sono invece non solo concessi, ma sono necessari. Tra i modelli termodinamici che consentono di descrivere il comportamento dei fluidi BZT, il più semplice è il modello di van der Waals politropico. Tale modello è utilizzato nel presente lavoro per analizzare flussi interni di fluidi BZT. Considerando trascurabili gli effetti della viscosità e della conducibilità termica, lo scopo è produrre le soluzioni esatte per un flusso monocomponente e monofase in un tipico ugello convergente-divergente, nell'ambito di un'approssimazione quasi monodimensionale. Gli effetti nonclassici associati alla presenza di una regione  $\Gamma < 0$  hanno importanti conseguenze sulla struttura della corrente, che si traducono in soluzioni esatte qualitativamente molto diverse dalle ben note soluzioni per un gas ideale politropico.

## Flussi interni di fluidi non ideali

Vengono introdotte le equazioni di governo in forma differenziale, che consistono nelle equazioni di Eulero stazionarie, nell'ambito dell'approssimazione quasi-1D. La chiusura del problema richiede di specificare la dipendenza della pressione da due variabili termodinamiche—il legame costitutivo. La scelta del modello termodinamico, il gas di van der Waals politropico, viene dettagliata e giustificata. Sulla base dei possibili valori che la derivata fondamentale della gasdinamica può assumere, si introduce una classificazione di fluidi in Low-molecular-complexity (LMC), High-molecular-complexity (HMC) e Bethe-Zel'dovich-Thompson (BZT). Per la classe di fluidi LMC la derivata fondamentale è sempre maggiore di uno. La classe HMC ammette regioni termodinamiche con  $\Gamma$  compresa tra zero e uno. La classe di fluidi BZT infine ammette regioni termodinamiche con derivata fondamentale negativa.

Le equazioni di governo vengono integrate per ottenere l'uniformità della portata massica, dell'entropia e dell'entalpia totale lungo l'asse dell'ugello. Pertanto, in una generica soluzione, le porzioni differenziabili sono isoentropiche e isototalentalpiche. Si introducono gli strumenti di base per l'analisi di flussi isoentropici: la dipendenza del numero di Mach dalla densità, la funzione di flusso, il piano delle fasi. Lo studio della funzione  $M(\rho)$  rivela che, per certe condizioni di ristagno, tre punti sonici si presentano lungo un'espansione isoentropica. La funzione di flusso o flusso di massa ricopre un ruolo importante nel determinare la soluzione in una porzione isoentropica. Le equazioni di governo vengono rielaborate ottenendo un'equazione algebrica contenente l'incognita densità, una volta fissati i valori di portata massica, entropia ed entalpia totale. L'analisi della funzione di flusso è fondamentale per individuare le condizioni sotto cui la precedente equazione definisce implicitamente l'incognita densità. Il piano delle fasi consiste in una serie di curve di livello, nel piano  $\rho$ - $x$ , della funzione portata massica, per valori di entropia ed entalpia totale fissati. L'importanza di questo strumento risiede nella possibilità di descrivere ogni flusso isoentropico, per una data geometria dell'ugello. Inoltre, specialmente per fluidi dal comportamento particolare quali i BZT, l'analisi del piano delle fasi consente di ottenere informazioni rilevanti circa la formazione di onde d'urto, a causa dell'impossibilità di continuare la corrente isoentropicamente. Attraverso gli strumenti citati, numerosi modelli di comportamento isoentropico vengono individuati. Si introduce a tal fine il concetto di schema o profilo isoentropico (isentropic pattern), come strumento capace di riassumere le proprietà delle correnti isoentropiche con determinate condizioni di ristagno. Si analizza di conseguenza l'effetto di una variazione di queste ultime e si traccia una mappa dei profili isoentropici in un tipico piano termodinamico. La mappa identifica le regioni di condizioni di ristagno che risultano in ciascuno dei modelli di corrente isoentropica individuati. Una soluzione generale al problema in esame consiste in molteplici porzioni isoentropiche raccordate tramite urti normali. Si richiamano le relazioni di salto di Rankine-Hugoniot e le condizioni di ammissibilità che consentono di selezionare la discontinuità fisicamente accettabile. Dato che l'entalpia totale rimane invariata attraverso un'onda stazionaria, la quantità stessa rimane costante lungo tutto l'ugello. La presenza di un urto nell'ugello è

in grado di determinare una variazione del profilo isoentropico. Si analizzano le possibili transizioni di questi ultimi, sapendo che l'entalpia totale è fissata e la condizione di entropia impone la direzione in cui la transizione può aver luogo.

### Soluzioni esatte per flussi interni stazionari quasi-1D

Si considera l'ugello come un dispositivo connesso a monte con un serbatoio e che scarica a valle in un ambiente a pressione costante. Le condizioni da specificare per ottenere una determinata soluzione sono rappresentate dalla coppia di variabili termodinamiche che identifica le condizioni di serbatoio e dal valore di pressione allo scarico. Questi tre parametri sostituiscono le opportune condizioni al contorno della formulazione differenziale del problema, ossia le condizioni di ingresso e uscita dell'ugello. La geometria considerata nel presente lavoro è la classica convergente-divergente.

Per condizioni di serbatoio fissate, al variare della condizione a valle, ossia la pressione allo scarico, si osserva una specifica sequenza di soluzioni. La forma e la sequenza stessa delle soluzioni identificano un determinato regime di funzionamento. Si introducono i concetti di soluzione limite e soluzione intermedia. Una soluzione è detta intermedia qualora esista un'altra soluzione qualitativamente simile alla precedente, in termini di topologia della soluzione (numero e tipo di urti, numero e tipo di porzioni isoentropiche e così via). Le soluzioni limite rappresentano il confine tra due tipi diversi di soluzione intermedia. La configurazione assunta dalle soluzioni limite è caratteristica di ciascun regime di funzionamento. Si procede a descrivere il calcolo di soluzioni limite e intermedie. Come esempio si utilizza un fluido LMC, ottenuto tramite il modello di van der Waals politropico con un basso valore di calore specifico a volume costante. Queste condizioni consentono di produrre qualitativamente le stesse soluzioni che si incontrano nei ben noti flussi in ugelli di un gas ideale politropico. Il corrispondente regime di funzionamento è indicato con  $\mathcal{R}_I$ . Il metodo qui proposto consente di ottenere la soluzione del problema risolvendo al più sistemi non lineari di equazioni algebriche, le cui radici possono essere determinate numericamente con l'accuratezza desiderata. Per tale ragione il metodo è denominato esatto. Si considera il caso dei fluidi HMC, tramite un opportuno aumento del calore specifico a volume costante, mostrando che le differenze rispetto alle correnti di fluidi LMC sono contenute e risiedono nel differente comportamento del numero di Mach nelle regioni supersoniche. Il corrispondente regime di funzionamento è indicato con  $\mathcal{R}_{M^+}$ , in aggiunta al regime  $\mathcal{R}_I$ , possibile anch'esso per fluidi HMC.

Si discutono le principali complicazioni cui si deve far fronte nel trattare fluidi BZT, in particolare la presenza di tre punti sonici lungo un'espansione isoentropica. Oltre ai regimi possibili per un fluido HMC,  $\mathcal{R}_I$  e  $\mathcal{R}_{M^+}$ , sei nuovi regimi di funzionamento sono individuati:  $\mathcal{R}_{M^-}$ ,  $\mathcal{R}_{N^{1+}}$ ,  $\mathcal{R}_{N^{1-}}$ ,  $\mathcal{R}_{N^{2+}}$ ,  $\mathcal{R}_{N^{2-}}$ ,  $\mathcal{R}_{N^3}$ . Particolare attenzione è prestata alle transizioni di profili isoentropici indotte dalla presenza di onde d'urto, che causano un aumento di entropia ad entalpia totale costante. A differenza dei fluidi LMC e HMC, per certe condizioni di serbatoio nelle correnti di fluidi BZT si dimostra l'impossibilità di ottenere espansioni isoentropiche a numeri di Mach arbitrariamente grandi. Nei classi di

funzionamento  $\mathcal{R}_{\mathcal{N}^1}$  e  $\mathcal{R}_{\mathcal{N}^2}$ , ossia  $\mathcal{R}_{\mathcal{N}^{1+}}$ ,  $\mathcal{R}_{\mathcal{N}^{1-}}$ ,  $\mathcal{R}_{\mathcal{N}^{2+}}$  e  $\mathcal{R}_{\mathcal{N}^{2-}}$ , è infatti necessaria la presenza di un'onda d'urto di espansione posizionata rispettivamente a valle e a monte della sezione di gola.

### Confronto con un metodo shock-capturing

Si effettua un confronto tra le soluzioni esatte calcolate in precedenza e i risultati prodotti da un metodo quasi-1D shock-capturing. Anzichè costruire appositamente un metodo per il calcolo di stati stazionari, si considerano qui metodi time-marching, ossia metodi temporali designati per raggiungere uno stato di regime stazionario. Questi infatti possono essere ottenuti con semplici modifiche a schemi instazionari preesistenti. Vengono presentati tre schemi numerici adatti allo scopo. Tramite un confronto preliminare si discutono le principali differenze, vantaggi e svantaggi degli stessi, con lo scopo di individuare il più adatto per le simulazioni nel presente contesto. I risultati con uno schema del primo ordine confermano da un lato la correttezza delle soluzioni esatte calcolate in precedenza, e anche la bontà del metodo nel trattare correnti di fluidi BZT, che comprendono fenomeni nonclassici quali urti di espansione e urti sonici. Vengono presentati anche i risultati dell'estensione al secondo ordine dello schema numerico. L'accordo con le soluzioni esatte è comprensibilmente migliore. Si riportano tuttavia problemi di convergenza, che si manifestano come oscillazioni della soluzione numerica intorno alla soluzione esatta di regime.

### Mappa termodinamica dei regimi di funzionamento

Il regime di funzionamento, definito in corrispondenza di un ingresso a numeri di Mach arbitrariamente bassi e di uno scarico a numeri di Mach arbitrariamente elevati, è indipendente dalla geometria dell'ugello, eccetto l'assunzione di forma convergente-divergente. Il regime di funzionamento è perciò determinato dalle condizioni di serbatoio. Di conseguenza è possibile individuare, in un tipico piano termodinamico quale il  $P$ - $v$ , le regioni di condizioni serbatoio che producono i regimi di funzionamento precedentemente descritti, ottenendo la cosiddetta mappa termodinamica dei regimi di funzionamento. A tale scopo si indagano le condizioni che determinano la transizione tra i differenti regimi. Per un fluido BZT la regione degli stati di serbatoio associati a regimi di funzionamento nonclassici è localizzata nei pressi del punto critico, per valori di pressione e densità di poco superiori. Si indaga inoltre l'effetto di una diminuzione della complessità molecolare, rispetto al caso di riferimento utilizzato nel calcolo delle soluzioni esatte. Si osservano delle mappe qualitativamente diverse al decrescere della complessità molecolare verso il valore limite per un comportamento di fluido BZT.

### Conclusioni

Le proprietà delle correnti di fluidi BZT in ugelli convergenti-divergenti sono state analizzate nell'ambito dell'approssimazione quasi mono-dimensionale. Per condizioni di serbatoio fissate, al variare della pressione allo scarico dell'ugello

---

si osserva una determinata sequenza di soluzioni che, nel complesso, definisce il regime di regime di funzionamento. Le soluzioni consistono in porzioni isoentropiche interfacciate da onde d'urto. Le equazioni di governo sono state opportunamente rielaborate ottenendo un'equazione algebrica implicita per l'incognita densità, noti i valori di entropia, entalpia totale e portata massica. Le discontinuità devono invece soddisfare il sistema di equazioni algebriche associate alle relazioni di salto, insieme a determinate condizioni di ammissibilità. La procedura di calcolo consiste perciò nel risolvere equazioni o sistemi di equazioni non lineari, giustificando la denominazione di soluzioni esatte, sebbene non ne venga fornita l'espressione analitica.

Il concetto di profilo isoentropico (isentropic pattern) è stato introdotto con l'intento di riassumere le principali proprietà delle correnti isoentropiche, per una data scelta di condizioni di ristagno. Le soluzioni esatte sono state calcolate tramite il modello di gas di van der Waals con tre diversi valori di calore specifico a volume costante, per descrivere il comportamento dei fluidi LMC, HMC e soprattutto BZT. La possibile transizione di un profilo isoentropico attraverso un urto riveste un ruolo importante nel calcolo delle soluzioni esatte, al punto da richiedere l'introduzione di specifici regimi di funzionamento.

Le soluzioni esatte sono state confrontate con i risultati di simulazioni effettuate attraverso un metodo shock-capturing time-marching. Si è riportato il buon accordo tra soluzioni esatte e numeriche, nonostante in alcuni casi si siano verificati problemi di convergenza, specialmente con il metodo di secondo ordine.

Si è proceduto al calcolo di una mappa termodinamica dei regimi di funzionamento. Questi, sotto l'ipotesi di considerare una completa espansione fino a numeri di Mach arbitrariamente grandi, sono indipendenti dalla distribuzione di area trasversale dell'ugello, eccetto per la richiesta che quest'ultimo sia convergente-divergente. Pertanto il regime di funzionamento è identificato dalle condizioni di serbatoio. E' stato quindi possibile definire le regioni, in un tipico piano termodinamico, in cui diversi stati di serbatoio danno luogo a ciascuno dei regimi di funzionamento identificati. Si discute infine l'effetto di una riduzione della complessità molecolare. La mappa subisce dei cambiamenti qualitativi, associati all'impossibilità di osservare certi regimi di funzionamento per valori di complessità molecolare prossimi al limite teorico per un comportamento BZT in fluidi di van der Waals.